

Oxygen mass transport parameters in ionomer films under controlled relative humidity

by

David Novitski

M.Sc., The University of Texas at Dallas, 2011

Thesis Submitted in Partial Fulfillment of the
Requirements for the Degree of
Doctor of Philosophy

In the
Department of Chemistry
Faculty of Science

© David Novitski 2017

SIMON FRASER UNIVERSITY

Spring 2017

All rights reserved.

However, in accordance with the *Copyright Act of Canada*, this work may be reproduced, without authorization, under the conditions for "Fair Dealing." Therefore, limited reproduction of this work for the purposes of private study, research, criticism, review and news reporting is likely to be in accordance with the law, particularly if cited appropriately.

Approval

Name: David Michael Novitski
Degree: Doctor of Philosophy
Title: *Oxygen mass transport parameters in ionomer films under controlled relative humidity*
Chair: Dr. Krzysztof Starosta
Associate Professor

Examining Committee:

Dr. Steven Holdcroft
Senior Supervisor
Professor

Dr. Michael Eikerling
Supervisor
Professor

Dr. Zuo-Guang Ye
Supervisor
Professor

Dr. Hua-Zhong Yu
Internal Examiner
Professor

Dr. Dan Bizzotto
External Examiner
Professor
Department of Chemistry
University of British Columbia

Date Defended/Approved: March 29, 2017

Abstract

Mass transport parameters are determined for the oxygen reduction reaction (ORR) at the electrochemical interface of a platinum microdisk electrode and five different series of polymer electrolyte membranes. The series included proton exchange polyfluorosulfonic acid (PFSA) based membranes (Nafion 117, Nafion 211), films cast from PFSA dispersions (DE2020), anion exchange quaternary ammonium based membranes (FAA-3), and films cast from hexamethyl-*p*-terphenyl polymethylbenzimidazole (HMT-PMBI) dispersions. The membranes differ in chemical structure, morphology, and water content controlled by relative humidity.

The series of materials were investigated over a range of temperatures (50-70 °C) and relative humidities (30-98% RH) using a solid state electrochemical cell. Cyclic voltammetry yielded the potentials where ORR is mass transport limited, as well as the electrochemically active surface area of the platinum microdisk electrode. Chronoamperometry was performed at mass transport limiting potentials, where fitting the current transients to analytical models (Cottrell/Shoup-Szabo) allowed for the calculation of oxygen diffusion coefficient (D_b), solubility (c_b), and permeability ($D_b \cdot c_b$) for the applied environmental conditions. A numerical model is also presented which highlights constraints in using the analytical models to determine mass transport parameters when the inherently-assumed infinite electrolyte thickness is not present.

During chronoamperometric measurements, where the potential applied results in the generation of liquid water at the membrane/electrode interface (ORR), a reversible time-dependent behaviour was observed where D_b and $D_b \cdot c_b$ increased over time to plateau values. The time-dependency responds to changes in relative humidity and is reversible, where mass transport parameters shift to a vapour equilibrated state over long periods of time. It is suggested that the electrochemically generated liquid water at the membrane/platinum interface during oxygen reduction results in a morphological change over repeated perturbations in the form of chronoamperometric analysis. The presence of interfacial liquid water causes hydrophilic channels, which are not present in substantial amounts at the interface in the vapour equilibrated-state, to reorient toward the surface. The increase in water-filled channels at the interface can explain the increase in D_b and $D_b \cdot c_b$, which are dependent on water content.

Oxygen mass transport parameters for both proton and anion exchange membranes are reported as a function of relative humidity. In order to perform electrochemical measurements at < 70% RH (at 50 °C) for perfluorosulfonic acid membranes and for all conditions for anion exchange membranes, a modified two-electrode setup was employed and compared to a three-electrode configuration. The oxygen diffusion coefficient is observed to depend on the water content. A lower relative humidity resulted in lower values of D_b ; significantly so for alkaline anion exchange samples compared to their acidic counterparts. c_b was observed to exhibit an inverse relationship, which increases with decreasing relative humidity. The decrease in D_b as the relative humidity was lowered was larger than the increase in c_b , which lead to a decrease in $D_b \cdot c_b$ as the relative humidity was lowered for all membranes.

Dedication

To my parents, Dave and Doreen Novitski for the support and guidance they have given me and the sacrifices they have made to ensure the best opportunity for their kids.

To Emily for her endless encouragement and enthusiasm toward the path I chose. There is no way this body of work could have taken place without her.

Acknowledgements

I am grateful for Dr. Steven Holdcroft giving me the opportunity to perform research in his group over the past 5 years. I value the hard work, patience, and thought that he has put toward my progress throughout the graduate program. I would like to express my thanks and gratitude to my supervisory committee members, Dr. Michael Eikerling and Dr. Zuo-Guang Ye for their direction during my time at SFU and for their supervision of this thesis, as well as to my internal and external examiners, Dr. Hogan Yu and Dr. Dan Bizzotto for their thorough review of this work. I would like to thank the following people for their support:

Dr. Mikhail Kozlov, who was my first mentor in laboratory research what seems like so many years ago.

Dr. Mihaela Stefan for introducing me to Steve's research and for encouraging me to pursue a PhD in Canada.

Dr. Ray Baughman for supporting me for years and igniting my enthusiasm for big ideas and science.

All current and past members of the Holdcroft group for their advice, discussions, and friendship during my time at SFU.

Dr. Zhong Xie at NRC Vancouver for his discussions and input especially at the beginning of my project.

Members of the CaRPE-FC network for the fantastic exposure to fuel cell research within Canada.

Mrs. Emily Novitski for her never ending support and patient but firm insistence on finishing the project.

My family for their helping me to get this far, and especially Dr. Crystal Engineer for her proof reading this thesis.

My son Rigel for sleeping well and letting dad finish his work.

Table of Contents

| | |
|------------------------|------|
| Approval..... | ii |
| Abstract..... | iii |
| Dedication | iv |
| Acknowledgements | v |
| Table of Contents..... | vi |
| List of Tables..... | viii |
| List of Figures..... | ix |

| | |
|--|----------|
| Chapter 1. Introduction | 1 |
| 1.1. Fuel cells | 1 |
| 1.2. Polymer electrolyte membrane fuel cells | 2 |
| 1.2.1. Proton exchange membrane fuel cell..... | 6 |
| 1.2.2. Anion exchange membrane fuel cell..... | 8 |
| 1.3. Membrane materials..... | 10 |
| 1.3.1. Proton exchange membranes..... | 10 |
| 1.3.2. Anion exchange membranes | 12 |
| 1.4. Properties of the catalyst layer..... | 15 |
| 1.4.1. Water in the ionomer | 19 |
| 1.4.2. Oxygen transport through ionomer | 22 |
| 1.5. Thesis outline | 28 |

| | |
|--|-----------|
| Chapter 2. Time-dependent mass transport for O₂ reduction at the Pt perfluorosulfonic acid ionomer interface | 30 |
| 2.1. Introduction..... | 30 |
| 2.1.1. Microdisk electrodes..... | 31 |
| 2.2. Experimental | 32 |
| 2.2.1. Materials..... | 32 |
| 2.2.2. Cyclic voltammetry | 33 |
| 2.2.3. Chronoamperometry..... | 34 |
| 2.2.4. Electrochemical cell..... | 37 |
| 2.2.5. Nafion 117 experiment protocol | 39 |
| 2.2.6. Nafion 211 and DE2020 experiment protocol | 40 |
| 2.3. Results and discussion | 40 |
| 2.3.1. Electrochemically active surface area:..... | 40 |
| 2.3.2. Time/measurement-dependence of mass transport parameters in Nafion 211 and DE2020 | 50 |
| 2.4. Conclusions..... | 52 |

| | |
|--|-----------|
| Chapter 3. Determination of O₂ mass transport at the Pt PFSA ionomer interface under reduced relative humidity | 53 |
| 3.1. Introduction..... | 53 |
| 3.2. Experimental | 54 |
| 3.2.1. Materials..... | 54 |

| | | |
|---|--|------------|
| 3.2.2. | The reference electrode..... | 54 |
| 3.2.3. | Solid-state electrochemical cell (2-electrode system)..... | 55 |
| 3.2.4. | Solid-state electrochemical cell (3-electrode system)..... | 56 |
| 3.2.5. | Chronoamperometric potential-step measurements versus relative humidity | 57 |
| 3.2.6. | Sampled current voltammetry | 57 |
| 3.2.7. | The Shoup-Szabo equation | 58 |
| 3.3. | Results | 59 |
| 3.3.1. | Justification for 2-electrode (vs. 3-electrode configuration) | 59 |
| 3.3.2. | Electrochemically active surface area..... | 63 |
| 3.3.3. | Oxygen reduction-limited chronoamperometry: Linear regression analysis | 66 |
| 3.3.4. | Oxygen reduction-limited chronoamperometry: Non-linear curve fitting analysis..... | 75 |
| 3.3.5. | Evaluation of analytical treatments | 79 |
| 3.4. | Conclusions..... | 80 |
| Chapter 4. Determination of O₂ mass transport at the Pt HMT-PMBI-OH⁻ interface under reduced relative humidity | | 81 |
| 4.1. | Introduction..... | 81 |
| 4.2. | Experimental | 84 |
| 4.2.1. | Water uptake and lambda measurements | 84 |
| 4.2.2. | Membrane preparation for water uptake and lambda measurements..... | 84 |
| 4.2.3. | Ion exchange capacity..... | 84 |
| 4.2.4. | Water uptake | 86 |
| 4.2.5. | Film preparation for the solid state electrochemical cell..... | 86 |
| 4.2.6. | Solid-state electrochemical cell..... | 87 |
| 4.2.7. | Chronoamperometric, potential step measurements..... | 87 |
| 4.3. | Results | 89 |
| 4.3.1. | Water uptake and lambda..... | 89 |
| 4.3.2. | Electrochemically active surface area..... | 90 |
| 4.3.3. | Potential step chronoamperometry | 96 |
| 4.3.4. | Numerical modeling..... | 105 |
| 4.4. | Conclusions..... | 109 |
| Chapter 5. Conclusions and future work | | 111 |
| 5.1. | Conclusions..... | 111 |
| 5.2. | Future work | 113 |
| References | | 116 |
| Appendix A. | Determination of charging constant..... | 128 |
| Appendix B. | Numerical model..... | 130 |
| | Parameter estimation..... | 132 |

List of Tables

| | | |
|------------|--|-----|
| Table 2.1. | Oxygen mass transport parameters for the Pt Nafion 117 interface obtained from data plotted in Figure 2.7, Figure 2.8, and Figure 2.9 | 45 |
| Table 3.1 | Oxygen diffusion coefficient, solubility, and permeability data for 2- and 3-electrode cells in Nafion 211 at 90% RH, 70°C, ambient air..... | 63 |
| Table 3.2 | Water content, oxygen diffusion coefficients, solubility, and permeability data for Nafion 211 and DE2020 at 70°C in ambient air obtained through area-corrected linear regression analysis..... | 71 |
| Table 4.1. | Oxygen mass transport parameters obtained through nonlinear curve fitting of the experimental data with the Shoup-Szabo equation | 101 |
| Table 4.2. | Comparison of numerical and analytical results for 2.1 meq/g IEC HMT-PMBI-OH ⁻ at 60°C | 107 |

List of Figures

| | | |
|--------------|--|----|
| Figure 1.1. | Total fuel cell polarization curve showing different regions of voltage losses dependent on current density..... | 3 |
| Figure 1.2. | Cathode catalyst layer related overpotential (η_0) as a function of current density (j_0). Contribution from doubled Tafel slope (dashed line) and mass transport related variable (dotted line) are shown separately. Reprinted with permission from reference 12. Copyright 2015 CRC Press. | 6 |
| Figure 1.3. | Schematic of a proton exchange membrane fuel cell. At the anode catalyst layer hydrogen gas is oxidized to protons which are shuttled through an ion selective membrane, while the electrons are transported through an external circuit. Oxygen reduction occurs at the cathode catalyst layer when oxygen gas reacts with the protons and electrons from the anode. | 7 |
| Figure 1.4. | Schematic of an alkaline anion exchange membrane fuel cell. At the anode catalyst layer hydrogen gas is oxidized to water which is shuttled through an ion selective membrane, while the electrons are transported through an external circuit. Oxygen reduction occurs at the cathode catalyst layer when oxygen gas reacts with the water and electrons from the anode. The product hydroxide is then transported to the anode. | 9 |
| Figure 1.5. | Chemical structure of Nafion, a perfluorosulfonic acid membrane where $x = m = n = 1$ and $y = 6-10$ | 10 |
| Figure 1.6. | Schematic representation of the hydrated morphology of perfluorosulfonic acid ionomer where hydrophilic channels have dimensions on the order of several nanometers. Reprinted with permission from reference 23. Copyright 2003 John Wiley & Sons, Inc. | 11 |
| Figure 1.7. | (Left) water uptake of Nafion 211 membrane at 25 °C, triangles represent sorption while squares represent desorption. (Right) proton conductivity of Nafion 211 membrane at 30 °C (diamonds), 50 °C (squares), and 80 °C (triangles). Reprinted with permission reference 25. Copyright 2010 Elsevier. | 12 |
| Figure 1.8. | Degradation pathways of quaternary ammonium-bearing anion exchange membranes by hydroxide attack. Printed with permission from reference 31. Copyright 2013 Springer Science and Bus Media B V. | 13 |
| Figure 1.9. | Chemical structure of polybenzimidazole. | 14 |
| Figure 1.10. | Synthetic pathway of mesitylene-polydimethylbenzimidazole and subsequent conversion to hydroxide anion form. Printed with permission from reference 32. Copyright 2012 American Chemical Society. | 14 |

| | | |
|--------------|---|----|
| Figure 1.11. | Chemical structure of hexamethyl-p-terphenyl polymethylbenzimidazole at 50% methylation. Degree of methylation can be controlled and corresponds to ion exchange capacity. Printed with permission from reference 33. Copyright 2014 American Chemical Society..... | 15 |
| Figure 1.12. | (A) Schematic of a cathode catalyst layer (not to scale) where pore volumes are present for gas ingress and water egress, and ionomer coats the catalyst agglomerates for proton conduction from the anode. (B) Distribution of the carbon support, catalyst (pure Pt), and ionomer in a catalyst layer obtained using scanning transmission x-ray microscopy. Top graphic reproduced with permission from reference 40. Copyright 2013 Electrochemical Society. Bottom graphic reproduced with permission from reference 41. Copyright 2013 Elsevier. | 16 |
| Figure 1.13. | Schematic of ionomer film thickness within a catalyst layer where thick films impede gas transport while thin films inhibit proton transport. Reproduced with permission from reference 42. Copyright 2010 Elsevier. | 18 |
| Figure 1.14. | Transmission electron microscope images at (a) low and (b) high magnifications of carbon supported catalyst with ionomer coverage shown as yellow dotted line, carbon surface represented by red dashed line. Reproduced from reference 46 under Creative Commons Attribution License CC BY..... | 18 |
| Figure 1.15. | Structural evolution of perfluorosulfonic acid membranes depending on water content. Structure inversion occurs for water contents > 0.5. Reprinted with permission from reference 24. Copyright 2000 Elsevier. | 19 |
| Figure 1.16. | Lambda values (mol of H ₂ O/mol of sulfonic acid group) versus film thickness for self-assembled thin films of Nafion. Reprinted with permission from reference 51. Copyright 2013 American Chemical Society. | 21 |
| Figure 1.17. | (a) structure of Nafion predicted through molecular dynamics with $\lambda = 15$ H ₂ O/SO ₃ ⁻ , only water and sulfonic groups are shown. (b) a unit cell of the simplified model for Nafion assuming a geometrically regular structure, and (c) connected network unit cells makes a continuous channel network. Reprinted with permission from reference 57. Copyright 2012 Elsevier. | 22 |
| Figure 1.18. | (Left) Schematic of cathode catalyst layer structure where platinum nanoparticles on carbon have metal-facing interfaces with both pore spaces as well as ionomer. (Right) Carbon agglomerates in the dry state, in an optimally wetted state with water in the primary pores, and fully flooded state (water in primary and secondary pores). Reprinted with permission from reference 50. Copyright 2006 Electrochemical Society..... | 25 |

| | | |
|--------------|--|----|
| Figure 1.19. | Schematic of O ₂ transport from pore space to Pt (not to scale). Oxygen can transit through a thin (~2 nm) ionomer layer, directly through a pore-volume exposed region, or through a film of liquid water in the pore. | 26 |
| Figure 1.20. | Humidity dependent (a) interfacial resistance and (b) bulk resistance to oxygen transport in thin Nafion film at 313 K (circle), 333 K (triangle), and 353 K (square). Reproduced with permission from reference ⁸⁰ . Copyright 2016 Elsevier. | 26 |
| Figure 1.21. | Oxygen permeability through humidified Nafion and Aquivion (shortened side-chain) membranes. Printed with permission from reference ⁸³ . Copyright 2013 Elsevier. | 27 |
| Figure 2.1. | Cyclic voltammogram of a Pt/C membrane electrode assembly at 80 °C and 100% RH versus reversible hydrogen electrode (RHE). Reprinted with permission from reference ¹⁰³ . Copyright 2012 Electrochemical Society. | 34 |
| Figure 2.2. | Potential step chronoamperometric measurement with decaying current response following mass-transport limiting potential step. | 35 |
| Figure 2.3. | Cottrell plot with linear diffusion limited region shown. Linear regression analysis with the Cottrell equation gives parameters in Eqns. 2.6 and 2.7. | 37 |
| Figure 2.4. | Diagram of electrochemical assembly showing electrodes in contact with membrane, which is exposed to vapour phase on both sides. Dynamic hydrogen electrode (DHE) used as reference. | 38 |
| Figure 2.5. | Potential step, chronoamperometric profile where open circuit is held for 6 hours followed by 20 back-to-back measurements highlighted in red. After this initial 20 sets post-6 hours, a hold at 30 minutes open circuit is made followed by the same 20 measurement sets highlighted in red. The 30 minute OCP test is performed 6 times, as highlighted by the blue line. This experimental procedure is repeated 3 times, as shown by the green line. | 39 |
| Figure 2.6. | Cyclic voltammograms (100 mV/s) of a 50 µm radius Pt microelectrode on Nafion 117 equilibrated at 70% RH and 50 °C in air. Platinum mesh counter electrode and dynamic hydrogen reference electrode. 20 th scan shown before experiments run (black line), and after (red line). V ₁ corresponds to the initial potential, V ₂ corresponds to the final potential where oxygen reduction is mass transport limited. | 41 |
| Figure 2.7. | Oxygen diffusion coefficients averaged over two batches, where error bars represent the standard deviation from two runs. First set of 20 measurements result from 6 hours open circuit potential, second and subsequent columns (broken by red lines) represents 30 minutes open circuit potential. | 42 |

| | | |
|--------------|--|----|
| Figure 2.8. | Oxygen solubility averaged over two batches, where error bars represent the standard deviation from two runs. First set of 20 measurements result from 6 hours open circuit potential, second and subsequent columns (broken by red lines) represents 30 minutes open circuit potential. | 43 |
| Figure 2.9. | Oxygen permeability averaged over two batches, where error bars represent the added relative uncertainties from the diffusion coefficient and solubility. First set of 20 measurements result from 6 hours open circuit potential, second and subsequent columns (broken by red lines) represents 30 minutes open circuit potential. | 44 |
| Figure 2.10. | (A) Oxygen diffusion coefficient, (B) solubility, and (C) permeability resulting from forced oxide growth (1.2 V for 5s, black symbols in D), and forced water production (0.4 V for 10s, red symbols in D) in Nafion 117 at 60 °C and 60% RH. | 45 |
| Figure 2.11. | Oxygen mass transport parameters averaged over two batches, where error bars represent the standard deviation. First set of 20 measurements result from 6 hours open circuit potential, second and third columns represent 30 minutes open circuit potential. | 47 |
| Figure 2.12. | Illustration of the Pt Nafion 117 interface (not to scale): (a) Equilibrated at 70% RH; (b) Following electrochemical-generation of liquid water that results in a morphological surface reconstruction in the vicinity of the electrode. | 49 |
| Figure 2.13. | (A) D_{bO_2} , (B) c_{bO_2} , and (C) $D_{bO_2} \cdot c_{bO_2}$ with repeated measurements for Nafion 211 membrane (open symbols) and cast DE2020 ionomer (filled symbols) from 90-30% RH at 70°C in air obtained with linear regression analysis. | 51 |
| Figure 3.1. | Electrochemical setup with ionomer sample pressed against a Nafion 117 backing layer. (A) Working electrode and pseudo-reference assembly are pressed against one another with compression springs to provide adequate contact pressure. (B) Comparative 3-electrode configuration. (C) Photograph of the electrochemical cell. | 56 |
| Figure 3.2. | (a) Potential step square waves with increasingly negative potential steps. (b) Resulting current responses versus time where current response becomes mass transport limited at potentials 4 and 5. (c) Sampled current voltammogram showing current response versus potential, first with kinetic region slope and a diffusion limited current plateau. Reprinted with permission from reference 2. Copyright 2000 John Wiley and Sons. | 58 |
| Figure 3.3. | Cyclic voltammograms for Nafion 211 at 90% RH where reference electrode dries out during measurement (Temperature 70°C). | 60 |

| | | |
|--------------|--|----|
| Figure 3.4. | Cyclic voltammetry scans (2 V/s) for Pt/Nafion 211 at 90% RH with a dynamic hydrogen reference electrode (3-electrode) and with a platinized Pt mesh pseudo-reference (2-electrode). Potentials for 3-electrode cyclic voltammogram have been shifted (-0.875 V, dashed line) to overlap with the cyclic voltammogram of the 2-electrode configuration. Temperature: 70°C. | 60 |
| Figure 3.5. | Sampled-current voltammograms for 2- and 3-electrode electrochemical cell with Nafion 211 membrane at 90% RH. Potentials have been shifted -0.875 V for 3-electrode data, overlaid current response for sample time of 100 ms after potential step. Three separate mechanisms are highlighted to indicate different processes occurring at specific potentials. Temperature: 70°C..... | 62 |
| Figure 3.6. | Cyclic voltammograms for Nafion 211 (2 V/s) under 90-30% RH at 70°C in air. | 64 |
| Figure 3.7. | Effective working electrode area calculated from H-adsorption charge minus background capacitive current. (Inset) stylized working electrode/ionomer interface shown where blue region is water-rich conductive area and grey is Pt surface exposed to hydrophobic domains (non-active). Effective radius (r_{eff} , dramatized for effect) is derived from the electrochemically active surface area and used in mass transport calculations. | 65 |
| Figure 3.8. | Cyclic voltammetry sweeps for cast DE2020 (1 V/s) from 90-30% RH at 70°C in air. Anomalous oxidation peak only present for 90% RH scan. | 66 |
| Figure 3.9. | Sampled-current voltammograms obtained for Nafion 211 at 90% RH and 70°C with varied initial potential, V_i . Although the value of +0.3 V was chosen in the presented work, this particular example had a current plateau at +0.2 V. Sampled current voltammetry comparisons such as this can be used to determine optimal initial and final potentials for chronoamperometric measurements. | 67 |
| Figure 3.10. | Sampled-current voltammograms for Nafion 211 from 90-30% RH (70°C). V_i =+0.3 V, plotted points are obtained by changing V_f for individual potential step measurements. Current sampling times are included in legend. | 68 |
| Figure 3.11. | Potential step measurements for Nafion 211 at 30% RH. Small circle at 0.189 s shows mass transport limiting current in the applicable potential range. Inset: linear cathodic sweep with representative potential step indicators, mass transport begins at overpotentials past Pt-O reduction peak current..... | 69 |
| Figure 3.12. | Cottrell plots for Nafion 211 at 90 to 30% RH and 70 °C. | 70 |
| Figure 3.13. | O ₂ mass transport parameters calculated by linear regression versus RH for Nafion 211 membrane and cast DE2020 at 70°C in air, with effective working electrode area corrected in calculations. | 71 |

| | | |
|--------------|---|----|
| Figure 3.14. | O ₂ mass transport parameters calculated by linear regression analysis versus RH for Nafion 211 membrane and cast DE2020 at 70°C in air, where ■ and ● emphasize r_{corr} , respectively. (A) D_{bO_2} , (B) c_{bO_2} , (C) $D_{bO_2}c_{bO_2}$ | 73 |
| Figure 3.15. | Oxygen solubilities versus oxygen partial pressure for radius corrected and uncorrected datasets. Increasing P_{O_2} corresponds with decreasing RH. | 74 |
| Figure 3.16. | (A) D_{bO_2} , (B) c_{bO_2} , (C) $D_{bO_2}c_{bO_2}$ comparison between linear regression obtained, area corrected Nafion 211 data taken at 70°C in air (present work), non-linear curve fitting obtained, area corrected Nafion 211 data taken at 70°C in air (present work), and Pt microcylinder study with Nafion 117 data taken at 60°C and fed with O ₂ gas (ref ¹³¹). | 75 |
| Figure 3.17. | Non-linear curve fit for current transient obtained for Nafion 211 at 90% RH and 70°C. | 76 |
| Figure 3.18. | O ₂ mass transport parameters calculated by non-linear curve fitting versus RH for Nafion 211 membrane and cast DE2020 at 70°C in air, using the effective (corrected) working electrode area. | 77 |
| Figure 3.19. | O ₂ mass transport parameters calculated by non-linear curve fitting versus RH for Nafion 211 membrane and cast DE2020 at 70°C in air, where ■ and ● emphasize r_{corr} , respectively. (A) D_{bO_2} , (B) c_{bO_2} , (C) $D_{bO_2}c_{bO_2}$ | 78 |
| Figure 3.20. | Current transients for DE2020 ionomer film at 70°C in air, where the green circle at 5 seconds is taken as the steady-state current. | 79 |
| Figure 3.21. | O ₂ mass transport parameters comparison for steady state, short times (Cottrell), and all times (Shoup-Szabo) in both Nafion 211 and DE2020 at 70°C in air. | 80 |
| Figure 4.1. | (A) Greater than 50% methylation of HMT-PMBI results in HMT-PMBI-OH ⁻ . The ion exchange capacity is controlled by the degree of methylation (50% methylation corresponds to 0 meq/g, 100% methylation corresponds to 3.14 meq/g). (B) Illustration of the oxygen depletion region (where L_D is diffusion length) in an ionomer film at a Pt microdisk electrode during ORR. The Pt mesh serves as the counter electrode, and allows for gas exchange directly above the platinum microdisk. | 83 |
| Figure 4.2. | Water uptake and water molecules per ion exchange site (λ) of 2.5 meq/g HMT-PMBI-OH ⁻ as a function of RH at 60 °C. Film thickness 81±3 μm. | 89 |

| | | |
|--------------|--|----|
| Figure 4.3. | Cyclic voltammogram for 2.5 meq/g HMT-PMBI-OH ⁻ at 90% RH and 60 °C, with scan rate of 250 mV/s. Platinum oxide reduction and oxidation is represented by lower and upper red arrows, respectively. Hydrogen adsorption and desorption is represented by the lower and upper blue arrows, respectively. Hydrogen adsorption charge density is used for effective surface area. Green arrow corresponds with hydrogen evolution..... | 90 |
| Figure 4.4. | Cyclic voltammograms for ionomer samples at 90% RH and 60 °C, with scan rate of 250 mV/s, except for 2.3 meq/g which had a scan rate of 500 mV/s (corrected for in surface area calculations). | 91 |
| Figure 4.5. | Cyclic voltammogram of 2.5 meq/g HMT-PMBI-I ⁻ at 70% RH, 70 °C in air at 250 mV/s. After first 3 scans, upper potential range was changed from +0.9 V to +1.1 V. Arrow denotes increasing scan number. | 92 |
| Figure 4.6. | Calculated effective working electrode surface area at 60°C in air. Dashed line (---) indicates the geometric surface area, 7.85×10^{-7} cm ² , while double dash-dash (- - -) line represents the maximum effective surface area of the electrode in 1M KOH, 5.05×10^{-6} cm ² | 93 |
| Figure 4.7. | Linear sweep voltammograms for 2.5 meq/g HMT-PMBI-OH ⁻ at 60°C in air, 150 mV/s scan rate. Arrows denote sweep direction..... | 94 |
| Figure 4.8. | Oxygen reduction reaction current transients for HMT-PMBI-OH ⁻ 2.5 meq/g at 60°C in air. Least squares fit solutions for the Shoup-Szabo equation are overlaid as fitted curves. | 95 |
| Figure 4.9. | Contour plot for solutions of the Shoup-Szabo equation for 2.5 meq/g HMT-PMBI-OH ⁻ at 98% RH and 60 °C in air. The colour corresponds to % error, with the solution of minimum error being the red point and points that lie within experimental error represented by green points..... | 97 |
| Figure 4.10. | Oxygen diffusion coefficients obtained for HMT-PMBI-OH ⁻ ionomer films and FAA-3 membranes by least squares fitting of the Shoup-Szabo equation versus RH, 60°C in air. The red points indicate values obtained for HMT-PMBI-OH ⁻ 2.1 meq/g from numerical modeling (see text). Error bars correspond to the range of solutions for the mass transport limited current transients fit to the Shoup-Szabo equation..... | 98 |
| Figure 4.11. | Oxygen solubility obtained for HMT-PMBI-OH ⁻ ionomer films and FAA-3 membranes by least squares fitting of the Shoup-Szabo equation versus RH, 60°C in air. The red points indicate values obtained for HMT-PMBI-OH ⁻ 2.1 meq/g from numerical modeling. Error bars correspond to the range of solutions for the mass transport limited current transients fit to the Shoup-Szabo equation. | 99 |

| | | |
|--------------|--|-----|
| Figure 4.12. | Oxygen permeability obtained for HMT-PMBI-OH ⁻ ionomer films and FAA-3 membranes by least squares fitting of the Shoup-Szabo equation versus RH, 60°C in air. Green stars represent permeability determined from steady state current, while red points indicate values obtained for HMT-PMBI-OH ⁻ 2.1 meq/g from numerical modeling. Error bars correspond to the range of solutions for the mass transport limited current transients fit to the Shoup-Szabo equation..... | 100 |
| Figure 4.13. | Oxygen diffusion coefficients obtained for HMT-PMBI-OH ⁻ ionomer films and FAA-3 membranes by least squares fitting of the Shoup-Szabo equation versus RH, 60°C in air. Colored fill corresponds to geometric radius of 5 µm used in the Shoup-Szabo equation. Patterned fill corresponds to effective surface area-derived radius used in the Shoup-Szabo equation. | 102 |
| Figure 4.14. | Oxygen solubility obtained for HMT-PMBI-OH ⁻ ionomer films and FAA-3 membranes by least squares fitting of the Shoup-Szabo equation versus RH, 60°C in air. Colored fill corresponds to geometric radius of 5 µm used in the Shoup-Szabo equation. Patterned fill corresponds to effective surface area-derived radius used in the Shoup-Szabo equation. | 103 |
| Figure 4.15. | Oxygen permeability obtained for HMT-PMBI-OH ⁻ ionomer films and FAA-3 membranes by least squares fitting of the Shoup-Szabo equation versus RH, 60°C in air. Colored fill corresponds to geometric radius of 5 µm used in the Shoup-Szabo equation. Patterned fill corresponds to effective surface area-derived radius used in the Shoup-Szabo equation. | 104 |
| Figure 4.16. | Diffusion coefficients and conductivities (proton and hydroxide) normalized to 90% RH values for Nafion 211 and 89% methylated (2.5 meq/g) HMT-PMBI versus relative humidity in air. Proton conductivity values taken from reference ²⁵ , hydroxide conductivities taken from reference ¹⁴² | 105 |
| Figure 4.17. | Contour plots for numerical fit normalized root mean square deviation (NRMSD) for 2.1 meq/g HMT-PMBI-OH ⁻ at 60°C in air. Colour corresponds to % NRMSD, where the red stars correspond to minimum % NRMSD. | 106 |
| Figure 4.18. | Dimensionless oxygen concentration (where a value of 1 represents bulk oxygen) distribution under the center of the electrode (x=0) versus dimensionless y-coordinate (film thickness normalized to gas-ionomer boundary) for 2.1 meq/g HMT-PMBI-OH ⁻ for 70%, 90%, and 98% RH at 60°C, $t \cong 5s$. Inset: zoom showing slopes present at 90% and 98% RH which indicate oxygen flux at gas-ionomer boundary..... | 109 |

List of Acronyms

| | |
|----------|---|
| AAEM | Alkaline anion exchange membrane |
| AAEMFC | Alkaline anion exchange membrane fuel cell |
| ACL | Anode catalyst layer |
| AFM | Atomic force microscopy |
| CA | Chronoamperometry |
| CCL | Cathode catalyst layer |
| CV | Cyclic voltammogram |
| DABCO | 1,4-diazabicyclo[2.2.2]octane |
| DHE | Dynamic hydrogen electrode |
| DI | De-ionized water |
| dm | Degree of methylation |
| DMA | Dynamic mechanical analyzer |
| DVS | Dynamic vapour sorption |
| ECSA | Electrochemically active surface area |
| FAA-3 | Commercial quaternary ammonium based membrane |
| HMT-PMBI | Hexamethyl- <i>p</i> -terphenyl polymethylbenzimidazole |
| HOR | Hydrogen oxidation reaction |
| IEC | Ion exchange capacity |
| MT | Mass transport |
| NHE | Normalized hydrogen electrode |
| NMR | Nuclear magnetic resonance |
| NRMSD | Normalized root mean square deviation |
| OCP | Open circuit potential |
| ORR | Oxygen reduction reaction |
| PBI | Polybenzimidazole |
| PEM | Proton exchange membrane |
| PEMFC | Proton exchange membrane fuel cell |
| PFSA | Perfluorosulfonic acid |
| Pt/C | Platinum nanoparticles on carbon support |
| RH | Relative humidity |
| SCV | Sampled current voltammetry |
| SPE | Solid polymer electrolyte |

Chapter 1. Introduction

1.1. Fuel cells

A fuel cell is an electrochemical device that is similar to a battery in that it converts chemical energy directly into electrical energy. The fuel cell deviates from battery technology because reactants are continuously fed during operation, whereas a battery has a finite reserve of fuel and oxidant. In this way, a fuel cell can hypothetically operate continuously so long as the reactant supply remains continuous and the components do not degrade. The first fuel cell was invented by Sir William Robert Grove in 1839, which produced electricity from the combination of platinum electrodes in contact with dilute sulphuric acid and gaseous hydrogen and oxygen.^{1,2} These early experiments produced limited current due to the low surface area of platinum catalyst in contact with sulphuric acid and reactant gases.³ In 1889, several advancements were made by Mond and Langer in the form of electrolyte-permeable materials as membranes and finely divided platinum black as catalyst.⁴ The individual cells were able to be placed on top of or next to one another, forming stacks. Such a design is the basis of modern proton exchange membrane (PEM) fuel cells.

The concept of a fuel cell involves an anode and cathode, which are electronically isolated by a resistance or load. This allows the energy of electrons, which are liberated in an oxidation reaction at the anode, to be harnessed at a set potential governed by the overall reaction. The electrons pass through the load on the way to the cathode for the corresponding reduction reaction, which is how usable work is harnessed. There are several types of fuel cell designs that differ in their electrolyte composition as well as reaction species such as alkaline, phosphoric acid, solid oxide, and molten carbonate.⁵ Each type of fuel cell has advantages and disadvantages, such as a necessity for CO₂ free oxidant streams for alkaline fuel cells, low power densities for phosphoric acid fuel cells, or long start up times for the latter two types.⁵ In the present day there is a massive thrust toward the realization of the next generation of automotive platforms, and PEM fuel cells stand out compared to other types due to their high energy and power density, low temperature of operation (30-100°C), and high efficiency.⁶

1.2. Polymer electrolyte membrane fuel cells

The use of solid polymers as the electrolyte (SPE) for fuel cells was first explored in the early 1960's at General Electric through Thomas Grubb and Leonard Niedrach.⁷ The polymer electrolyte is designed such that there are ionizable groups integrated in the polymeric structure, with a fixed ionic component in either the backbone or attached as a pendant group. A replaceable mobile counter-ion acts as a charge balance to the fixed ionic component and is the method of selective ion transport. A suitable polymer for use as an electrolyte membrane must have good selective ion conductivity (higher than 0.01 S/cm), no electronic conductivity, be resistant to chemical, thermal, and mechanical degradation, and ideally have a low cost.

The conversion of chemical energy to electrical energy depends on the maximum reversible work that can be performed for the reaction (Gibb's free energy):

$$\Delta G = \Delta H - T\Delta S \quad (1.1)$$

where ΔH is the reaction enthalpy of formation (in kJ/mol), T is the temperature (in K), and ΔS is the entropy (in J/mol*K). The theoretical standard potential (E^o) for a given reaction, without considering irreversible losses, follows the change in Gibb's free energy:

$$\Delta G^o = -nFE^o \quad (1.2)$$

where n is the number of electrons transferred and F is Faraday's constant (96,485 C/mol). Thus, the resulting work that is able to be performed by the system is defined by the amount of charge involved in the process multiplied by the potential. For example, the overall electrochemical reaction for a hydrogen fuel cell is:



where liquid water is the product, oxygen gas is reduced and hydrogen gas is oxidized. Eqn. 1.3 is overall a 4 electron process, meaning that each mole of product water is a two electron process. The change in Gibb's free energy for liquid water formation at 25 °C is $\Delta G^o_{\text{H}_2\text{O}} = -237$ kJ/mol (negative means an exothermic, or more favourable, reaction).⁸ Rearranging Eqn. 1.2 to solve for E^o reveals that the maximum E^o for the hydrogen fuel cell is 1.23 V. The second law of thermodynamics requires that not all of the energy is available to be converted directly to electricity; there must be some loss to the

environment as heat. The theoretical maximum efficiency of a fuel cell operating ideally is expressed by Eqn. 1.4:

$$\eta_{th} = \frac{\Delta G}{\Delta H} = 1 - \frac{T\Delta S}{\Delta H}, \quad (1.4)$$

where η_{th} is the temperature-dependent theoretical efficiency of the fuel cell. From thermodynamic tables at standard conditions, the enthalpy of formation for liquid water is $\Delta H_{H_2O} = -286 \text{ kJ/mol}$.⁸ Thus, about 49 kJ/mol is lost as heat to the environment and the theoretical maximum efficiency of such a process is 83%.

Another source of loss in cell voltage is given by the Nernst equation (Eqn. 1.5), which defines the change in electrode potential (E_{cell}) depending on the temperature and concentration of redox active species:

$$E_{cell} = E^o + \frac{RT}{nF} \ln \frac{c_O}{c_R}, \quad (1.5)$$

where R is the universal gas constant, T is the temperature (in K), n is the number of electrons transferred, F is Faraday's constant, and c_O and c_R are the concentrations of the oxidized and reduced species.

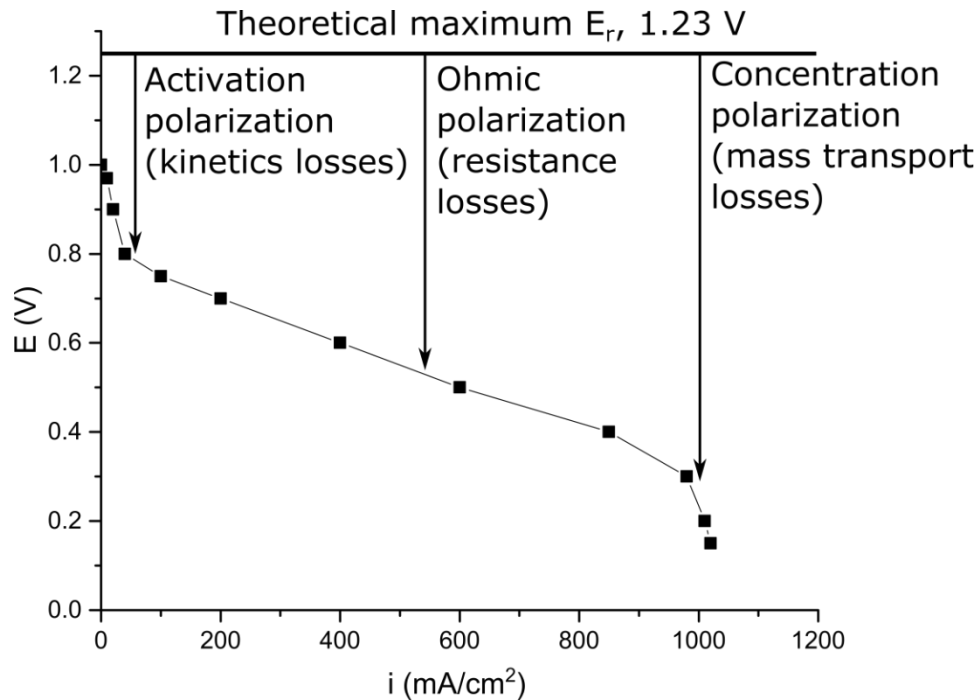


Figure 1.1. Total fuel cell polarization curve showing different regions of voltage losses dependent on current density.

When a fuel cell is in operation, the potential decreases depending on the amount of current being drawn, shown as a polarization curve in Figure 1.1. The extent of polarization is dependent upon the overpotential (η) from a series of losses, defined as:

$$\eta = E - E_{theor}, \quad (1.6)$$

The characteristics of a polarization curve are dependent on the cell geometry, electrolyte properties, and operating conditions (such as temperature, relative humidity, and gas pressures). In a hydrogen fuel cell the theoretical potential is never attained due to sluggish kinetics attributed to the oxygen reduction reaction.⁹ The activity of the catalyst, effective surface area for reaction, and chemical environment all affect the kinetics of a reaction, given by the exchange current density, j^0 , according to Eqn. 1.7²:

$$j^0 = Fk^0 c_O^{(1-\alpha)} c_R^\alpha \quad (1.7)$$

where F is Faraday's constant, k^0 is the standard heterogeneous rate constant, c_O and c_R are the concentrations of the oxidized and reduced species, and α is the electron transfer coefficient. The exchange current density represents the rate, in A/cm^2 , of the forward and backward reaction when the system is at equilibrium. In the intermediate current density region in Figure 1.1, Ohmic losses are observed and are attributed to the resistance of both ion flow in the electrolyte as well as contact resistances between components impeding the flow of electrons through the electrodes.¹⁰ In the high current density region, there are mass transport losses associated with the resistance of reactant gas transport through the porous gas diffusion and catalyst layers, causing a concentration gradient to emerge.¹¹ Eqn. 1.8 presents the combination of all losses which reveals E_{cell} , the total cell potential:

$$E_{cell} = E_{OC} - \eta_0 - R_\Omega j_0 \quad (1.8)$$

where E_{OC} corresponds to the open circuit potential of the cell, R_Ω is the Ohmic resistance of the cell comprised of the membrane and contact resistances, j_0 is the current density, and η_0 is the overpotential at the membrane/catalyst layer interface.

In a proton exchange membrane fuel cell j^0 is several orders of magnitude slower for the oxygen reduction reaction compared to the hydrogen oxidation reaction. The Tafel equation (Eqn. 1.9) shows that if the oxygen concentration in the cathode catalyst layer (c_t) decreases, then the overpotential, $|\eta_0|$, increases to maintain a given current density j_o .

$$j_o = l_{CL} j^0 \left(\frac{c_t}{c_h^0} \right) \exp \left(\frac{|\eta_o|}{b} \right) \quad (1.9)$$

where l_{CL} is the catalyst layer thickness, j^0 is the exchange current density, c_h^0 is the oxygen concentration in the cathode channel, and b is the Tafel parameter/slope defined by:

$$b = \frac{R_g T}{\alpha_{eff} F} \quad (1.10)$$

where R_g is the universal gas constant, T is the temperature, F is Faraday's constant, and α_{eff} is the electron transfer coefficient, which is between 1 and 0.5 as η increases for the 4 electron oxygen reduction reaction. The Tafel slope denotes the overpotential required to increase the current density by one order of magnitude.

At high current densities limitations from transport phenomena become severe, where either oxygen gas or proton transport is hindered and the majority of current derived from the oxygen reduction reaction comes from either the cathode catalyst layer/membrane interface (under poor proton transport) or the cathode catalyst layer/gas diffusion layer interface (under poor oxygen transport), given by Eqns. 1.11 and 1.12.

$$l_p = \frac{\sigma_p b}{j_o} = \frac{j^p}{j_o} l_{CL} \quad (1.11)$$

$$l_d = \frac{4FDc_1}{j_o} = \frac{j^d}{j_o} l_{CL} \quad (1.12)$$

where l_p and l_d are the penetration depths dependent on proton limiting or oxygen diffusion limiting conditions, respectively, σ_p is the proton conductivity, and j^p and j^d are the proton limiting or oxygen diffusion limiting current densities, respectively. In either limiting reactant condition a doubling of the Tafel slope occurs which increases the overpotential losses in the intermediate region of the polarization curve shown in Figure 1.2.

$$j_o \propto \exp \left(\frac{\eta_o}{2b} \right) \quad (1.13)$$

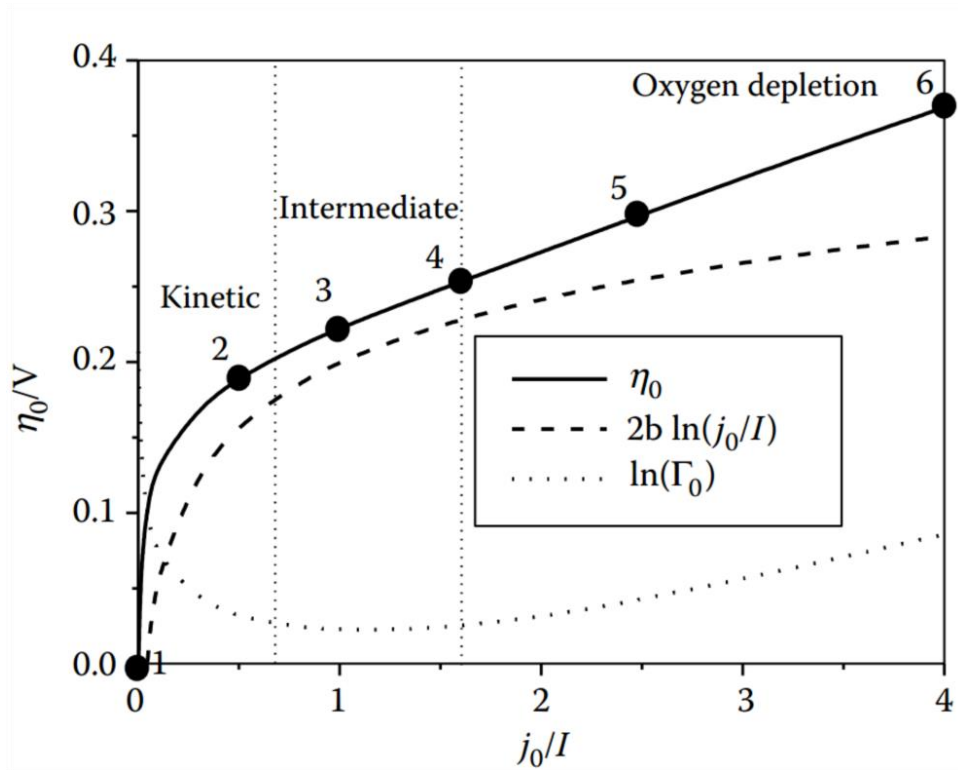


Figure 1.2. Cathode catalyst layer related overpotential (η_0) as a function of current density (j_0). Contribution from doubled Tafel slope (dashed line) and mass transport related variable (dotted line) are shown separately. Reprinted with permission from reference 12. Copyright 2015 CRC Press.

Over the past several decades, research efforts have been focusing on reducing the losses described by Eqn. 1.8.¹³ Novel catalysts are used to reduce activation overpotentials, thinner membranes are used to reduce Ohmic losses, and catalyst layer structures are optimized to reduce transport losses by improving reactant ingress and product egress.¹⁴

1.2.1. Proton exchange membrane fuel cell

A proton exchange membrane fuel cell (PEMFC) electrochemically converts hydrogen and oxygen to water and heat through the hydrogen oxidation reaction (HOR) and oxygen reduction reaction (ORR). The transport of electrons through an external circuit from the HOR in order to participate in the ORR provides an opportunity to extract meaningful electrical energy that can be used to perform work.

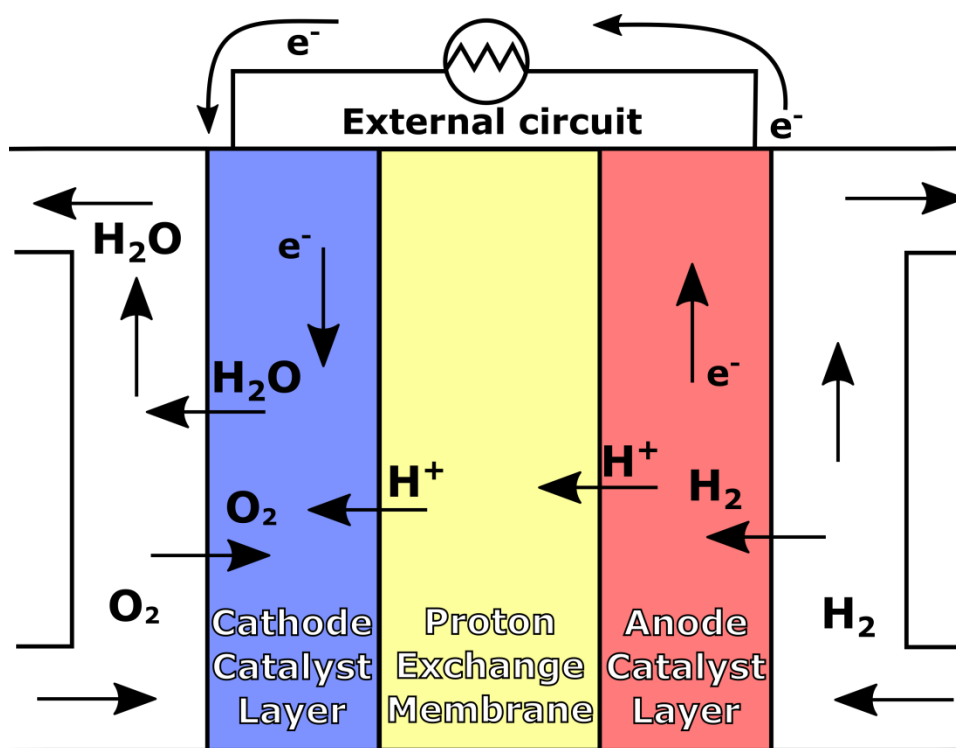


Figure 1.3. Schematic of a proton exchange membrane fuel cell. At the anode catalyst layer hydrogen gas is oxidized to protons which are shuttled through an ion selective membrane, while the electrons are transported through an external circuit. Oxygen reduction occurs at the cathode catalyst layer when oxygen gas reacts with the protons and electrons from the anode.

A simplified structure of a PEMFC is shown in Figure 1.3. Starting at the anode (right), hydrogen gas is fed through a gas diffusion layer (not shown), which helps to evenly distribute gas to the anode catalyst layer (ACL). In the ACL, hydrogen gas is oxidized into protons and electrons at accessible catalyst sites via Eqn. 1.14. The catalyst is typically supported on carbon or another electrically conductive media to facilitate transport of electrons to the cathode catalyst layer (CCL). A membrane separator ensures no electrical short between electrodes but allows facile transport of protons through a hydrophilic channel network that exists when the membrane is hydrated. The HOR occurs at a potential of 0.0 V vs. standard hydrogen electrode (SHE) and has a high exchange current density on platinum ($\sim 10^{-3}$ A/cm²).



At the CCL, oxygen is fed in the same method as on the anode side, wherein the protons that were shuttled through the PEM combine with oxygen, along with the electrons that were forced through the external circuit. This confluence of reactants must exist at an accessible platinum site so that the oxygen reduction reaction can occur. Especially at high current densities, liquid water production

presents a challenge as the water must be transported away from the reaction sites to maintain an active catalyst surface for continuous ingress of oxygen gas to participate in the oxygen reduction reaction. The oxygen reduction reaction (Eqn. 1.15) occurs at a potential of 1.23 V vs. NHE and has a low exchange current density on platinum ($\sim 10^{-10}$ A/cm²). Since the ORR exchange current density is several orders of magnitude lower than the HOR, the ORR is considered the limiting reaction, so considerable efforts have been made to understand the limitations of the ORR over the HOR.¹⁵



When combined, the overall electrochemical reaction for a proton exchange membrane fuel cell is represented by Eqn. 1.3.

1.2.2. Anion exchange membrane fuel cell

There is increasing interest in anion exchange membrane fuel cells and a resurgence in the development of materials which deliver the properties necessary for commercialization, however low hydroxide conductivities and poor stability at high temperatures and high pH are present drawbacks.^{16,17} Aside from proton exchange membrane fuel cell architectures, the transport of an anion such as OH⁻ is beneficial for several reasons. For instance, the reaction kinetics are more favourable at the cathode, leading to higher cell potentials; and the prospect of using a non-precious metal catalyst in the cathode can significantly reduce costs.^{16,18} The overall reaction of alkaline anion exchange membrane fuel cells (AAEMFCs) is the same as for PEMFCs (Eqn. 1.3), however the individual half reactions are markedly different. At the cathode ($E^o = 0.4\text{V vs. SHE}$, Eqn. 1.16), oxygen is reduced with the addition of water as a reactant, which produces hydroxide anions. The schematic in Figure 1.4 shows a simplified, non-stoichiometric view of the operation of an AAEMFC.

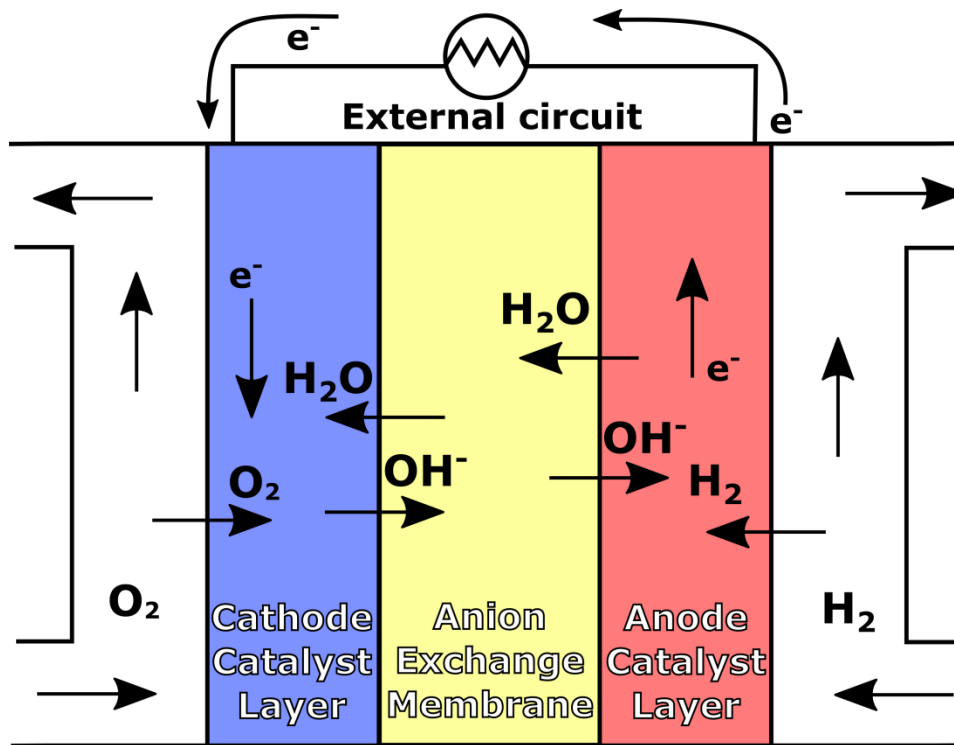


Figure 1.4. Schematic of an alkaline anion exchange membrane fuel cell. At the anode catalyst layer hydrogen gas is oxidized to water which is shuttled through an ion selective membrane, while the electrons are transported through an external circuit. Oxygen reduction occurs at the cathode catalyst layer when oxygen gas reacts with the water and electrons from the anode. The product hydroxide is then transported to the anode.



The hydroxide ions are transported to the anode, where they participate in the hydrogen oxidation reaction ($E^0 = -0.83V$ vs. *SHE*, Eqn. 1.17) to produce water. The back diffusion of product water to the cathode is critical because the hydroxide ions drag water molecules along with them from the cathode to the anode through the anion exchange membrane.



Since water is consumed at the cathode, a significant limitation for AAEMFCs is the effect of drying at the cathode side.¹⁹ Proper water management is therefore crucial both in terms of maximizing back diffusion of water to the cathode from anode, as well as humidification of inlet gas streams.

1.3. Membrane materials

1.3.1. Proton exchange membranes

In proton exchange membranes, the predominant functional group used to impart proton conductivity is sulfonic acid because of complete dissociation in the presence of water as well as high proton conductivity.²⁰ Within a polymer, the concentration of acid groups available to conduct protons is characterized by the equivalent weight, EW (grams dry polymer/mol ion exchange sites), or by the ion exchange capacity (IEC), where $IEC = 1000/EW$ for units of milliequivalents/gram.

Nafion, a perfluorosulfonic acid (PFSA) polymer, is the industry benchmark for present day proton exchange membrane fuel cells, as it exhibits most of the desired properties, except cost.²¹ Initially introduced as “XR”, Nafion was synthesized by E.I. du Pont de Nemours & Company in the late 1960’s and was a breakthrough for its time as it was able to withstand chemical degradation caused by hydrogen peroxide, which degraded then-used polystyrene based membranes.²² Nafion is a copolymer of polytetrafluoroethylene and polytrifluoroethylene with pendant perfluorosulfonic acid groups, with a chemical structure given in Figure 1.5. The high chemical and thermal stability afforded by Nafion is derived from the PTFE backbone. PFSA polymers exhibit distinct hydrophobic/hydrophilic phase separation due to the hydrophobicity of the perfluorinated backbone and flexible ether-linked side chains ending in a hydrophilic sulfonic acid exchange site. The side chains are able to form aggregated hydrophilic domains while the backbone forms crystalline hydrophobic domains. The sulfonic acid groups afford Nafion an IEC of about 0.91 meq/g.

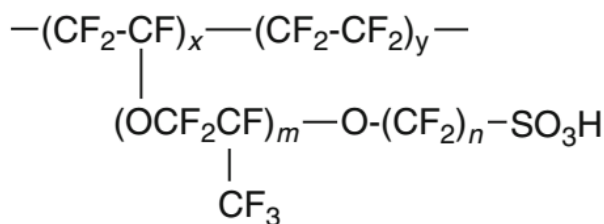


Figure 1.5. Chemical structure of Nafion, a perfluorosulfonic acid membrane where $x = m = n = 1$ and $y = 6-10$.

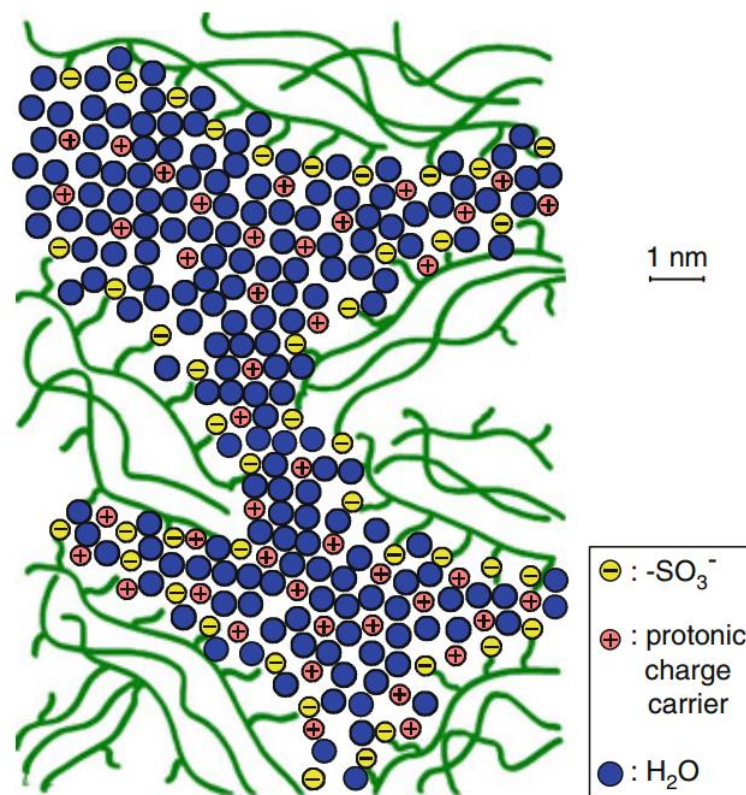


Figure 1.6. Schematic representation of the hydrated morphology of perfluorosulfonic acid ionomer where hydrophilic channels have dimensions on the order of several nanometers. Reprinted with permission from reference 23. Copyright 2003 John Wiley & Sons, Inc.

The morphology of PFSA polymers is intricately connected with the water content, influenced by gas relative humidity (RH), which influences the resulting gas transport and proton conducting behaviour. In the presence of water, a hydrated morphology is present where the hydrophilic domains swell (5-6 nm diameter, as determined by small-angle X-ray scattering), resulting in an interconnected network capable of facile proton transport, shown in Figure 1.6.²⁴ The water uptake is not linear, as shown by Figure 1.7, where a change in morphology occurs after 50% RH and water uptake becomes even higher. Peron *et al.*, for instance, has shown a drop in proton conductivity by two orders of magnitude in Nafion 211 membranes when lowering the RH from 97-10% for a range of temperatures.²⁵

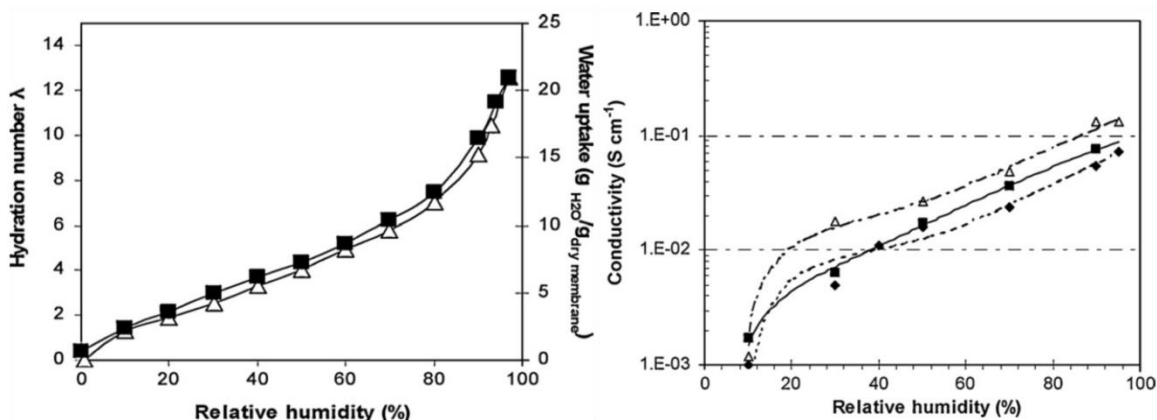


Figure 1.7. (Left) water uptake of Nafion 211 membrane at 25 °C, triangles represent sorption while squares represent desorption. (Right) proton conductivity of Nafion 211 membrane at 30 °C (diamonds), 50 °C (squares), and 80 °C (triangles). Reprinted with permission reference 25. Copyright 2010 Elsevier.

1.3.2. Anion exchange membranes

Anion exchange membranes (AEMs) are solid polymer electrolytes that contain a positively charged ionic group, such as a quaternary ammonium covalently bonded to the polymer backbone, with a negatively charged mobile anion (typically hydroxide) as the conductive species. Although AEMs have been used in wastewater treatment, desalinization, and electrodialysis for some time, the stability and conductivity of such membranes are not suitable for use in AAEMFCs.²⁶

A significant concern with AEMs is their stability over time in basic media and at elevated temperatures.¹⁸ Recent synthetic routes attempting to increase hydroxide stability include polymers bearing cationic tetraalkylammonium²⁷, phosphonium²⁸, DABCO²⁹, and imidazolium head groups.³⁰ However, the membranes tend to degrade over a relatively short period of time when subjected to high pH and temperatures. Figure 1.8 shows the chemical degradation pathways at elevated temperatures often experienced in AEMs which utilize quaternary ammonium functional groups, where hydroxide attack results in either a direct nucleophilic displacement of alcohol or tertiary amines, or if β hydrogens are present, a Hoffman elimination resulting in an alkene termination and loss of the functional group.³¹

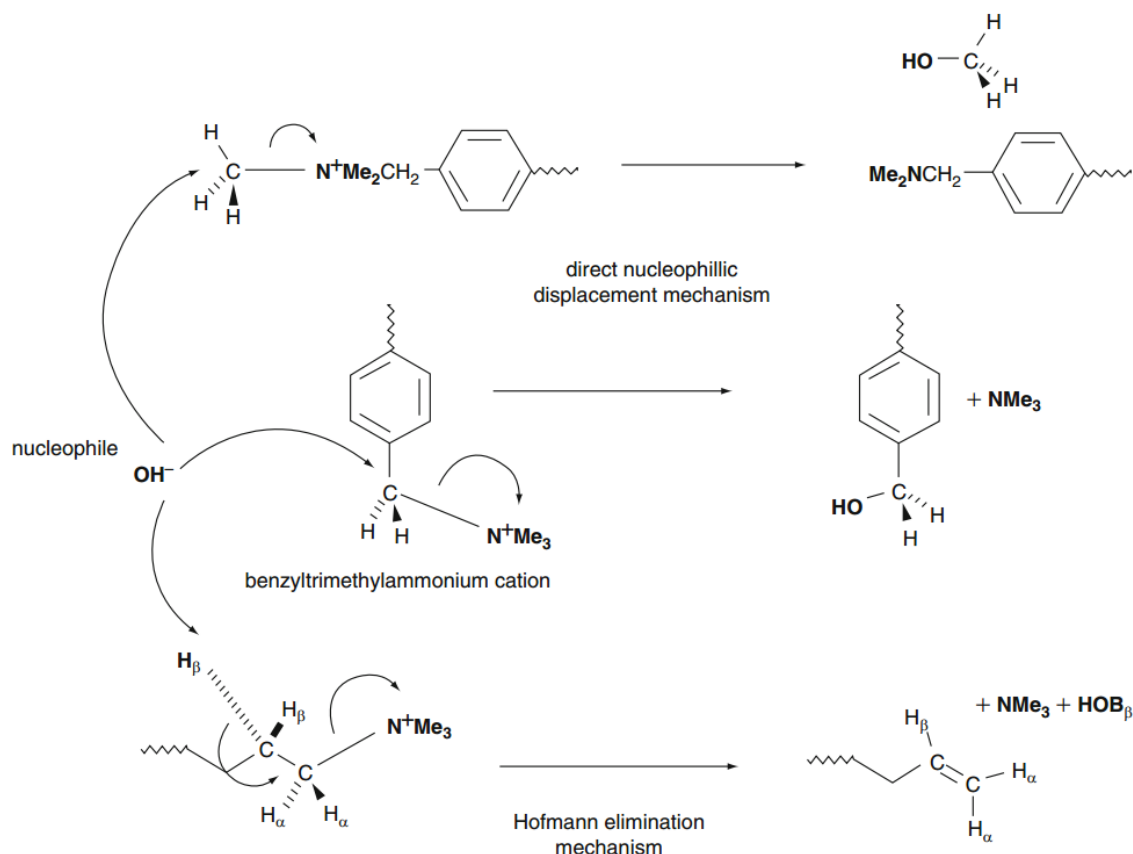


Figure 1.8. Degradation pathways of quaternary ammonium-bearing anion exchange membranes by hydroxide attack. Printed with permission from reference 31. Copyright 2013 Springer Science and Bus Media B V.

Although significant research has been made predominantly toward pendant functional groups on the polymer backbone, the poor stability at high temperatures and in alkaline conditions precludes their widespread use. A positively charged polymer backbone can eliminate the cleavage of the functional pendant group which results in a loss of conductivity. Polybenzimidazole (PBI), shown schematically in Figure 1.9, is an attractive option as an AEM due to its exceptional thermal and chemical stability. The synthetic work of Thomas *et al.*, schematically shown in Figure 1.10, resulted in the addition of a mesitylene group to PBI for added steric hindrance as protection against nucleophilic hydroxide attack.³² Subsequent dimethylation of the mesitylene-PBI resulted in a positively charged polymer which exhibited exceptional protection against hydroxide degradation, where no change was observed in NMR studies for 10 days in 2 M KOH at 60 °C.

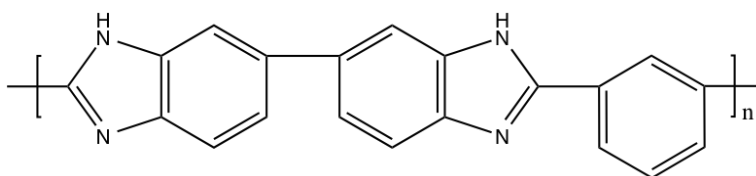


Figure 1.9. Chemical structure of polybenzimidazole.

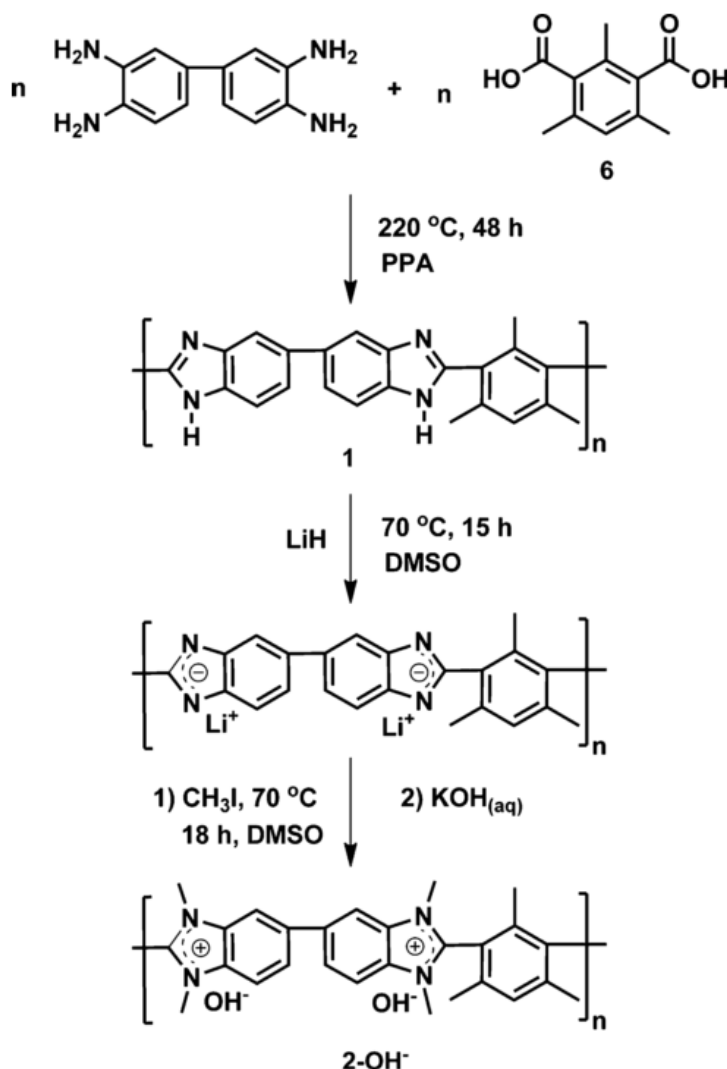
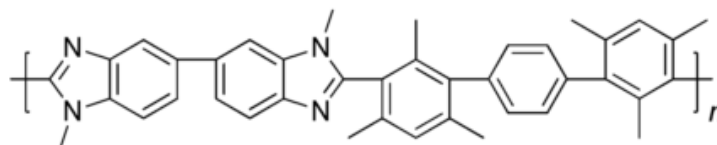


Figure 1.10. Synthetic pathway of mesitylene-polydimethylbenzimidazole and subsequent conversion to hydroxide anion form. Printed with permission from reference 32. Copyright 2012 American Chemical Society.

The mesitylene-polydimethylbenzimidazole was soluble in water, however, so an alternative approach developed by Wright replaced the mesitylene group with a hexamethyl-p-terphenylene group, shown schematically in Figure 1.11, which increased the hydrophobicity of the backbone.³³ This made

the resulting polymer insoluble in water while maintaining the steric hindrance afforded by the mesitylene group. After 7 days in 2M KOD at 60 °C, no loss of functional groups was detected by NMR, suggesting substantial stability afforded by the steric crowding. The degree of methylation can be controlled, which directly correlates to the ion exchange capacity. At high methylation (92% methylated, IEC = 2.7 meq/g), the hydroxide conductivity was reported as 9.7 mS/cm at room temperature.³³ An added benefit to the polymer, termed HMT-PMBI for hexamethyl-*p*-terphenyl polymethylbenzimidazole, is solubility in ethanol/water mixtures, which allows for its use as ionomer in catalyst layers.



50% dm HMT-PMBI

Figure 1.11. Chemical structure of hexamethyl-*p*-terphenyl polymethylbenzimidazole at 50% methylation. Degree of methylation can be controlled and corresponds to ion exchange capacity. Printed with permission from reference 33. Copyright 2014 American Chemical Society.

1.4. Properties of the catalyst layer

The catalyst layer is a complex mixture of components which are arranged in a way to maximize the ingress and egress of reactants and products, respectively, in order to maintain a constant environment favourable for reactions to occur.¹⁴ Early fuel cell catalyst layers were comprised of platinum black held together by polytetrafluoroethylene as a binder material, which had low proton conductivity and was expensive. The introduction of ionomer in the catalyst layer was introduced by Ticianelli *et al.* by brushing a solution of Nafion on the surface of the electrode, which highlighted the importance of a three-phase boundary where a continuous pathway for proton conduction is present in the catalyst layer.³⁴ Afterward, Wilson and Gottesfeld used recast Nafion as the binder, removing the polytetrafluoroethylene which subsequently allowed for lower platinum loadings.^{35,36} Eventually platinum black was replaced with platinum on supported carbon, which led to a significant reduction in the metal content. Modern catalyst layer formulation involves an ink comprised of a supported catalyst dispersed in a solvent with an ionically conductive binder material. The properties of the resulting catalyst layer are dependent on the formulation of the ink (solvent used, relative concentrations of constituents). The physical and mass transport properties of the catalyst layer are dependent on the dispersion medium, which affects the overall rate of solidification, shape and size of ionomer/carbon agglomerates, and porosity of the layer.¹⁴

For the anode and cathode catalyst layers, the carbon support is used to facilitate the flow of electrons from and to catalyst sites, respectively. Reaction sites are provided by catalyst material, most commonly platinum, which is decorated on the support material. A schematic representation of a cathode catalyst layer is shown in Figure 1.12. Platinum decorated carbon particles about 10 to 20 nm in diameter aggregate together to form agglomerates (50-100 nm).³⁷⁻³⁹ These agglomerates have pore spaces inside them about 1 to 10 nm in diameter (primary pores). Pore spaces exist between agglomerates which are about 10 to 50 nm in diameter (secondary pores). Water can penetrate in the primary pores and acts as a medium for proton transport.

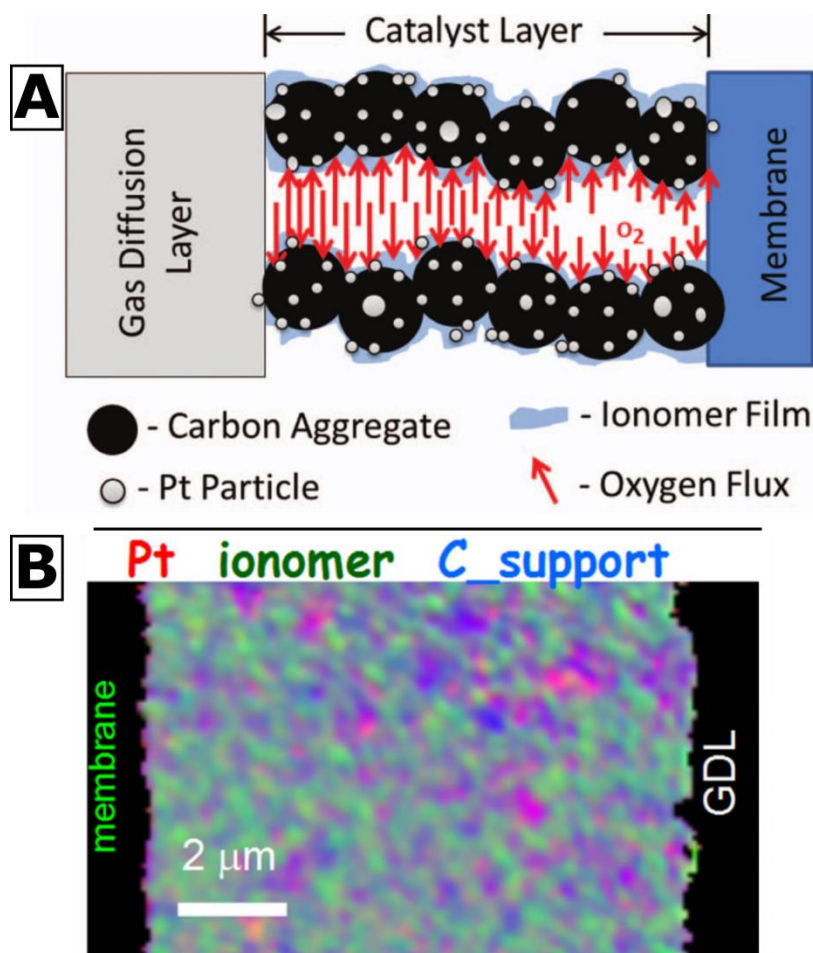


Figure 1.12. (A) Schematic of a cathode catalyst layer (not to scale) where pore volumes are present for gas ingress and water egress, and ionomer coats the catalyst agglomerates for proton conduction from the anode. (B) Distribution of the carbon support, catalyst (pure Pt), and ionomer in a catalyst layer obtained using scanning transmission x-ray microscopy. Top graphic reproduced with permission from reference 40. Copyright 2013 Electrochemical Society. Bottom graphic reproduced with permission from reference 41. Copyright 2013 Elsevier.

A mixture of ion conducting polymer known as the ionomer is added as a binder for the catalyst coated support so that ionomer coverage exists on the catalyst sites. The ionomer in the catalyst layer

cannot penetrate into the smaller primary pores, thus the ionomer network in the catalyst layer is located in the secondary pore spaces between agglomerates. Ideally, there would be a continuous network of ionomer from the anode catalyst sites to the membrane, and from the membrane to the cathode catalyst sites, to facilitate rapid ion conduction. However, too much ionomer in the catalyst layer results in flooding due to lack of available pore spaces and slow diffusion of gases to reactant sites. Too little ionomer, however, results in inaccessible platinum sites and poor proton conductivity. There is significance in the ratio between ionomer and carbon so that pore spaces are available to improve gas transport and remove product water, while still maintaining adequate proton conduction, with an ionomer to carbon ratio of around 0.8 to 1 being ideal in a Pt/C based catalyst layer.⁷ Figure 1.13 highlights the complexity of obtaining a uniform catalyst layer, where in their investigation Lee *et al.* observed that less than 15% of platinum in the catalyst layer was effectively active under optimal operating conditions (Pure O₂ and 65 °C).⁴² The role of ionomer in the catalyst layer and resulting performance losses have been modeled by Eikerling and Kulikovsky, who showed two limiting cases that result in drastic underutilization of a large part of the catalyst layer.¹² Poor proton conductivity arising from either too low ionomer content or poor ionomer network connectivity results in the oxygen reduction reaction being confined to a thin layer adjacent to the membrane. In another case, poor oxygen diffusion in the catalyst layer resulting from either liquid water flooding close to the gas diffusion layer or too much ionomer filling pore spaces leads to oxygen reduction being limited to a region close to the gas diffusion layer. In order to improve the utilization of the entire thickness of the catalyst layer, a homogeneous distribution of components is desirable.

Sadeghi *et al.* has shown that the structure of the catalyst layer significantly impacts the effective use of platinum catalyst, where smaller sized platinum/carbon agglomerates lead to higher effectiveness factors. Similarly, greater than 50% ionomer coverage on catalyst agglomerates leads to increased oxygen diffusion resistance.⁴³

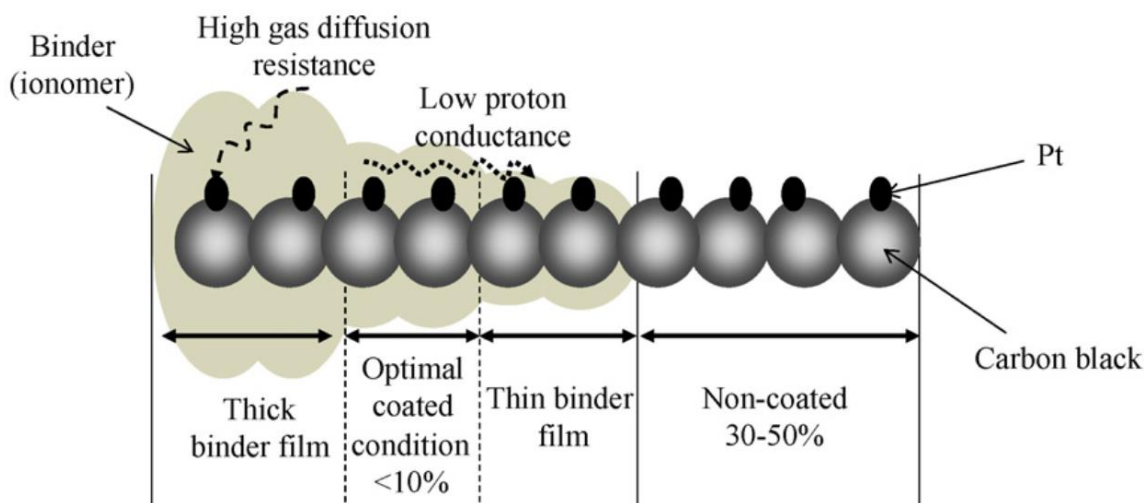


Figure 1.13. Schematic of ionomer film thickness within a catalyst layer where thick films impede gas transport while thin films inhibit proton transport. Reproduced with permission from reference 42. Copyright 2010 Elsevier.

As well, electrochemical impedance spectroscopy revealed that an ionomer to carbon (I/C) ratio of $>0.6/1$ is required in order to avoid overpotential losses from high proton resistances when operating at low relative humidities.⁴⁴ A high I/C ratio, however, leads to a reduction in electrochemically active surface area and a decrease in oxygen reduction activity at the cathode.⁴⁵ Recent work from Park et al. has shown that the carbon support morphology can also play a role in obtaining uniform ionomer coverage on catalyst sites, with thin (1-2 nm) ionomer coatings on carbon/platinum agglomerates seen in Figure 1.14.⁴⁶

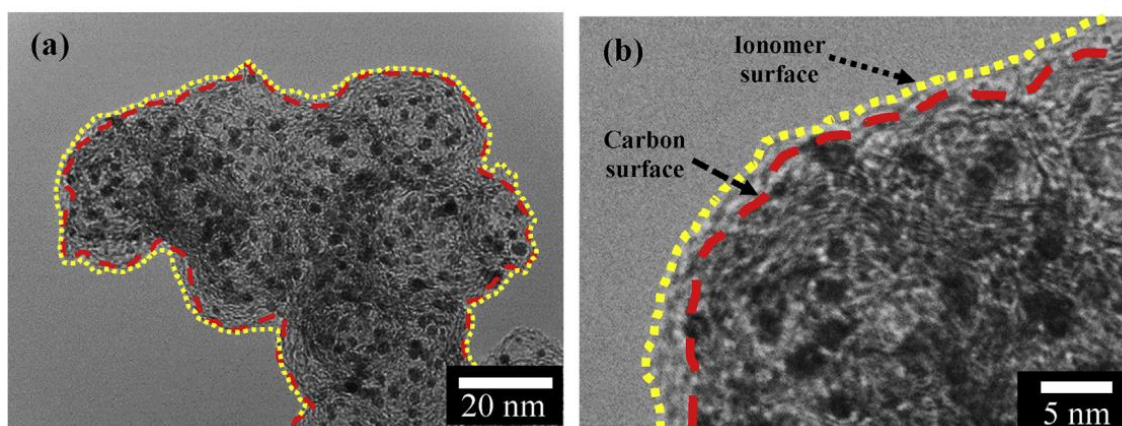


Figure 1.14. Transmission electron microscope images at (a) low and (b) high magnifications of carbon supported catalyst with ionomer coverage shown as yellow dotted line, carbon surface represented by red dashed line. Reproduced from reference 46 under Creative Commons Attribution License CC BY.

1.4.1. Water in the ionomer

Nafion membranes have been well studied for their interaction with water in both the liquid and vapour states.^{47,48} In the presence of water vapour, contact angle measurements for Nafion 117 membrane reveal similar hydrophobic surface character from dry to high relative humidity (RH) with a hydrophobic contact angle of 108.1 and 103.4 degrees, respectively. In the presence of liquid water the contact angle was observed to decrease to 22.3 degrees.⁴⁷ Complimentary atomic force microscopy measurements observed a roughening in the surface topography of the membrane when exposed to liquid water compared to water vapour. A morphological change has been proposed where the hydrophobic backbone is initially exposed to membrane interface under conditions of water vapour, where the presence of liquid water at the interface causes a reorganization of the hydrophilic sulfonic side chain sites, which significantly improves proton conductivity.

Similarly, a reduction in water content in the fuel streams in a PEMFC has resulted in a decrease in ORR kinetics, by at least a 20 mV overpotential losses at 30% RH.⁴⁹ At 30% RH, the exchange current density for ORR was observed to decrease by a factor of 2, attributed to both the lower water content as well as decreased proton conductivity in the ionomer. Where too little water causes problems with proton and reactant transport, too much causes severe flooding, which impedes fuel cell operation.^{38,50} Gebel *et al.* proposed a model using small angle neutron and X-ray scattering data where, as liquid water percolates at low (<50% RH) relative humidity, spherical ionic clusters are present, forming an interconnected network. At higher (>50% RH) relative humidities, there is a structural inversion that takes place and at higher relative humidities to pure solution state, there exists rod like particles with varying degrees of connectedness.²⁴ This structural evolution is shown schematically in Figure 1.15.

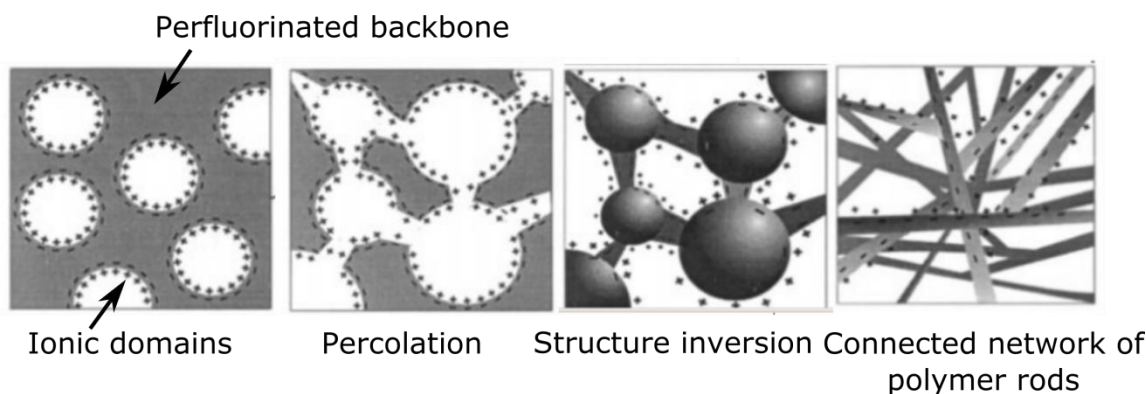


Figure 1.15. Structural evolution of perfluorosulfonic acid membranes depending on water content. Structure inversion occurs for water contents > 0.5. Reprinted with permission from reference 24. Copyright 2000 Elsevier.

Water uptake of PFSA ionomers has been reported to behave differently from expectations as ionomer in the catalyst layer is confined to thicknesses on the order of single nanometers. Modestino *et al.* have shown significant losses in proton conductivity versus film thickness, likely caused by the isolation of conductive sulfonic sites by the absorption of more than 5 times the amount of water compared to bulk membranes, as shown in Figure 1.16.⁵¹

Modestino and coworkers reported that ionomer present at thicknesses of several nanometers begin to lose their phase separated morphology that exists at the macroscale, leading to a high degree of water uptake, film swelling and decreased ionic conductivity.⁵¹ As well, thermal treatment (>110 °C) of 10 nm thin Nafion films resulted in a change in surface morphology, from very hydrophilic to hydrophobic, resulting in an 81% loss in proton conductivity.⁵² Upon exposure to liquid water, however, the surface rearranged from hydrophobic to hydrophilic and the proton conductivity was even higher than the base state.

As well, the stiffness of Nafion ionomer was observed to increase when confined to nanoscale films, where decreasing film thickness results in a higher modulus.⁵³ This stiffening effect is able to explain previously observed water transport and uptake characteristics. Studies performed on 15 nm Nafion films at elevated temperature and high RH have shown improved water uptake upon lowering the temperature, as well as a hysteresis effect at high RH, alluding to some reorganization of polymer structure when exposed to high temperature, high RH conditions.⁵⁴ Additional thin film investigations have revealed a time-dependent surface restructuring from hydrophobic to hydrophilic upon exposure to liquid water that depends on film thickness.⁵⁵

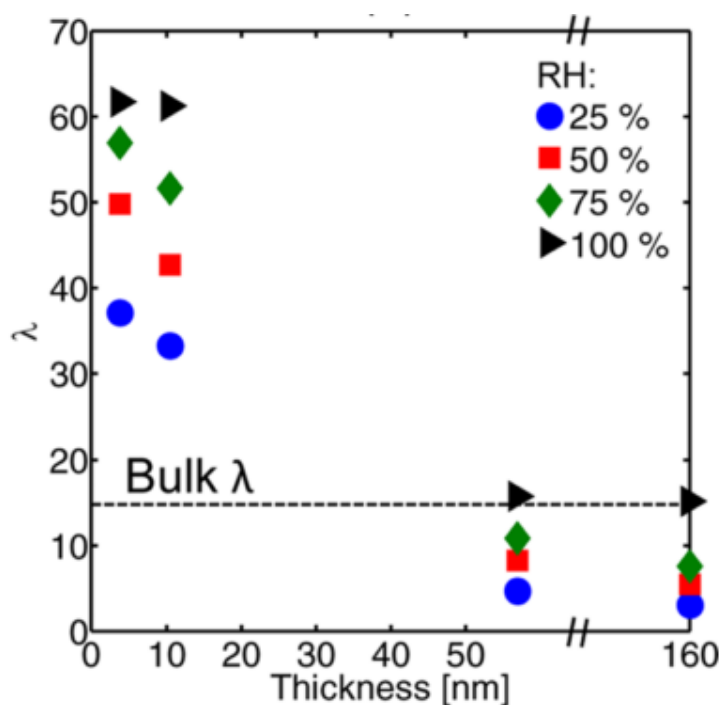


Figure 1.16. Lambda values (mol of H₂O/mol of sulfonic acid group) versus film thickness for self-assembled thin films of Nafion. Reprinted with permission from reference 51. Copyright 2013 American Chemical Society.

Adachi *et al.* reported significant interfacial resistances to water permeation in Nafion films compared to the bulk internal resistance, suggesting that the membrane/vapour interface was the limiting transport mechanism for water transport.⁵⁶ Duan *et al.* further investigated water mass transport through Nafion and proposed a network of hydrophilic channels 2.5 nm in diameter spaced 5.5 nm apart using molecular dynamics simulations.⁵⁷ In this model, shown in Figure 1.17, a unit cell contains struts, which were proposed as being the hydrophilic channels, and voids, proposed as being the hydrophobic backbone. Combining unit cells ideally in a regular pattern shows a well-defined morphological network.

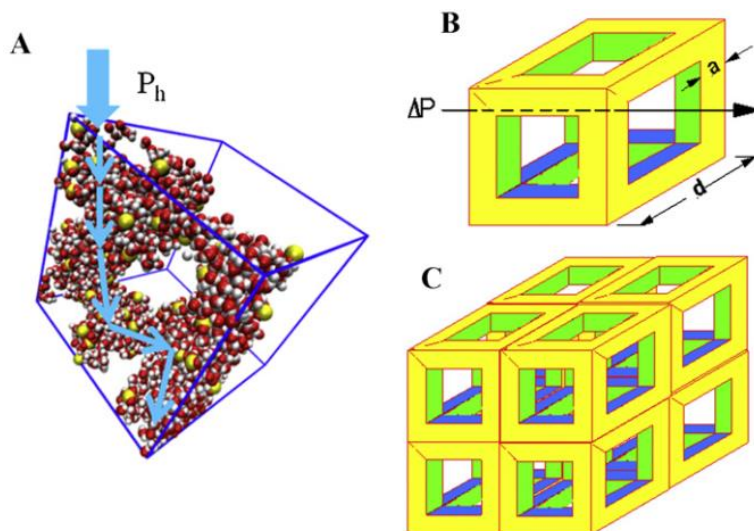


Figure 1.17. (a) structure of Nafion predicted through molecular dynamics with $\lambda = 15 \text{ H}_2\text{O}/\text{SO}_3^-$, only water and sulfonic groups are shown. (b) a unit cell of the simplified model for Nafion assuming a geometrically regular structure, and (c) connected network unit cells makes a continuous channel network. Reprinted with permission from reference 57. Copyright 2012 Elsevier.

For alkaline anion exchange membranes (AAEMS), little is presently known with regard to the role of water and morphological changes. Recent investigations have shown that improving the microphase separation, for instance, brought about through additional alkyl chains, resulted in well-connected channels observed in transmission electron microscopy analysis, which significantly improved ion conductivity (from 16.2 mS/cm to 53.9 mS/cm at room temperature).⁵⁸ Further work is needed to understand the morphological changes that occur for different families of AAEM materials with respect to water content, however, it appears that good phase separation of the material, as is present in perfluorosulfonic acid membranes, is a desirable property.

1.4.2. Oxygen transport through ionomer

When a solid polymer electrolyte is used as a membrane, there is a desire for low gas permeability since excessive gas crossover through the membrane would result in losses of efficiency as no electrons would pass through an external circuit to produce meaningful work. As an ionomer in the catalyst layer, however, facile gas permeability facilitates reactant transport through ionomer-covered catalyst sites. Gasteiger *et al.* found boundary limits for solid polymer electrolyte gas permeability, where the lower oxygen permeability limit was stated for the ionomer in the catalyst layer ($10^{-16} \text{ mol}\cdot\text{cm}/\text{cm}^2\cdot\text{s}\cdot\text{kPa}$ at 80°C) and the upper permeability limit corresponded to oxygen permeability through the membrane ($10^{-12} \text{ mol}\cdot\text{cm}/\text{cm}^2\cdot\text{s}\cdot\text{kPa}$ at 80°C).³¹

Two physiochemical properties that directly affect the rate limiting mass transport for oxygen reduction are the diffusion and solubility of oxygen. The diffusion and solubility of oxygen through the ionomer in the cathode catalyst layer plays a direct role in the mass transport limiting current density, as can be seen from Fick's first law²:

$$i_{lim} = \frac{nFD_b c_b}{\delta}, \quad (1.18)$$

where i_{lim} is the limiting current density (A/cm²), n is the number of electrons transferred per molecule, F is Faraday's constant, D_b is the diffusion coefficient (cm²/s), c_b is the bulk solubility (mol/cm³), and δ is the thickness of the mass transfer boundary layer in cm. In this way it can be seen that the limiting current density increases with an increase in either the diffusion coefficient or solubility, or a decrease in the boundary layer thickness. The product of D_b and c_b is the permeability.

Ex-situ solid state electrochemical techniques provide a means to study the oxygen reduction reaction at Pt | ionomer interfaces under conditions of specific temperature, pressure, and RH. Previous electrochemical studies have shown that mass transport through perfluorosulfonic acid (PFSA) membranes is dependent upon oxygen solubility in the hydrophobic, fluorinated domains (polymer backbone) and its transport into, and diffusion through, aqueous domains (sulfonic sidechains).^{59,60} Oxygen diffuses rapidly through the water channels that become wider and better connected at higher hydration, where it dissolves more readily in the hydrophobic domains.⁶¹ The relatively high rate of oxygen permeation through PFSA ionomer is attributed to the relatively high oxygen solubility afforded by fluorine domains and high diffusion coefficient afforded by a well-connected hydrophilic network.^{59,62} Pioneering work by Srinivasan and coworkers demonstrated both a temperature and pressure dependency on the ORR activation energy, oxygen diffusion coefficient, and oxygen solubility in PFSA ionomer membranes.^{63,64} The technique was subsequently used to determine kinetic and mass transport parameters for ionomers with different ion exchange capacities and polymer structures.^{62,65–68} Membranes with higher equivalent weights (correlating to ion exchange capacity) were found to have higher oxygen permeabilities attributed to the increased water content, suggesting that water plays a critical role in gas transport through ionomers.⁶² Of note is the fact that previous works relied on conditions in which the ambient environment was fully saturated (100% RH) and where water was often wicked to the membrane to maintain its fully hydrated state. These conditions are not truly representative of PEMFC conditions but were adopted because of difficulties in overcoming high ionic resistances observed in solid state electrochemical cells under low RH conditions.

Zhang et al. reported oxygen permeability values for a PFSA-based membrane electrode assembly where the humidity of the membrane was controlled.⁶⁹ While the oxygen diffusion coefficient and oxygen solubility could not be decoupled based on the measurement technique, oxygen permeability was found to decrease by more than one half when the relative humidity was decreased from 100 to 25%. As well, studies based on limiting current techniques indicate that as Pt catalyst loading in the CCL is reduced, oxygen mass transport resistance in, and through, the PFSA ionomer increases.^{70–72} A study by Tabe *et al.* supports this contention - that oxygen mass transport resistance through the ionomer film in the cathode catalyst layer affects fuel cell operation at high current densities, where improving gas transport can lead to reduced platinum usage.⁷³ It is also hypothesized that oxygen mass transport is hindered by a resistance at the gas/ionomer interface, which becomes increasingly dominant as ionomer film thickness is reduced.^{74–76} This resistance, attributed to oxygen gas diffusing into ionomer films toward platinum catalyst sites, has renewed interest in the area of oxygen mass transport.^{74,77,78}

Figure 1.18 shows a typical cathode catalyst layer where platinum particles can be exposed to open pore spaces or have some degree of coverage with ionomer. In the open pore spaces oxygen transport is facile, with a diffusion coefficient in air on the order of $\sim 0.2 \text{ cm}^2/\text{s}$. A triple phase boundary is desirable for catalyst sites, where access to reactants is provided by carbon (electrons), ionomer (protons), and pore space (oxygen gas in, liquid water out). At high current densities or in a poorly designed CCL liquid water flooding can occur which impedes normal oxygen mass transport, resulting in limiting current densities as reactant ingress and product egress are hindered.^{38,50} Oxygen transport through water is less than in air, with diffusion coefficients on the order of about $4 \times 10^{-5} \text{ cm}^2/\text{s}$, yet still faster than through solid ionomer. As discussed more in depth in the following chapters, typical oxygen diffusion coefficients are on the order of $\sim 10^{-6} \text{ cm}^2/\text{s}$ or less, depending on ionomer water content. Of the components in the cathode catalyst layer, oxygen transport through the ionomer is rate limiting, and oxygen diffusion coefficients thus reported are considered as “effective” diffusion coefficients, in that the diffusion coefficient changes based on the interfacial morphology and its effect on oxygen reduction. The effective oxygen diffusion coefficient is heavily dependent on the conditions at the interface. For instance, the tortuosity of the electrolytic pathways (hydrophilic water filled channels for perfluorosulfonic acid type ionomers), the orientation of which has been observed to change with relative humidity, will directly affect the effective diffusion coefficient. The interfacial morphology, which changes depending on the type of polymer (such as perfluorinated versus hydrocarbon) directly affects the resulting electrochemically-determined oxygen diffusion coefficient.

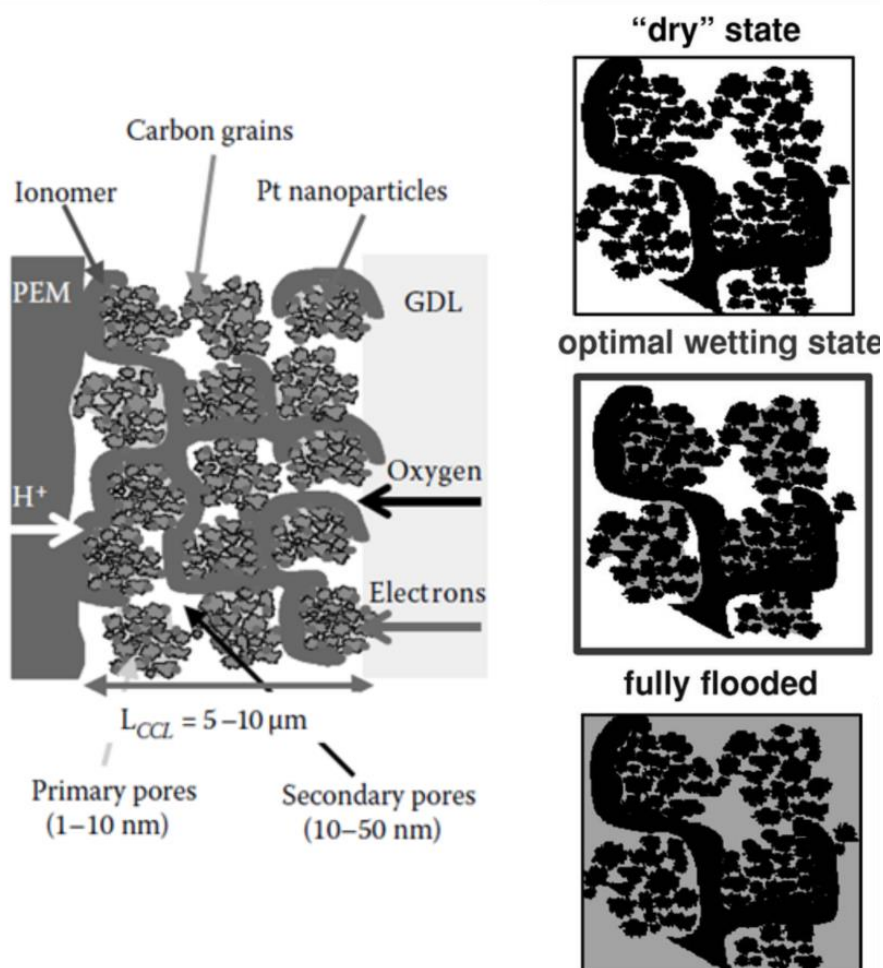


Figure 1.18. (Left) Schematic of cathode catalyst layer structure where platinum nanoparticles on carbon have metal-facing interfaces with both pore spaces as well as ionomer. (Right) Carbon agglomerates in the dry state, in an optimally wetted state with water in the primary pores, and fully flooded state (water in primary and secondary pores). Reprinted with permission from reference 50. Copyright 2006 Electrochemical Society.

A schematic illustrating the interfacial and bulk resistances that O_2 gas experiences travelling to Pt sites is shown in Figure 1.19. Oxygen molecules must move through ionomer when pore-space exposed platinum sites are already proceeding with the ORR under mass transport limiting conditions for high current loads. As well, oxygen gas has to contend with product water filling pore spaces at high current densities. For the transition through ionomer, O_2 gas must first diffuse through the pore space/ionomer interface, then through the bulk ionomer, and finally contend with the ionomer/Pt interface contact resistance. Not shown in Figure 1.19 is a thin intermediate layer of liquid water which exists between the ionomer and platinum sites during oxygen reduction. A molecular dynamics study

by Nouri-Khorasani *et al.* has shown that the thin water layer, which acts as a medium for proton transport, facilitates a high concentration of protons at the platinum oxide surface which has a direct implication for the rate of the oxygen reduction reaction.⁷⁹

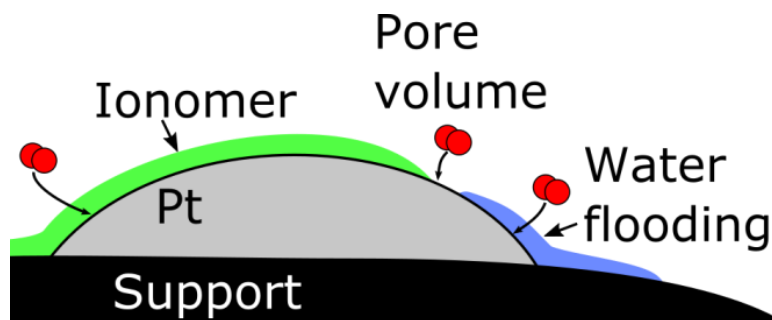


Figure 1.19. Schematic of O_2 transport from pore space to Pt (not to scale). Oxygen can transit through a thin (~ 2 nm) ionomer layer, directly through a pore-volume exposed region, or through a film of liquid water in the pore.

Recent works have indicated that as relative humidity is decreased for a thin (~ 100 nm) ionomer film, oxygen resistance increases more at the interface than in the bulk (Figure 1.20).^{80,81} This suggests that the limiting step for the observed oxygen resistance is for oxygen diffusing into the ionomer from the gas phase rather than through bulk transport once inside the ionomer. Kudo *et al.* have recently indicated that gas transport through the thin ionomer film to catalyst sites does not significantly differ from bulk materials, however the ionomer/catalyst interface provides a significant (10-20 kJ/mol) energetic barrier for gas permeation.⁸⁰

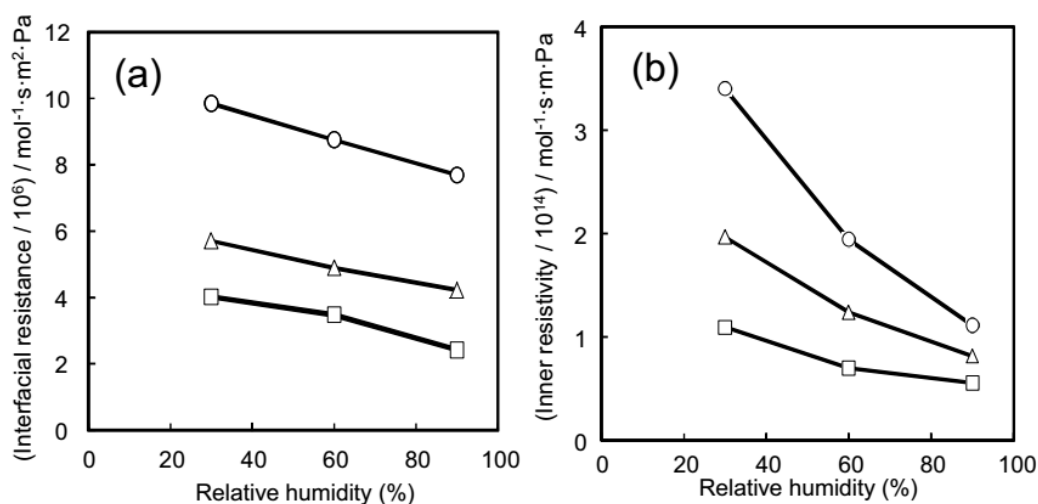


Figure 1.20. Humidity dependent (a) interfacial resistance and (b) bulk resistance to oxygen transport in thin Nafion film at 313 K (circle), 333 K (triangle), and 353 K (square). Reproduced with permission from reference ⁸⁰. Copyright 2016 Elsevier.

There are two methods commonly used for measuring oxygen gas permeability through ionomers, either the time-lag method after applying a pressure gradient on one side of a thick ($>10\ \mu\text{m}$) membrane, or solid state electrochemistry using a platinum electrode pressed against an ionomer film or membrane.^{61,65,66,68,82} Electrochemical measurements have been an accepted method of determining oxygen mass transport parameters because of their ability to probe catalyst-ionomer interfacial properties rather than the forced pressure-gradient measurement which is more suited for bulk membrane gas crossover properties. Similarly, electrochemical methods allow for the use of thin ionomer films closer to reality in a catalyst layer, where differential pressure techniques are limited to greater thicknesses to avoid mechanical puncturing during vacuum.

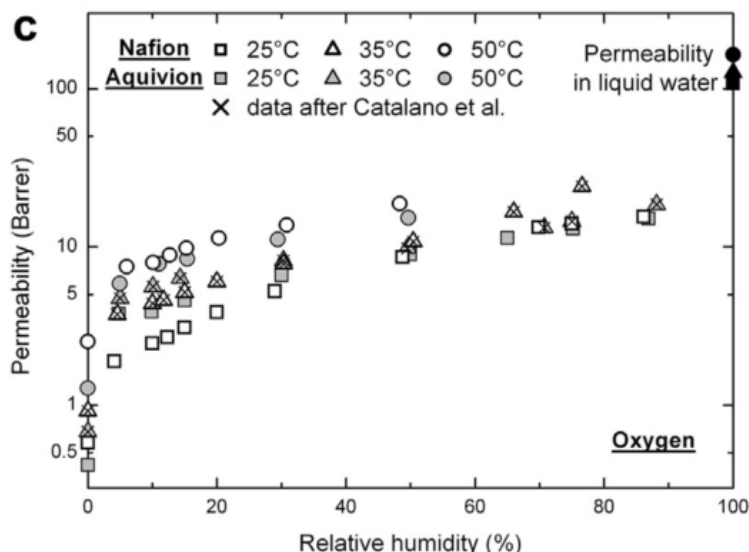


Figure 1.21. Oxygen permeability through humidified Nafion and Aquivion (shortened side-chain) membranes. Printed with permission from reference⁸³. Copyright 2013 Elsevier.

The pressure differential method was applied to Nafion membranes as well as short-side chain membranes by Baschetti *et al.*, who showed, in Figure 1.21, that oxygen permeability decreases with decreasing relative humidity.⁸³ The same method was applied by Ohira *et al.*, who showed similar behaviour for a similar series of polymers. However, the pressure differential method is most applicable for bulk properties of membranes, as ionomer films have been observed to reorganize their interfacial and bulk morphology in the presence of different substrates.⁸⁴ In the case of a morphological change, oxygen mass transport parameters would likewise be affected in some way.

Added complexity for oxygen transport through ionomer films on platinum surfaces comes from sulfonic group adsorption on the platinum surface. Kudo *et al.* have shown that the existence of adsorbed species on platinum has a potential dependence that impedes diffusion pathways or active

surface domains for oxygen reduction.^{80,85} Recent works have shown that drying Nafion films in contact with a platinum surface results in a reversible transformation of the disassociated sulfonate ions ($-\text{SO}_3^-$) into the dehydrated sulfonic acid group ($-\text{SO}_3\text{H}$). A small amount of the dehydrated sulfonic acid, however, decomposed to atomic sulphur in the presence of a platinum surface which led to an irreversible adsorption to the surface.⁸⁶ Liu and coworkers recently proposed a notion that sulfonic group adsorption on the platinum surface is to blame for the ionomer/electrode interfacial resistance to gas transport, rather than some dense hydrophobic skin at the platinum/ionomer interface.⁸⁷ The adsorption of sulfonic groups is dependent on the potential of the platinum surface being clean or oxidized. Electrochemical quartz crystal microbalance studies have shown an increase in electrode mass as platinum oxide is reduced which was attributed to adsorption on the clean electrode surface.⁸⁸ However, as the platinum surface is oxidized even to a monolayer, at +0.7 V versus reversible hydrogen electrode, desorption of the sulfonic group was observed.

1.5. Thesis outline

Voltage losses under high current density operation due to mass transport limitations are a large hindrance in the development of low catalyst loading fuel cells. The resistance attributed to oxygen permeating through thin ionomer films in the cathode catalyst layer has been observed to increase as catalyst loading decreases. The objective of this research is to gain insight into the electrochemical interface which is present in fuel cell catalyst layers. For this purpose, several ionomers are characterized with a focus on the ion exchange capacity, polymer structure, water content, and oxygen mass transport properties. Throughout this thesis, results are obtained for both membranes and as cast thin films on the electrode surface. For clarity, the term membrane is used interchangeably to refer to as-received membranes as well as cast films.

Chapter 2 is based on results from two individual publications that report the electrochemical characterization of as-received polyfluorosulfonic acid membranes (Nafion 117 and Nafion 211) and ionomer films cast from a perfluorosulfonic acid dispersion (DE2020) directly on the electrode. Oxygen reduction-limited current transients were measured using either a 5 or 50 μm microdisk platinum electrode, based on the methodology of Beattie *et al.*⁶⁵ Oxygen mass transport parameters are reported under controlled temperature, pressure, and relative humidity using an environmental chamber. The effect of interfacial water generation during oxygen reduction limiting potentials on resulting oxygen mass transport properties is investigated. The data is discussed in the context of membrane/electrode interfacial morphology and water content.

Chapter 3 is based on my published work which describes the electrochemical characterization of as-received Nafion 211 and as-cast DE2020 films. Cyclic voltammetry was used to investigate the effect of relative humidity on the electrochemically active surface area of the membrane in contact with the electrode. Sampled current voltammetry is utilized to determine the potential where oxygen reduction is mass transport limiting at a specific relative humidity. Potential step chronoamperometry is employed to obtain oxygen mass transport parameters under low relative humidity. The data is discussed in the context of interfacial morphology and water content.

In Chapter 4, the knowledge gained from previous chapters is applied toward the electrochemical characterization of a series of novel alkaline anion exchange hydrocarbon ionomers (hexamethyl-*p*-terphenyl polymethylbenzimidazole, HMT-PMBI) cast directly on the electrode.³³ Dynamic vapour sorption is used to measure the water content in cast ionomer films at specific relative humidities. The methods described in Chapter 3 are applied in a similar fashion and the results are discussed in the context of ion exchange capacity and water content. The oxygen mass transport properties of HMT-PMBI are compared to a commercially obtained quaternary ammonium-based membrane. A numerical model is also presented wherein the effect of the oxygen reduction diffusion field hitting the air/membrane interface is accounted for.

Chapter 2. Time-dependent mass transport for O₂ reduction at the Pt | perfluorosulfonic acid ionomer interface

This chapter is reproduced from two published papers: (1) David Novitski, Zhong Xie, and Steven Holdcroft, *ECS Electrochemistry Letters*, **2015**, Vol. 4 (1) F9-F12 with permission from The Electrochemical Society. From this paper, Z. Xie contributed in the solid state electrochemical cell design and setup in Section 2.2.4. (2) David Novitski and Steven Holdcroft, *ACS Applied Materials and Interfaces*, **2015**, Vol. 7 (49) 27314-2723 with permission from The American Chemical Society.

2.1. Introduction

Proton exchange membrane fuel cell (PEMFC) catalyst layers typically employ an ionomer component to reduce ionic resistance and improve electrochemical kinetics.^{89,90} Recent studies reveal the ionomer in the catalyst layer may be present as an ultrathin (~2 nm) film, and ex-situ contact angle measurements have indicated that such cast films undergo a surface morphological reconstruction from hydrophobic to hydrophilic upon exposure to liquid water. Moreover, the reconstruction is observed to have a time-dependency proportional to film thickness, where a 10 nm cast film required 24 hours for surface reorganization to occur, a 30 nm film required 48 hours.⁵⁵ Exposure to water vapour did not trigger this surface reconstruction, which is attributed to sulfonic group mobility toward the surface.⁵⁵ The existence of a hydrophobic surface at the membrane/vapour interface compared to the membrane/liquid interface has been supported by molecular dynamics simulations⁹¹ as well as grazing-incidence small angle x-ray scattering studies.^{47,92}

The nature of these morphological reorganizations at the surface of the ionomer film is of considerable interest for understanding electrochemical mass transport at the ionomer | Pt interface.¹⁴ However, there is little evidence concerning the role of these reorganizations on actual Faradaic electrochemical activities. Overall, the complex morphological changes at ionomer surfaces are of increasing interest, where variables such as film thickness, substrate, and film preparation result in markedly different outcomes for the resulting ionomer properties.^{47,93–95} Grazing incidence x-ray diffraction and small angle x-ray scattering performed Tang et al. have shown a fluorine-rich 4 nm

region at the membrane/air interface which has about 40% higher crystallinity over the bulk membrane.⁹⁶

The equilibration time for perfluorosulfonic acid polymers is long due to the complex phase separation of the semicrystalline hydrophobic backbone and the ionic water-rich domains. Changes in morphology and water uptake have been reported for membranes that have been equilibrating for days or weeks.^{94,97–99} PFSA polymer exhibited a mechanical relaxation that was humidity-, temperature-, and time-dependent over several days.¹⁰⁰ As well, a time-dependent relationship in PFSA has been observed for conductivity and morphology changes.¹⁰¹ Therefore it is more appropriate to refer to an equilibrated membrane as in quasi-equilibrium rather than at a true steady-state.

In the present work, a solid state electrochemical cell was constructed which was capable of operation under reduced relative humidity in order to determine the absence or presence of a time-dependency for oxygen mass transport in ionomer membranes that are not fully hydrated. The experiments were designed to investigate the different time-dependencies for extruded membranes (Nafion 117), cast membranes (Nafion 211), and ionomer cast directly onto the working electrode (DE2020) in order to probe the effect of interfacial morphologies.

2.1.1. Microdisk electrodes

A microelectrode is defined as an electrode with a characteristic dimension on the scale of micrometer or sub-micrometer. At the micrometer scale, the overall volume of electrolyte is much larger than the perturbing electrode, which results in an electrode which can probe the system of interest rather than change the overall composition. Microelectrodes exhibit high current densities at low total currents as well as the ability to attain steady state under conditions usually not possible with macroelectrodes. There are many geometries of microelectrode such as disk, hemispherical, or band. Microdisk electrodes are possibly the most common microelectrode because they are simple to fabricate, usually comprised of a metal wire encapsulated in soft glass which is polished away to expose a circle of active electrode area with a critical dimension r_0 on the order of several microns.²

Microelectrodes are advantageous in that they are able to operate in both the short and long timescales, where the current response following perturbation is able to be analytically solved using geometry-specific equations, as discussed in more detail in Section 2.2.3. Microdisk electrodes are used in this work as the solid polymer electrolytes used throughout the thesis exhibit low conductivities, especially at low humidification conditions. This in turn leads to an increase in iR drop

(current*resistance) which prohibits the use of conventional-sized electrodes. In microelectrodes the currents are typically very small, on the order of nanoamperes, which allows for relatively resistive samples (up to megaohms) to be analyzed while not significantly impacting the uncertainty in the experiment.

Lastly, the dimension of microelectrodes allow operation at short timescales compared to macroelectrodes. The RC time constant (the product of the solution resistance, R , and the double layer capacitance, C , of the working electrode) is the lower limit for electrochemical measurements.¹⁰² After applying a potential, the charge on the metal surface changes which results in a reorganization of ions and solvent dipoles at the solution side. This results in a flow of electrons which are capacitive or charging in nature. Meaningful data can only be obtained when charging of the interface is mostly complete, at timescales typically greater than 5 time constants,. The solution resistance for a disk shaped microelectrode is given by

$$R = \frac{1}{4\kappa r_o} \quad (2.1)$$

where the solution resistance, R , increases as the electrode radius, r_o , decreases. In Eqn. 2.1, κ is the conductivity of the electrolyte. In this way, decreasing the electrode size does not lead to the ability to decrease the charging constant. However, the double layer capacitance for a disk microelectrode is given by

$$C = \pi r_o^2 C_d \quad (2.2)$$

where C_d is the double layer capacitance specific to the electrode. By decreasing the size of the working electrode the capacitance decreases by a factor r_o^2 . This relationship allows the utilization of microdisk electrodes for either extremely short (nanosecond) timescales, or short (millisecond) timescales with more resistive electrolyte media such as ion conducting polymers.

2.2. Experimental

2.2.1. Materials

Nafion 117 and Nafion 211 membranes (cut to 2 cm² squares, Sigma Aldrich) were soaked in 3 wt% hydrogen peroxide at 80 °C for one hour in order to remove inorganic impurities followed by rinsing in Millipore (Milli-Q 18 MΩ) water. Protonation of membranes was achieved by soaking in 0.5 M

H₂SO₄ at 80 °C for one hour, followed by rinsing and soaking in Millipore water at 80 °C for one hour to remove residual acid. Nafion 117 samples were stored in Millipore water at 50 °C overnight before insertion into the electrochemical cell. Nafion 211 membranes were allowed to equilibrate in Millipore water at 70°C for several hours before being mounted in the electrochemical cell. DE2020 (Ion Power) 20 wt% PFSA dispersion was used as-received and cast directly onto the working electrode.

2.2.2. Cyclic voltammetry

Cyclic voltammetry is a method of applying a triangle wave repeatedly in an electrochemical cell, typically first sweeping the potential reductively, known as a cathodic sweep, and then oxidatively in an anodic sweep. In this way, thermodynamics of redox processes occurring within the selected potential range can be ascertained as well as information on reaction reversibility and adsorption processes at the electrode interface. A potentiostat is used to measure the current response during the triangle sweep, resulting in a cyclic voltammogram (CV), where an example sweep of platinum in 0.5 M H₂SO₄ is shown in Figure 2.1. From positive potentials (1 V vs. Reversible Hydrogen Electrode, RHE) sweeping negative (cathodic, negative current), the first peak near 0.8 V vs. RHE corresponds to platinum oxide reduction while the series of peaks starting around 0.4 V comes from hydrogen adsorbing on the platinum surface. Any further travelling into more negative potentials will result in large currents and hydrogen gas evolution. Sweeping anodically (positive currents from 0.05 V), the first series of peaks come from desorption of hydrogen from platinum followed by platinum oxide formation near 0.8 V vs. RHE.

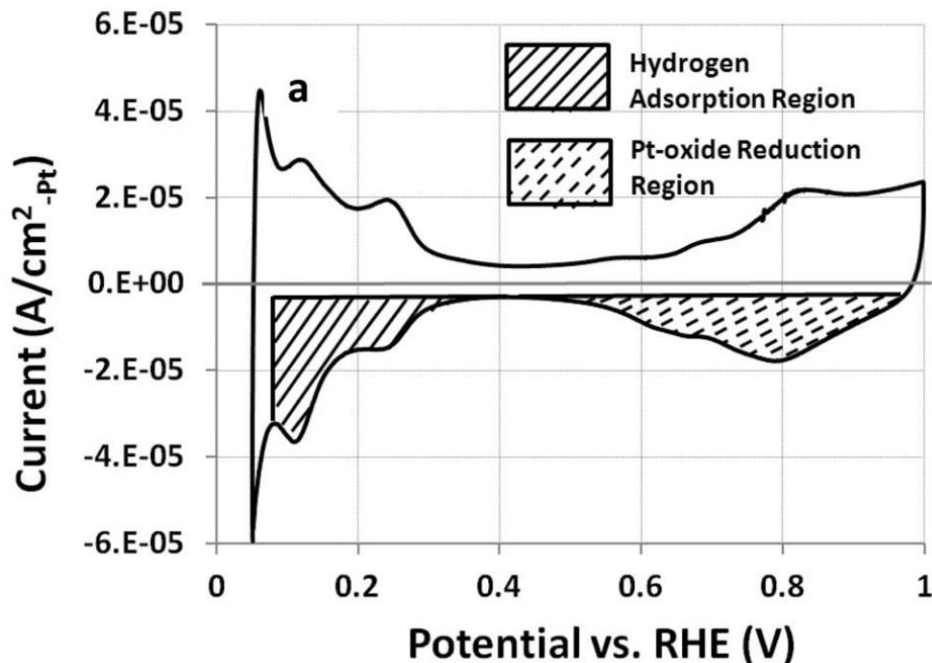


Figure 2.1. Cyclic voltammogram of a Pt/C membrane electrode assembly at 80 °C and 100% RH versus reversible hydrogen electrode (RHE). Reprinted with permission from reference ¹⁰³. Copyright 2012 Electrochemical Society.

From Figure 2.1, the charge associated for the hydrogen adsorption (solid stripes in figure) or desorption, when corrected for double layer capacitance, corresponds with the adsorption or desorption of one hydrogen atom with one platinum atom at the electrode surface (Q_h). The associated charge for a one-to-one H-Pt adsorption per unit surface area (Q_h^*) is calculated dependent on the metal atom distribution on the surface (crystal face). For a polycrystalline metal surface, Q_h^* is the average value between the main low-index faces and is accepted to be $210 \mu\text{C}/\text{cm}^2$ based on the assumption that the density of Pt atoms is $1.31 \times 10^{15} \text{ atoms}/\text{cm}^2$.¹⁰⁴ The real surface area, A , which accounts for atomic scale peaks and troughs on the electrode surface is given as:

$$A = \frac{Q_h}{Q_h^*} \quad (2.3)$$

2.2.3. Chronoamperometry

Chronoamperometry is the investigation of current over time after an excitation signal is applied to an electrode in the form of a square wave. The current is the Faradaic response which is the result of an instantaneous application of a constant potential (Figure 2.2) which is sufficient to reduce all of a reactant species at the working electrode surface such that the subsequent rate of reaction is limited to the rate of diffusion through the electrolyte medium to the electrode surface.² This is a diffusion limited

process as the other contributions of mass transport, notably migration (movement of charged species) and convection (movement of solvent) are experimentally controlled and do not contribute to the system.

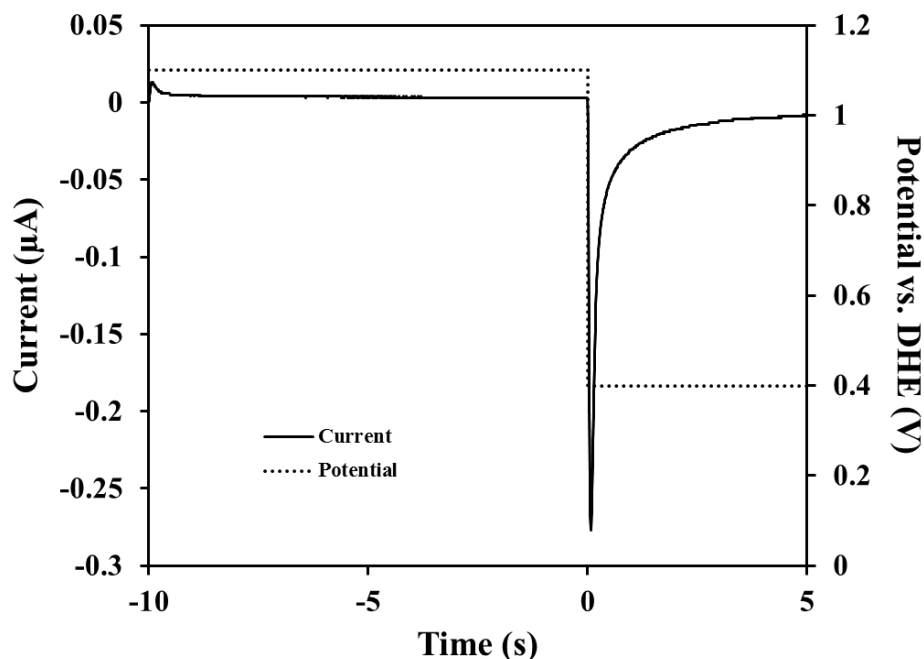


Figure 2.2. Potential step chronoamperometric measurement with decaying current response following mass-transport limiting potential step.

The equations that exist to describe this current for a microdisk electrode are known for the limits of zero and infinite time. Specifically, the Cottrell equation,¹⁰⁵ derived from Fick's laws, describes the current for the zero time limit:

$$I(t \rightarrow 0) = nFc_b r^2 \sqrt{\frac{\pi D}{t}} \quad (2.4)$$

and for long times, the Saito equation¹⁰⁶ describes the steady-state current:

$$I(t \rightarrow \infty) = 4nFc_b D_b r \quad (2.5)$$

where I is current (amperes), n is the number of electrons transferred (positive for oxidation, negative for reduction), F is Faraday's constant (96,485 C/mol), c_b is the reactive species concentration/solubility (cm³/mol), r is the electrode radius (cm), D_b is the bulk reactive species diffusivity coefficient (cm²/s), and t is time (s).

For a microdisk electrode configuration there is a current contribution from both equations, such that the current at a microdisk electrode is defined by the Cottrell equation:

$$I(t) = \frac{nFAD_b^{0.5}c_b}{\pi^{0.5}t^{0.5}} + 4nFc_bD_br, \quad (2.6)$$

where the parameters have the same meaning as previously described. According to Winlove, the current response should be linear versus $t^{-1/2}$ within the boundary conditions set by Eqn. 2.7, so long as the relationship $1 > \tau^{-0.5} > 0.5$ is met.¹⁰⁷ Plotting I versus $t^{-1/2}$ allows for linear regression analysis to obtain the slope and intercept which can be used to determine the oxygen diffusion coefficient and oxygen solubility in the membrane, given by Eqns. 2.8 and 2.9, respectively. Oxygen permeability is the product of Eqns. 2.6 and 2.7. Plotting the current versus the inverse of the square root of time, a Cottrell plot (Figure 2.3) is obtained which remains linear in the short time region. In Eqns. 2.8 and 2.9 b corresponds to the y-intercept in the Cottrell plot, while m corresponds to the slope of the line.

$$\tau = \frac{4t}{r^2} \quad (2.7)$$

$$D_b = \frac{r^2b^2}{\pi m^2} \quad (2.8)$$

$$c_b = \frac{m^2}{nFr^3b} \quad (2.9)$$

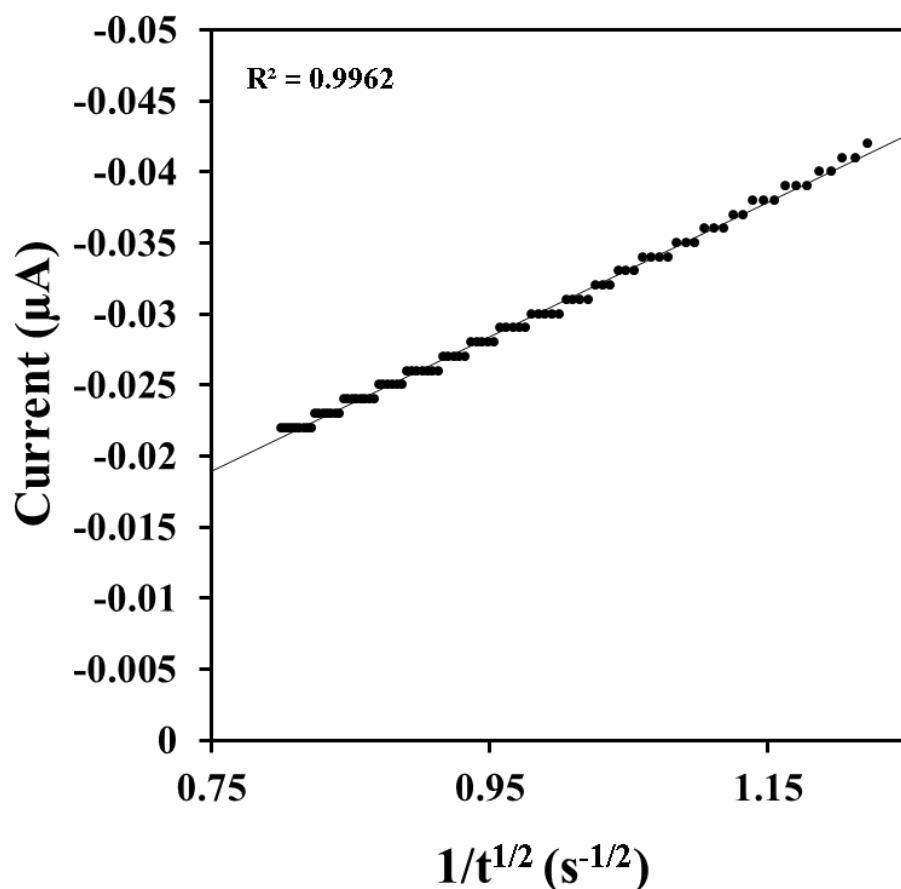


Figure 2.3. Cottrell plot with linear diffusion limited region shown. Linear regression analysis with the Cottrell equation gives parameters in Eqns. 2.6 and 2.7.

2.2.4. Electrochemical cell

The electrochemical cell, shown in Figure 2.4, was custom-designed based on a previously used cell and fabricated in-house.^{62,65,66} Individual electrode holders contained compression springs that allowed electrodes to achieve the required contact with the membrane for reproducible electrochemical activity, and were maintained in a secure position by a tension screw. The membrane was held in place, vertically, by a set of 4 screws and exposed to the ambient atmosphere on both sides. The electrochemical cell fit inside an Espec SH-241 environmental chamber in which the ambient air was held at a specific temperature and humidity. For the Nafion 117 experiment the temperature was held at 50°C and 70% RH under atmospheric pressure was used for all measurements. For the Nafion 211/DE2020 experiment the temperature was held at 70°C and the RH was held incrementally at 30%, 50%, 70%, and 90%. The electrode wires were routed to a PAR 283 (EG&G Instruments) potentiostat controlled through a GPIB-USB (National Instruments) connection

and the programming of the electrochemical experiments was controlled using CorrWare (Scribner Associates Inc.).

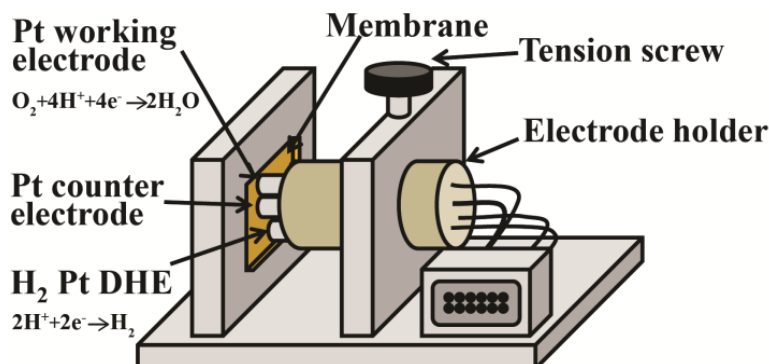


Figure 2.4. Diagram of electrochemical assembly showing electrodes in contact with membrane, which is exposed to vapour phase on both sides. Dynamic hydrogen electrode (DHE) used as reference.

The working electrode consisted of a 50 μm radius Pt microdisk (Sandfire Scientific Inc.) embedded in glass for the Nafion 117 experiments and a 5 μm radius Pt microdisk (BASi, Inc.) for the Nafion 211/DE2020 experiments. Both electrodes were polished using 1, 0.3, and 0.05 μm alumina polishing compound (Buehler). Cyclic voltammetry (30 scans at 100 mV/s) in deaerated 0.5 M H_2SO_4 between 1.4 V and -0.23 V (vs. Ag/AgCl) (BASi Inc.) was performed to remove remaining polish and other impurities. In the Nafion 117 experiment the reference electrode employed was a dynamic hydrogen electrode (DHE).^{65,68,108} The DHE operates by having two platinum electrodes continuously electrolysing water (Eqns. 2.10 and 2.11), while taking the hydrogen evolving electrode as reference. Two electrodes comprising the DHE were connected to a 9 V battery in line with a 1.7 M Ω resistor to achieve a constant 2.04 V at 1.2 μA . The current draw of 1.2 μA was sustainable for long periods of time (thousands of hours) as a 9 V battery contains about 500 mAh lifetime. The high overpotential over the standard potential of 1.23 V was required for water oxidation to occur at a rate where adequate hydrogen evolution occurred at the cathode to be used as reference. The counter electrode was a high surface area platinum mesh affixed to the end of a glass tube. Electrodes were placed in contact with the membrane and allowed to equilibrate for 5 days in the environmental chamber before measurements were performed. All potentials are reported versus DHE, unless otherwise noted. In the Nafion 211/DE2020 experiments, as will be discussed more thoroughly in section 3.3.1, a 2-electrode system was employed where the reference electrode was a platinized platinum mesh which also acted as the counter electrode. For the Nafion 211/DE2020 experiments the potentials are referenced versus the Pt pseudo-reference.





2.2.5. Nafion 117 experiment protocol

The experiment was designed hierarchically, as outlined in Figure 2.5, with one individual potential step measurement consisting of subjecting the Pt working electrode to 2 minutes rest at open circuit potential (OCP) (+0.96 to +0.98 V vs. DHE) followed by 10 seconds at +1.1 V (no Faradaic processes occurring), followed by a potential step to +0.4 V for 5 seconds during which time mass transport limited ORR occurs. The initial 2 minutes at OCP was necessary as potential step measurements taken without any rest time at OCP were irreproducible.

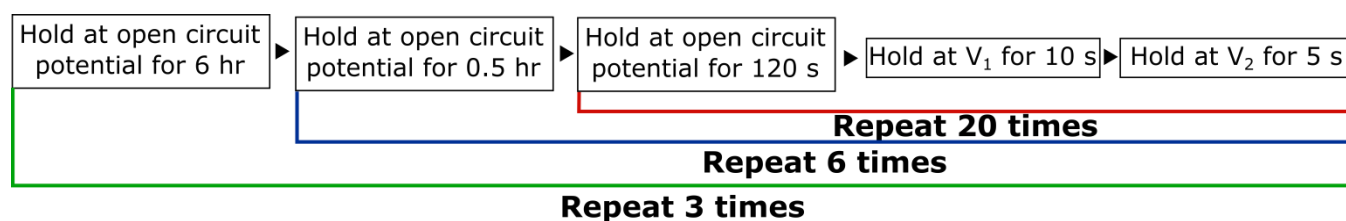


Figure 2.5. Potential step, chronoamperometric profile where open circuit is held for 6 hours followed by 20 back-to-back measurements highlighted in red. After this initial 20 sets post-6 hours, a hold at 30 minutes open circuit is made followed by the same 20 measurement sets highlighted in red. The 30 minute OCP test is performed 6 times, as highlighted by the blue line. This experimental procedure is repeated 3 times, as shown by the green line.

One “set” of measurements consisted of subjecting the Pt microdisk to a rest time at OCP for 30 minutes, followed by 20 individual measurements as described above. One “batch” of measurements consisted of 6 hours open circuit potential (~0.96-0.98 V), followed by 6 “sets” run back-to-back. In other words, for each *batch* of measurements, the first set of 20 measurements reports on changes in electrochemical response after 6 hours exposure to OCP. The next 6 sets (20 measurements each set) report any change in the response after each 30 minutes exposure to OCP. The ORR parameters extracted from each potential step measurement were correlated to the measurement number in order to examine the time dependency of extracted mass transport parameters. A complete experiment consisted of 3 “batches”, such that the effect of holding the electrode for 2, 30, and 360 minutes at OCP on the resulting oxygen mass transport parameters was investigated.

2.2.6. Nafion 211 and DE2020 experiment protocol

For Nafion 211 and DE2020 experiments, the working electrode was held at open circuit potential for 5 minutes followed by a series of 5 back-to-back chronoamperometric measurements at potential V_i for 10 s, followed by application of V_f for 5 seconds.

2.3. Results and discussion

2.3.1. Electrochemically active surface area:

The electrochemically active surface area of the working electrode was calculated by integrating the current response correlating to the hydrogen desorption peak as described in section 2.2.2. A representative cyclic voltammogram of the Pt | Nafion 117 interface at 70% RH and 50°C is shown in Figure 2.6. The electrode roughness factor, or ratio between measured surface area and geometric surface area, is a way to quantify the peaks and troughs that exist at the atomic level on the electrode. The value should always be greater than one and relates to the real surface accessible to participate in electrochemical reactions. In the present investigation the platinum electrode roughness was ~ 2 , in agreement with values for polycrystalline Pt electrodes reported in literature.² Comparison of the CVs in Figure 2.6 before and after the experiment described in Figure 2.5 indicates no significant loss of electrochemically active surface area of the working electrode due to platinum dissolution during potential sweeps.¹⁰⁹ Cyclic voltammograms for platinum electrodes in contact with a solid membrane electrolyte such as Nafion have been reported to have diminished peaks in the hydrogen adsorption/desorption and oxygen reduction region.¹¹⁰ This has been attributed to a decrease in the accessibility of electrolyte to the atomic-scale features of the electrode, compared to aqueous H_2SO_4 solutions. The cyclic voltammograms shown in Figure 2.6 as well as in Chapters 3 and 4 differ from the ideal aqueous electrolyte CV shown in Figure 2.1 for this reason.

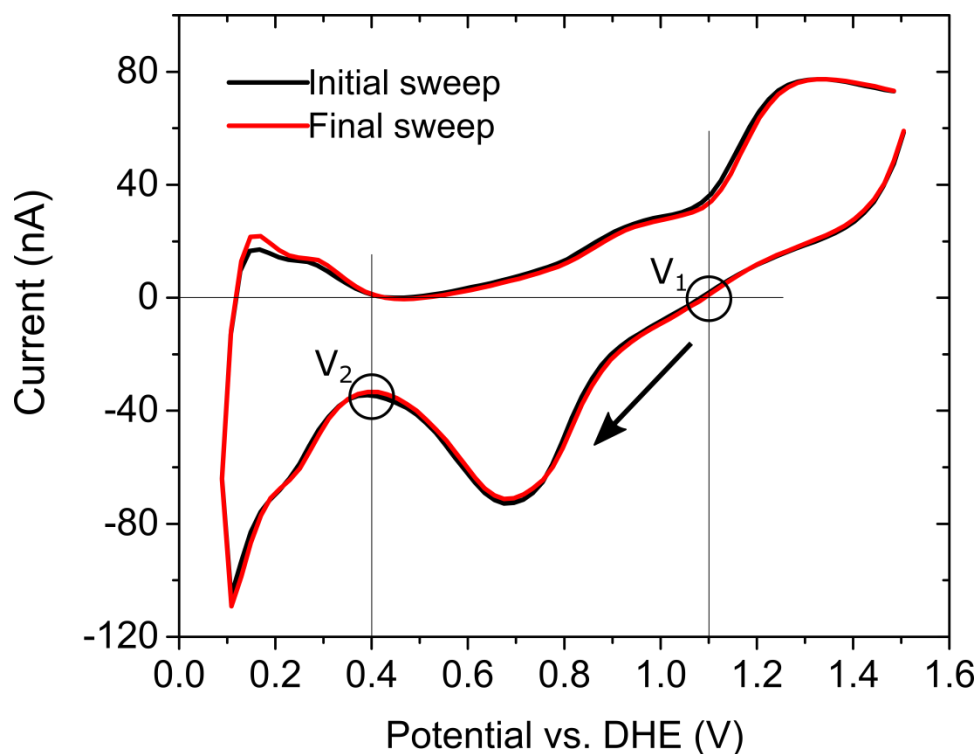


Figure 2.6. Cyclic voltammograms (100 mV/s) of a 50 μm radius Pt microelectrode on Nafion 117 equilibrated at 70% RH and 50 $^{\circ}\text{C}$ in air. Platinum mesh counter electrode and dynamic hydrogen reference electrode. 20th scan shown before experiments run (black line), and after (red line). V_1 corresponds to the initial potential, V_2 corresponds to the final potential where oxygen reduction is mass transport limited.

A potential step, chronoamperometric measurement under the same conditions as described in section 2.2.5 produced a current spike comprised of both capacitive charging and Faradaic ORR (Figure 2.2) that quickly decays. The chronoamperometric data was converted to a Cottrell plot of I vs. $t^{1/2}$ for the time interval 0.7 to 1.4 s. D_b , c_b , and $D_b \cdot c_b$ values extracted for all sets and batches of chronoamperometric measurements are shown in Figure 2.7, Figure 2.8, and Figure 2.9, respectively, and include 2 min, 30 min. and 6 h OCP rest times. The x-axis lists measurement number following the first chronoamperometric measurement taken after either 30 minutes or 6 hours OCP rest time. The presented data are averaged over two batches of data, showing good reproducibility in the system with very little standard deviation. For Figure 2.7 and Figure 2.8 the error bars correspond to the standard deviation for oxygen diffusion coefficient and solubility parameters obtained from linear regression analysis in two experimental runs. For Figure 2.9 the error bars correspond to the added relative errors from the oxygen diffusion coefficient and solubility values. The striking feature is that D_b and $D_b \cdot c_b$ values increase over time after 6 h OCP rest time, reaching a steady state after ~ 10 chronoamperometric potential steps (1/2 a set). In the case of subjecting the electrode/polymer

interface to 30 min OCP, smaller decreases in D_b and $D_b \cdot c_b$ are observed, but which rise to steady state after 5 subsequent potential steps.

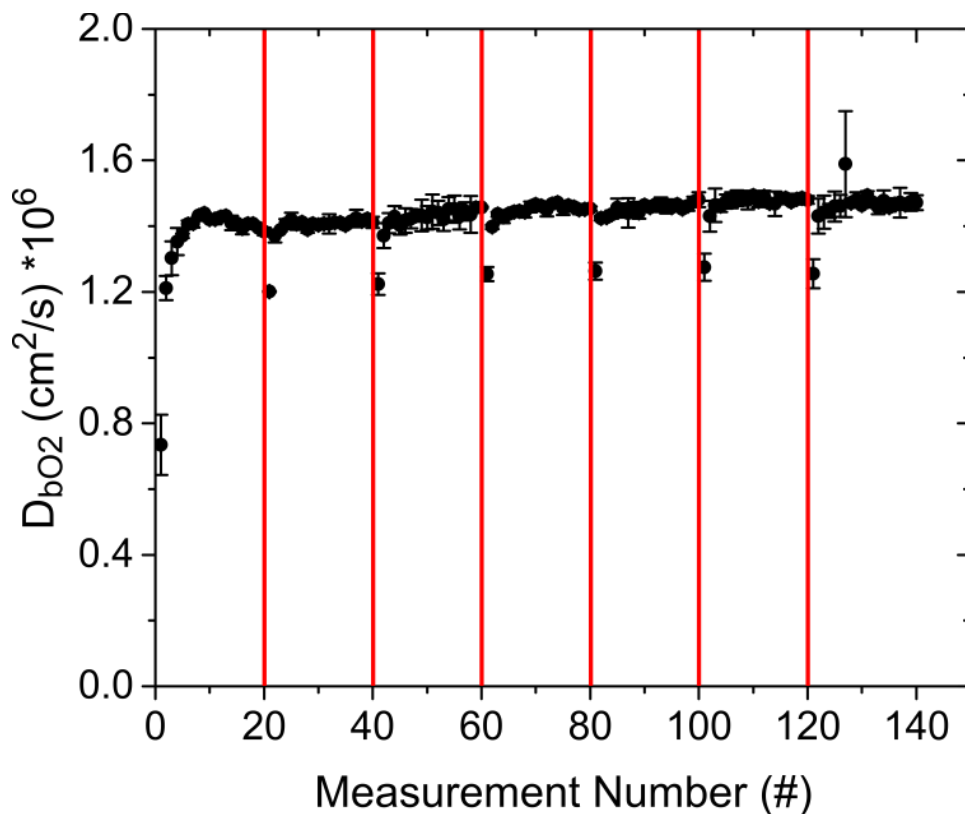


Figure 2.7. Oxygen diffusion coefficients averaged over two batches, where error bars represent the standard deviation from two runs. First set of 20 measurements result from 6 hours open circuit potential, second and subsequent columns (broken by red lines) represents 30 minutes open circuit potential.

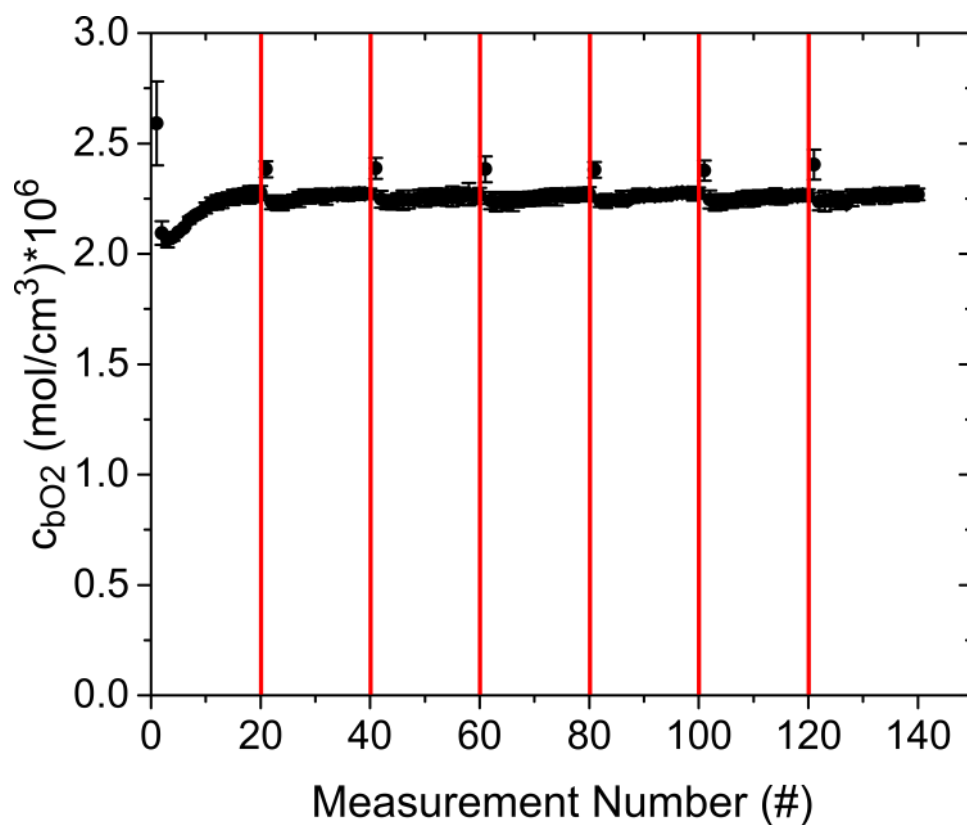


Figure 2.8. Oxygen solubility averaged over two batches, where error bars represent the standard deviation from two runs. First set of 20 measurements result from 6 hours open circuit potential, second and subsequent columns (broken by red lines) represents 30 minutes open circuit potential.

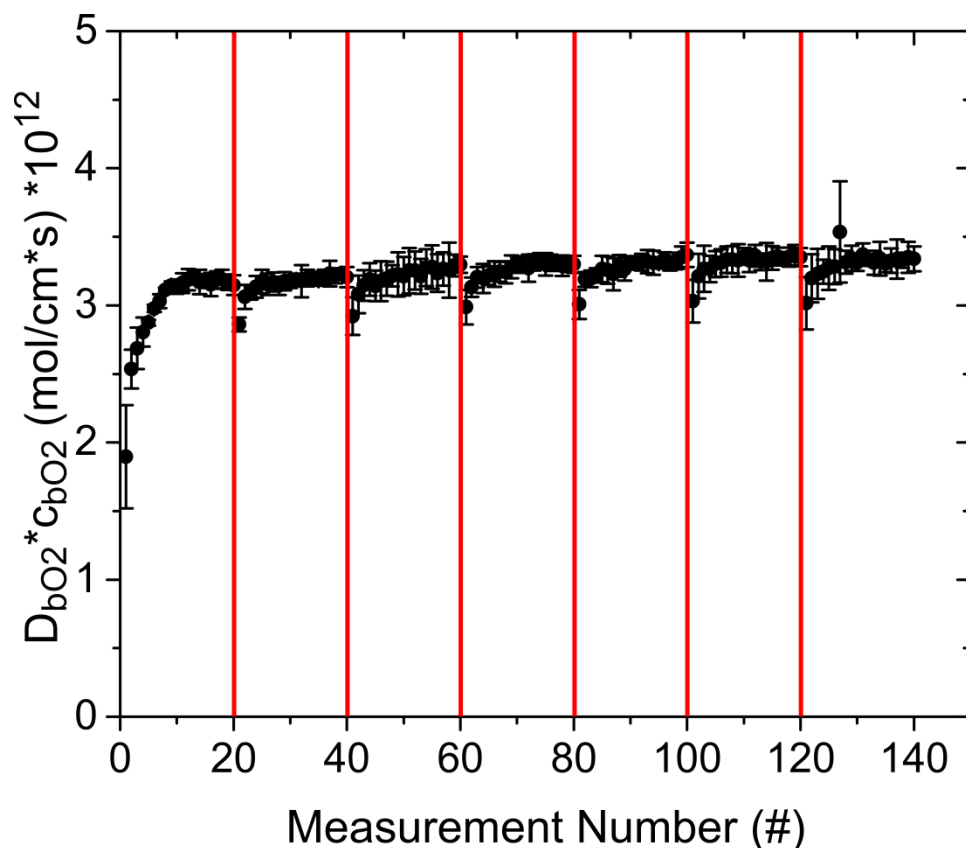


Figure 2.9. Oxygen permeability averaged over two batches, where error bars represent the added relative uncertainties from the diffusion coefficient and solubility. First set of 20 measurements result from 6 hours open circuit potential, second and subsequent columns (broken by red lines) represents 30 minutes open circuit potential.

The mass transport parameters are observed to decay to some initial point after subjection of the electrode/polymer interface to 30 min and 6 h at OCP. The phenomenon is entirely reproducible and was repeated several times with different Nafion 117 samples. A time interval of 2 min OCP did not result in a decrease in D_b , c_b , or $D_b^* c_b$ values. Oxygen mass transport parameters from both the water vapour equilibrated OCP relaxation state and the electrochemically induced steady state are presented in Table 2.1, with comparative values from literature.⁶⁵ Comparing the steady state values obtained at 70% RH to literature values taken at 100% RH and 2 atm O_2 reveals a lower oxygen diffusion coefficient at reduced humidity, congruent with expectations for ionomer systems where reduced hydration decreases the size of the hydrophilic channels and hinders oxygen diffusion.⁶⁵ Oxygen solubility values were found to be lower than literature values reported because of the ambient oxygen partial pressure employed in this work.⁶⁵ Oxygen permeability was reduced under lower RH due to the lower oxygen diffusion coefficient relative to fully hydrated conditions.

Table 2.1. Oxygen mass transport parameters for the Pt | Nafion 117 interface obtained from data plotted in Figure 2.7, Figure 2.8, and Figure 2.9

| | $D_b \times 10^6 \text{ (cm}^2\text{/s)}$ | $c_b \times 10^6 \text{ (mol/cm}^3\text{)}$ | $D_b * c_b \times 10^{12} \text{ (mol/cm}^2\text{s)}$ |
|--------------------------|---|---|---|
| 100% RH ^a | 5.24 | 6.36 | 33.4 |
| Steady state | 1.41 (± 0.02) | 2.27 (± 0.003) | 3.21 (± 0.04) |
| 2 Minutes ^b | 1.4 (± 0.1) | 2.24 (± 0.09) | 3.12 (± 0.3) |
| 30 Minutes ^b | 1.20 (± 0.002) | 2.38 (± 0.04) | 2.86 (± 0.04) |
| 360 Minutes ^b | 0.73 (± 0.09) | 2.59 (± 0.2) | 1.90 (± 0.1) |

^a Obtained at 2.0 atm O₂, 100% RH, 323 K.⁶⁵

^b Initial value taken after holding at open circuit potential for specified duration.

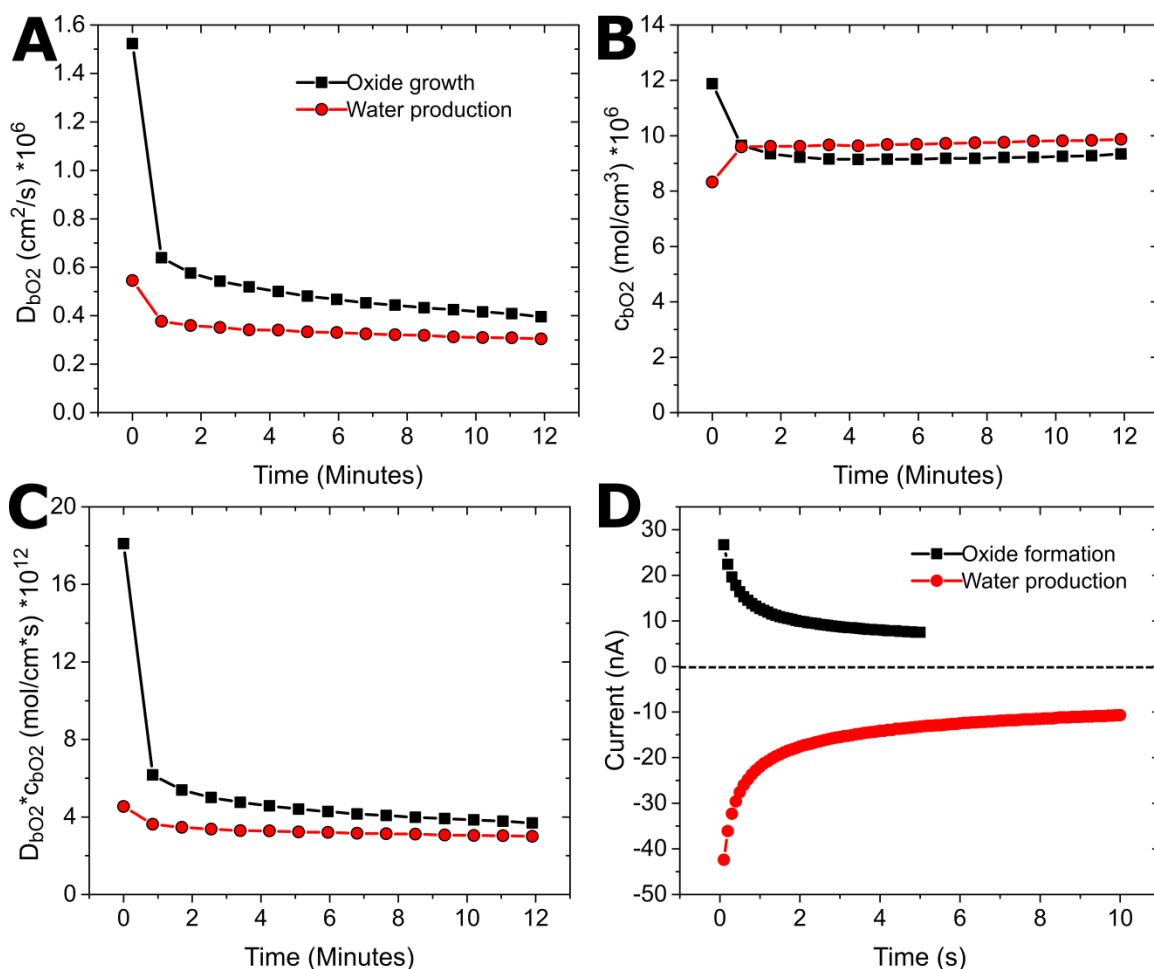


Figure 2.10. (A) Oxygen diffusion coefficient, (B) solubility, and (C) permeability resulting from forced oxide growth (1.2 V for 5s, black symbols in D), and forced water production (0.4 V for 10s, red symbols in D) in Nafion 117 at 60 °C and 60% RH.

As can be seen in Figure 2.6, the open circuit potential of around +0.96 V is within the platinum oxide formation region. In order to probe whether oxide formation over time may be responsible for the depression in diffusion coefficient and permeability, the electrochemical cell was held at open circuit potentials for 10 minutes followed by a platinum oxide growth step achieved by applying 1.2 V for 5 seconds. Afterward, chronoamperometric potential steps as described above were performed. As a comparison, the same 10 minute open circuit potential was applied followed by 10 seconds of water production at +0.4 V. The results, shown in Figure 2.10, indicate that oxide growth corresponds with higher initial mass transport parameters, potentially due to the presence of an oxide layer already on the surface which is reduced over subsequent measurements. As well, Nouri-Khorasani *et al.* showed that the local proton density at the platinum oxide surface increased drastically compared to oxide-free platinum, which can affect the rate of oxygen reduction.⁷⁹ By comparison, during water generation only the diffusion coefficient and permeability increase slightly initially, likely due to the swelling of hydrophilic channels at the interface, while the solubility is initially smaller since there is less of the hydrophobic domain in contact with the platinum surface.

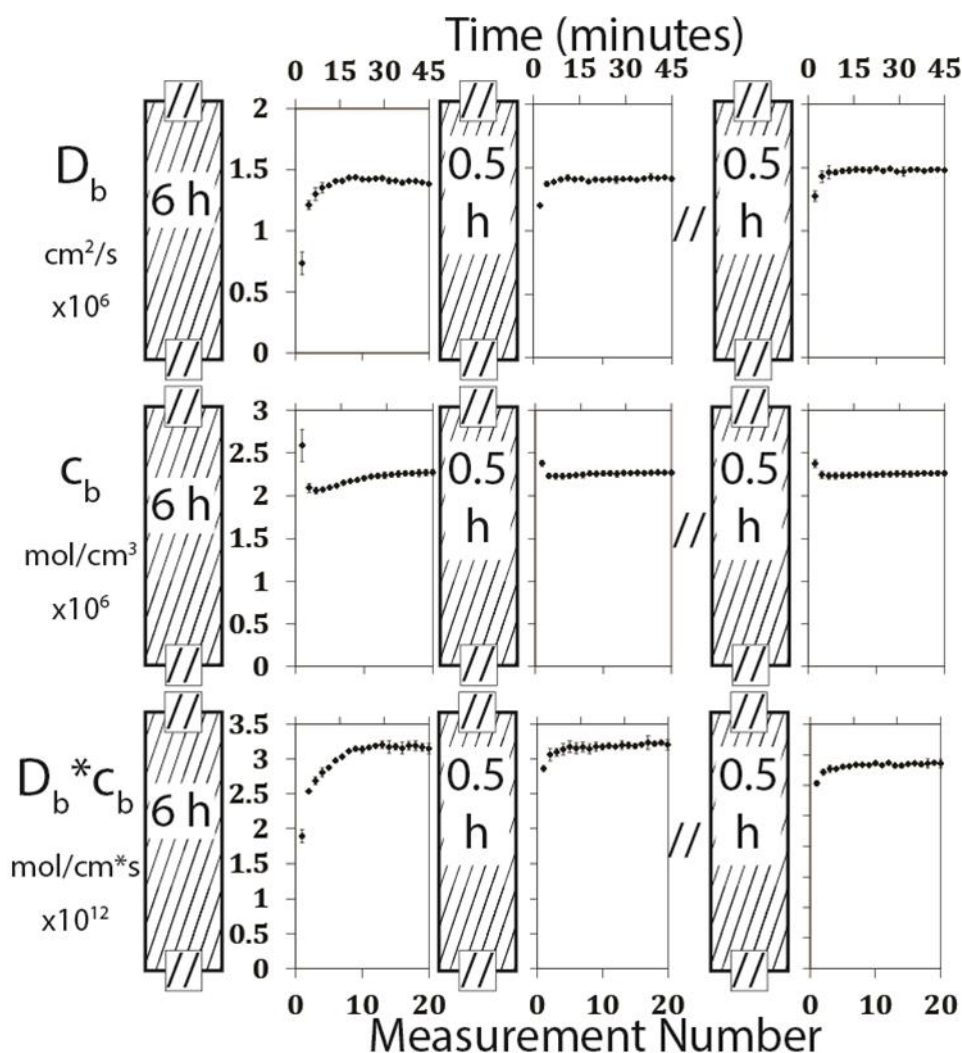


Figure 2.11. Oxygen mass transport parameters averaged over two batches, where error bars represent the standard deviation. First set of 20 measurements result from 6 hours open circuit potential, second and third columns represent 30 minutes open circuit potential.

The time/measurement-number dependency (condensed data with time included in the upper x-axis shown in Figure 2.11, for clarity on time-dependence) observed for ORR mass transport parameters may be explained by water that is electrochemically-generated at the electrode interface during each potential step measurement and the response of the membrane to the water produced. In support of this assertion, the current-sensing atomic force microscopy (AFM) studies of Hiesgen et al. is considered, in which it is suggested that pores at the membrane's surface open as a result of electrogenerated water being formed leading to better interfacial connectivity to the internal network of hydrophilic channels.¹¹¹ More specifically, when a bias potential is applied to the AFM electrode/membrane interface causing ORR, internal membrane pressures developed which were released by hydrophilic water channels opening at the surface, resulting in increased current flow.

Other investigations with AFM have shown a fluorous, hydrophobic surface present for dry PFSA, where strong phase separation was present with humidification.^{112,113} The phase separation at the surface was observed as 25 to 45 nm clusters of conductive hydrophilic sites comprised of domains 3 to 15 nm in size which are surrounded by PTFE rich regions which were non-conductive.^{114–116} The active areas increase in size and become more conductive and connected with increasing relative humidity^{115–118}, even more so in liquid water.¹¹⁹ A similar effect was postulated by Kreuer in conclusion of dynamic mechanical analyses (DMA) of membranes exposed to varying relative humidity, i.e., internal pressures in PFSA membranes resulting from increasing hydration levels are relieved by a reorganization of the morphology of the outer skin when in contact with liquid water.¹²⁰ The thermal and mechanical history of membranes was found important by Kusoglu et al., as boiling PFSA membrane in water reduced the Young's modulus compared to as-received membrane, which increased water uptake due to lower backbone rigidity.⁹⁵ Current-sensing AFM measurements performed by He and coworkers discovered a nonlinear increase in the fraction of ionically conductive area with increasing relative humidity for PFSA membranes, suggesting that RH affects the availability and accessibility of hydrophilic surface domains, which in turn influences water transport at the membrane/vapour interface.¹²¹

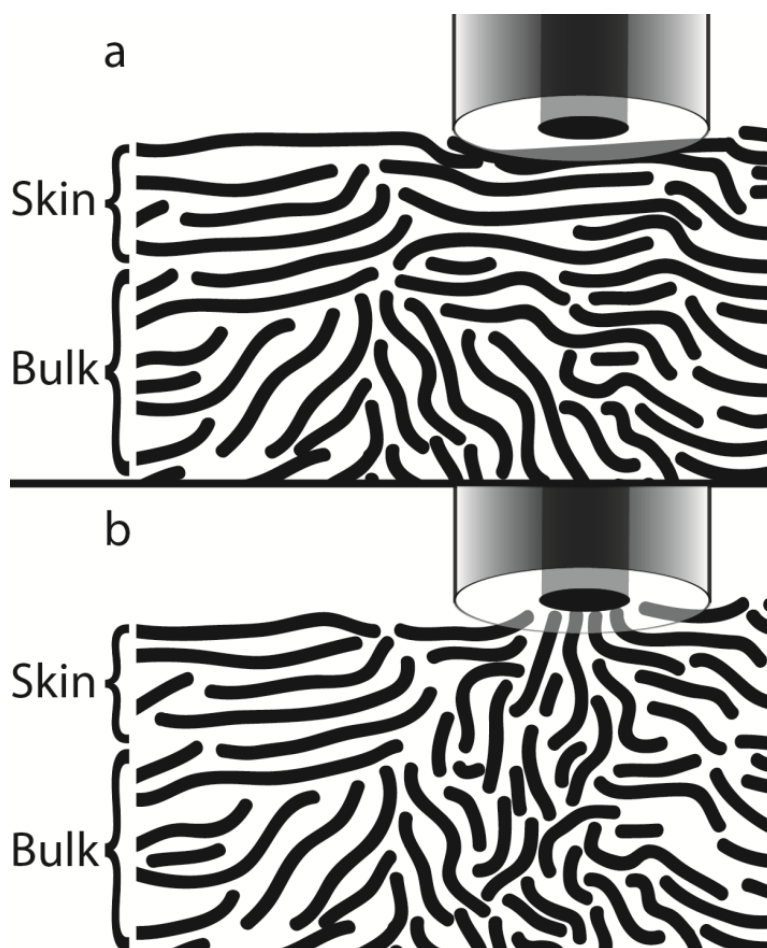


Figure 2.12. Illustration of the Pt | Nafion 117 interface (not to scale): (a) Equilibrated at 70% RH; (b) Following electrochemical-generation of liquid water that results in a morphological surface reconstruction in the vicinity of the electrode.

The time/measurement-dependence of the ORR mass transport parameters reported herein are thus explained by considering the electrode/ionomer interface to be initially equilibrated at a hydration level determined by the ambient 70% RH air but which changes upon electrogeneration of water so as to improve mass transport of reactant gas to the catalyst site, as shown pictorially in Figure 2.12. However, the chronoamperometric analyses was monitored over 1.4 s, representing an oxygen diffusion length of 20 μm , which suggests the change in mass transport parameters cannot completely be explained by a surface reconstruction. A more likely explanation is that surface reconstruction enables electrogenerated water to percolate into the hydrophilic channels within the membrane, resulting in an increase in available hydrophilic surface domains for the working electrode to probe into the bulk, which acts as a temporary increase in local environment hydration as shown by current sensing AFM.¹²¹ The induced surface hydration reveals an increase in the bulk oxygen diffusion coefficient, which suggests a collaborative effect between the surface skin and bulk membrane, as previous studies infer.⁵⁵ This effect is shown to reach a steady state, which is sustainable as long as

water is generated within 2 minutes of rest time at OCP. If the electrode is at rest for longer periods wherein water is not generated, the oxygen mass transport parameters reduce in value, indicating re-equilibration of the interface, with the effect being exacerbated with prolongation of the interval time, i.e., 6 hours at 70% RH.

Locally, ORR kinetics may be affected by interfacial water generation. Chlistunoff has suggested that product water formed during chronoamperometric measurements is expected to increase n ($n=4$ for ORR) by reducing the quantity of hydrogen peroxide produced during ORR.¹²² Improved accessibility to the water rich hydrophilic domains after liquid water penetrates the hydrophobic skin may lead to an increase in n at the electrochemical interface. In a similar fashion, local changes in ionomer surface structure and the effect on available interfacial oxygen concentration may affect ORR kinetics. Adsorbed oxygen species surface coverage on Pt may fluctuate; where a drop in kinetic current has been observed for decreased oxygen concentration as activation energies for adsorption increase as oxygen concentration decreases.¹²³

2.3.2. Time/measurement-dependence of mass transport parameters in Nafion 211 and DE2020

Due to the time dependencies observed for Nafion 117, a similar experiment was designed to see if such a difference in mass transport parameters would be seen with cast membranes as the relative humidity was lowered. Figure 2.13 shows the resulting mass transport parameters for Nafion 211 and cast DE2020 ionomer, averaged from 3 sets of data analyzed with linear regression analysis, where the working electrode was held at open circuit for 10 minutes followed by 5 back-to-back chronoamperometric measurements. With different values of RH, D_{bO_2} remains relatively constant, and there is little variation from measurement sets over all values of RH investigated. There is both an increase observed for c_{bO_2} with time/measurement number at, and below, 70% RH, as well as a larger time dependency as the RH is lowered. This suggests that for RH <70% (at 70°C) there is reduced accessibility of oxygen at the electrochemical interface until ORR has occurred, whereupon the ionomer interface undergoes a change that results in an increase in available oxygen.

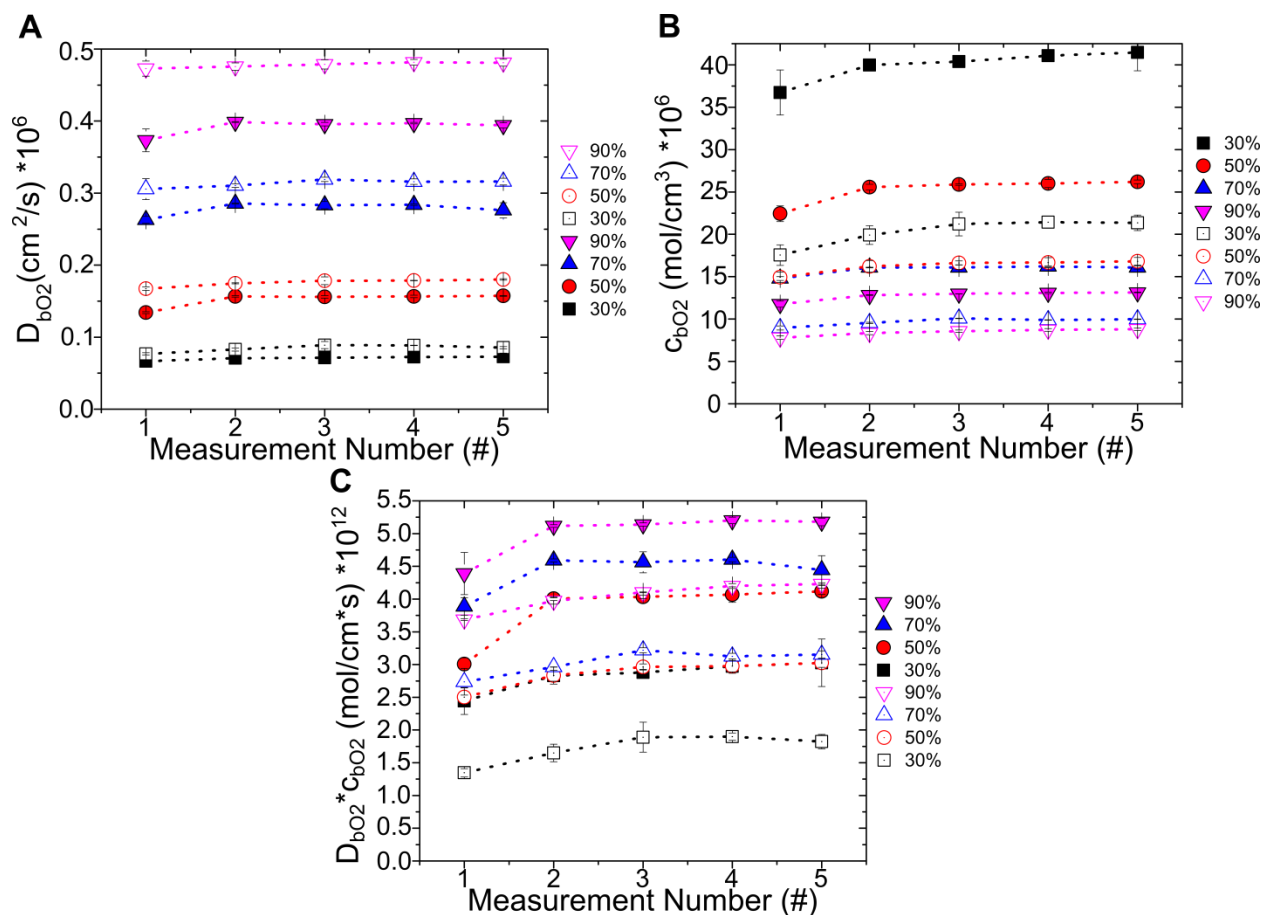


Figure 2.13. (A) D_{bO_2} , (B) c_{bO_2} , and (C) $D_{bO_2} * c_{bO_2}$ with repeated measurements for Nafion 211 membrane (open symbols) and cast DE2020 ionomer (filled symbols) from 90-30% RH at 70°C in air obtained with linear regression analysis.

It is worth commenting on the relatively consistent data acquisition for the Nafion 211 oxygen diffusion coefficient considering how the mode of diffusion in PFSA is predominantly in the water rich domains. It is possible to speculate the nature of this behaviour based off of time-based small-angle X-ray scattering measurements which revealed sub-second interfacial restructuring for a PFSA membrane in contact with liquid water.⁹⁴ If the short time domain for linear O_2 diffusion is too long compared to the surface restructuring event for cast membranes, it is possible that the initial generation of interfacial liquid water and the subsequent interfacial restructuring occurs fast enough as to reach a steady-state for diffusion in the time frame before the chronoamperometric analytical technique can detect a change in cast films, compared to extruded Nafion 117 membranes.

2.4. Conclusions

Oxygen mass transport parameters were determined for Nafion 117 at 50°C and 70% RH where time-dependent behaviour was observed. It is postulated that the generation of liquid water at the electrochemical interface leads to a morphological change at the polymer surface which increases the oxygen diffusion coefficient and permeability. The effect is reversible, with the diffusion coefficient decreasing to initial, lower values when electrochemical generation of water is stopped, and is attributed to hydrophilic channels inverting inwards as available liquid water at the surface decreases.

Analysis of repeated chronoamperometric measurements after an interfacial rest time of 10 minutes at open circuit potential for Nafion 211 and DE2020 films has revealed markedly differing behaviours from the Nafion 117 study. Notably, for both Nafion 211 and cast DE2020 there is little to no difference in the calculated oxygen diffusion coefficient, while a time dependency exists and becomes more pronounced as RH is reduced for calculated oxygen solubilities. The rate of morphological change resulting from the electrochemical generation of water may be too rapid in cast ionomer films for the present technique to measure in terms of mass transport parameters.

Chapter 3. Determination of O₂ mass transport at the Pt | PFSA ionomer interface under reduced relative humidity

This chapter is reproduced from: David Novitski and Steven Holdcroft, *ACS Applied Materials and Interfaces*, **2015**, Vol. 7 (49) 27314-2723 with permission from The American Chemical Society.

3.1. Introduction

In this chapter, the use of *ex-situ*, solid state electrochemistry provides a means to probe the oxygen diffusion coefficient (D_{bO_2}), oxygen concentration (c_{bO_2}), and permeability ($D_{bO_2} \cdot c_{bO_2}$) under conditions that mimic fuel cell operation, i.e., at the catalyst/ionomer interface during water-generating ORR. Previous studies have determined mass transport parameters for ORR using a 3-electrode Pt microelectrode-based cell, employing a dynamic hydrogen reference electrode (DHE), to be described in detail in section 3.2.4, under fully hydrated conditions, where O₂ pressure, temperature, membrane-type and IEC have been varied.^{62–66,122,124} Similar measurements under reduced RH are problematic due to the higher resistances in the membrane commensurate with low water uptake and proton conductivity, as was shown in Figure 1.7 by Peron *et al.*, and the instability of the DHE which requires liquid water for operation. The present study reports a 2-electrode approach that circumvents the use of a DHE, and allows mass transport measurements to be made at RH values as low as 30% RH, at 70°C in air. Herein, D_{bO_2} , c_{bO_2} , and $D_{bO_2} \cdot c_{bO_2}$ values for Nafion 211 and cast 20 wt% Nafion solution (DE2020) between 90–30% RH at 70°C are presented by the analysis of current transients using the Cottrell equation (short times), as in Chapter 2, as well as the Shoup-Szabo equation (all times), described below. Data are discussed in the context of water content, membrane preparation, and choice of analytical treatment.

3.2. Experimental

3.2.1. Materials

Nafion 211 (Sigma Aldrich) samples were cut to 2 cm² pieces, washed in 3 wt% H₂O₂ at 70°C to remove trace organic contaminants that may be present in the membrane, then washed with 0.5 M H₂SO₄ at 70°C to remove any trace inorganic contaminants and to ensure protonation, and thoroughly washed with MilliQ water at 70°C to remove residuals. The washing steps were necessary as impurities and contaminants present in the membrane will be seen in cyclic voltammetry. Samples were allowed to equilibrate in fresh MilliQ water at 70°C for several hours before being mounted in the electrochemical cell. DE2020 (Ion Power) 20 wt% PFSA dispersion was used as-received by drop casting directly onto the working electrode and evaporating the solvent in ambient air to a thickness of ~30 µm.

3.2.2. The reference electrode

The conventional three electrode electrochemical system is designed so that the potential of the working electrode can be known. As current is passed through the working and counter electrodes, a third electrode known as the reference electrode is used, where practically no current flows. The polarizing current flows through one circuit (the working and counter electrodes), while the change in potential at the working electrode is measured by a different circuit (the working and reference electrodes). Since no current flows through the reference electrode its potential is considered constant (a non-polarizable electrode), irrespective of the current flowing between the working and counter electrodes. This means that changes in the potential of the working electrode can be known versus the reference electrode.¹²⁵

At the same time, it is possible to use a two electrode electrochemical cell to the same effect, provided several conditions are present. The counter electrode needs to be highly reversible and not change over time in the solution of interest. The counter electrode in this arrangement is known as a pseudo-reference electrode. If the pseudo-reference is sufficiently larger than the working electrode, the resulting current density at the pseudo-reference can result in a negligible change in potential of the pseudo-reference compared to the working electrode. The use of a microelectrode as working electrode, with dimensions on the order of several microns, allows the use of large surface area metal meshes as pseudo-reference electrodes. Pseudo-reference electrodes are ideal in certain situations,

such as when contamination from ions in a conventional reference electrode is a concern, or in dry conditions where standard hydrogen reference electrodes cannot be used.

3.2.3. Solid-state electrochemical cell (2-electrode system)

In this Chapter several modifications were made to the electrochemical cell compared to Chapter 2. A 2-electrode configuration was chosen as suitable for low relative humidity operation, and a comparison of methods is described below. Assembly of the 2-electrode cell configuration is shown in Figure 3.1 (A). Two compression-spring fitted, diametrically-opposed electrode holders provide ample contact pressure to the ionomer sample, either Nafion 211 membrane or DE2020 ionomer solution drop-cast on the working electrode and allowed to dry under ambient conditions. One electrode holder contains the working electrode, a 5 μm radius Pt microdisk (Basi, inc.) polished with alumina compounds (1, 0.3, and 0.05 μm , Buehler). A hollow glass tube is employed to support a 1 cm^2 platinized platinum mesh, which is pressed against the electrode/membrane assembly and acts as both counter and reference electrodes in the present investigation. The sample is held vertically to ensure no stagnant water droplets interfere with measurements. Membrane samples are secured in a holder by way of four thumb screws. A Nafion 117 backing layer is deemed necessary in order to prevent electrode punctures through thin Nafion 211 samples as well as provide structural support for cast ionomer samples. The backing layer is not sampled during measurements as the electrochemical diffusion layer during experiments is only several microns thick via $\delta = 2\sqrt{D_{\text{O}_2}t}$ where δ is the diffusion field thickness.² Any additional resistance provided by the backing layer is considered negligible in the present study on account of the microelectrode dimensions. The electrochemical cell, shown in Figure 3.1 (C), was then placed in the environmental chamber and connected to the same equipment as described in Chapter 2. Samples were allowed to equilibrate under vapour phase conditions overnight, and at least one hour after reaching the desired RH and obtaining reproducible, overlapping cyclic voltammograms (CVs) prior to commencing chronoamperometric measurements. Current transients are run through a custom MATLAB script designed to analyze batches of experiments expediently.

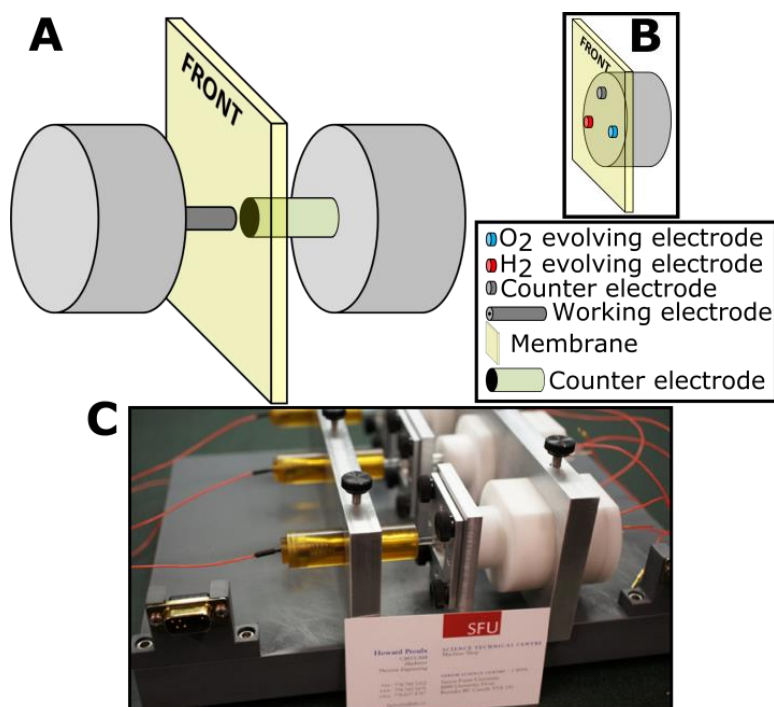


Figure 3.1. Electrochemical setup with ionomer sample pressed against a Nafion 117 backing layer. (A) Working electrode and pseudo-reference assembly are pressed against one another with compression springs to provide adequate contact pressure. (B) Comparative 3-electrode configuration. (C) Photograph of the electrochemical cell.

3.2.4. Solid-state electrochemical cell (3-electrode system)

A 3-electrode electrochemical cell was used for comparative purposes, where three isolated platinum wires were affixed in a solid plastic tube and platinized in a 1 mM solution of K_2PtCl_6 in 0.5 M H_2SO_4 at -0.2 V vs. Ag/AgCl for 2 hours. A velvety black deposit was left on the exposed ends of the wires, which were folded over the edge of the rigid tubing and pressed against the Nafion 117 backing layer. The 3-electrode configuration is shown schematically in Figure 3.1 (B). Two of the wires were connected to a 9 V battery and a series of resistors such that constant water electrolysis (Eqns. 2.10 and 2.11) occurred (~ 1.9 V at 1 M Ω), where the hydrogen evolving electrode was taken as reference. Care was taken to ensure that the oxygen evolving electrode did not interfere with measurements by placing it above the working electrode and hydrogen evolving electrode. The third platinized wire was used as counter electrode.

3.2.5. Chronoamperometric potential-step measurements versus relative humidity

As described in Chapter 2, the accurate determination of mass transport parameters D_{bO_2} and c_{bO_2} requires the application of a potential step where the ORR is under mass transport limited control. In order to ensure chronoamperometric (CA) measurements are within this regime as the relative humidity was lowered the technique of sampled-current voltammetry, SCV (described in more detail in section 3.2.6) was applied.² CA measurements were achieved by first recording cyclic voltammograms, as well as linear sweep voltammetry in the cathodic direction, to ascertain the appropriate potential range for chronoamperometry. After establishing the potential range, individual CA potential step measurements were performed after an interfacial-cleaning linear cathodic sweep at 500 mV/s was run past the ORR potential to ensure a consistent interface for all measurements. CA measurements were performed by holding an initial potential, V_i , where the redox reaction is silent, for a 10 s interval, and then to a final potential, V_f , where ORR is diffusion limited, for a period of 5 s. SCV's were obtained by adjusting the step potential (V_f) in 25 mV increments and sampling the resulting current, i_t , at a set time during the response. By plotting i_t versus step potential a current plateau is observed upon attaining mass transport limiting potentials. In this way, there is confidence that the measurement is probing the appropriate regime for ORR mass transport rather than a mixed kinetic-mass transport regime, or entering a potential regime where hydrogen evolution is observed. Obtaining an appropriate potential regime V_f was critical to ensure that an accurate and consistent electrochemical environment was applied to the membrane under varied levels of hydration.

3.2.6. Sampled current voltammetry

Sampled current voltammetry (Figure 3.2) is a chronoamperometry based technique used to determine the potential at which mass transport limiting conditions are present by performing a series of potential step experiments. Before each potential step, the initial potential is a constant value where no faradaic processes occur. The step potentials are chosen to be within three ranges: where oxygen is not yet electroactive, is electroactive but not such that the surface concentration is depleted (mixed kinetics), and where oxygen reduction is limited only by diffusion to the electrode surface. The current response increases to a limiting case as the potentials become thoroughly mass transport limiting and further potential changes do not result in an increase in current response. Sampling the current at some fixed time and plotting it versus the potential applied leads to a wave shape shown in where mass transport limiting potentials can be determined.²

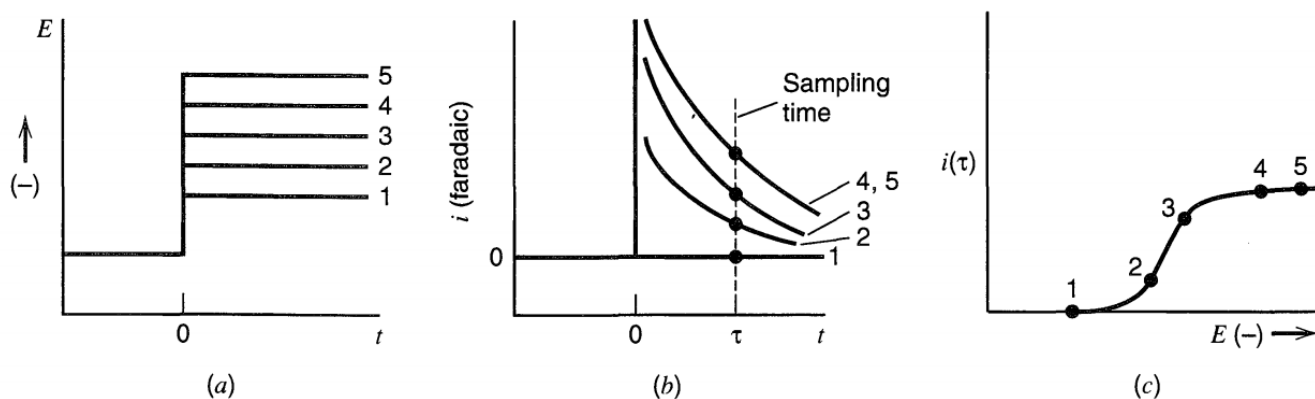


Figure 3.2. (a) Potential step square waves with increasingly negative potential steps. (b) Resulting current responses versus time where current response becomes mass transport limited at potentials 4 and 5. (c) Sampled current voltammogram showing current response versus potential, first with kinetic region slope and a diffusion limited current plateau. Reprinted with permission from reference 2. Copyright 2000 John Wiley and Sons.

3.2.7. The Shoup-Szabo equation

As a method of comparing data analysis techniques, the Cottrell equation was applied to the current transients, as described in section 2.2.3. In Chapter 3, the entire current transient (spanning short, intermediate, and long times) was also evaluated through nonlinear fitting of the Shoup-Szabo equation. Eqn. 3.1 was determined through digital simulation using an explicit hopscotch algorithm which describes the current at a microdisk electrode and remains valid for short, intermediate, and long times.¹²⁶ The Shoup-Szabo equation is powerful in that it allows the simultaneous determination of D_b and the product nc_b . At short times the current response is Cottrellian (Eqn. 2.6) and depends on $nD_b^{0.5}c_b$ while at long times the steady state current scales by $nD_b c_b$.¹²⁷ Evaluation of this approximation for the entire current transient of 5 seconds was carried out only for CA measurements that were well within the mass transport limited region and compared to linear regression (Cottrell equation) obtained parameters.

$$f(\tau) = 0.7854 + 0.8862\tau^{-\frac{1}{2}} + 0.2146\exp(-0.7823\tau^{-\frac{1}{2}}) \quad (3.1)$$

where $\tau = \frac{4D_{bO_2}t}{r^2}$ and $\frac{i}{i_{ss}} = f(\tau)$, where $i_{ss} = 4nFD_{bO_2}c_{bO_2}r$.¹²⁸ The above expression is said to be accurate to 0.6% for all times. The greatest source of error for the Shoup-Szabo equation (within the 0.6%) comes during the intermediate time regime in the current transient, when moving from linear diffusion at short times to spherical diffusion at long times. A review from Basha and Rajendran presented an approximation with a claimed even lower error for all times (0.006%).¹²⁸ Their equation,

as well as another from Mahon and Oldham, were not used over the Shoup-Szabo equation as preliminary fittings did not appreciably change the resulting mass transport coefficients, however longer computation times were necessary to fit the data.^{129,130} Nonlinear curve fitting of the Shoup-Szabo expression was achieved through *MATLAB* software where the effective working electrode radius was incorporated into the equation and compared to the geometric radius of 5 μm .

3.3. Results

3.3.1. Justification for 2-electrode (vs. 3-electrode configuration)

It was found that the conventional three-electrode cell (working, counter, reference) used in Chapter 2 did not function satisfactorily upon lowering the RH of the environmental chamber, as the DHE ceased to operate reliably. An example of the electrochemical drying behaviour can be found in overlaid CV scans in Figure 3.3. Therefore data acquisition without the use of a classical reference electrode was investigated by having the counter electrode serving as the pseudo-reference electrode. This was considered feasible because of the low current (nA) response from the working electrode compared to the large surface area of the counter electrode. It was hypothesized that the counter electrode would not be appreciably polarized when used as pseudo-reference, which would be apparent when comparing electrochemical behaviour from a 2- and 3-electrode system.

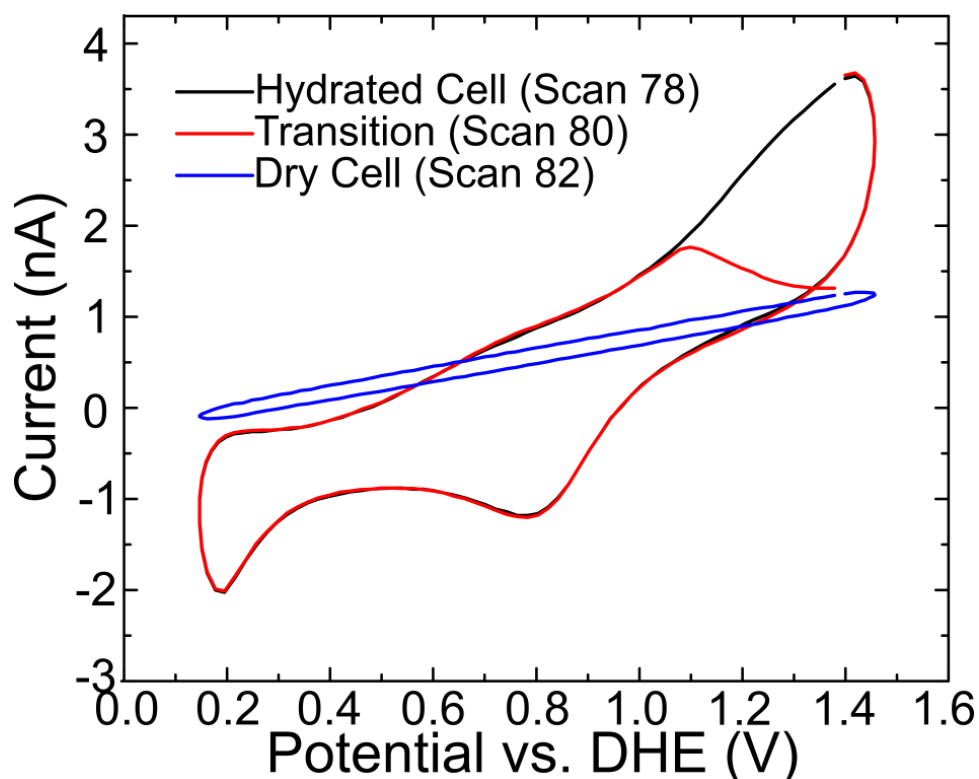


Figure 3.3. Cyclic voltammograms for Nafion 211 at 90% RH where reference electrode dries out during measurement (Temperature 70°C).

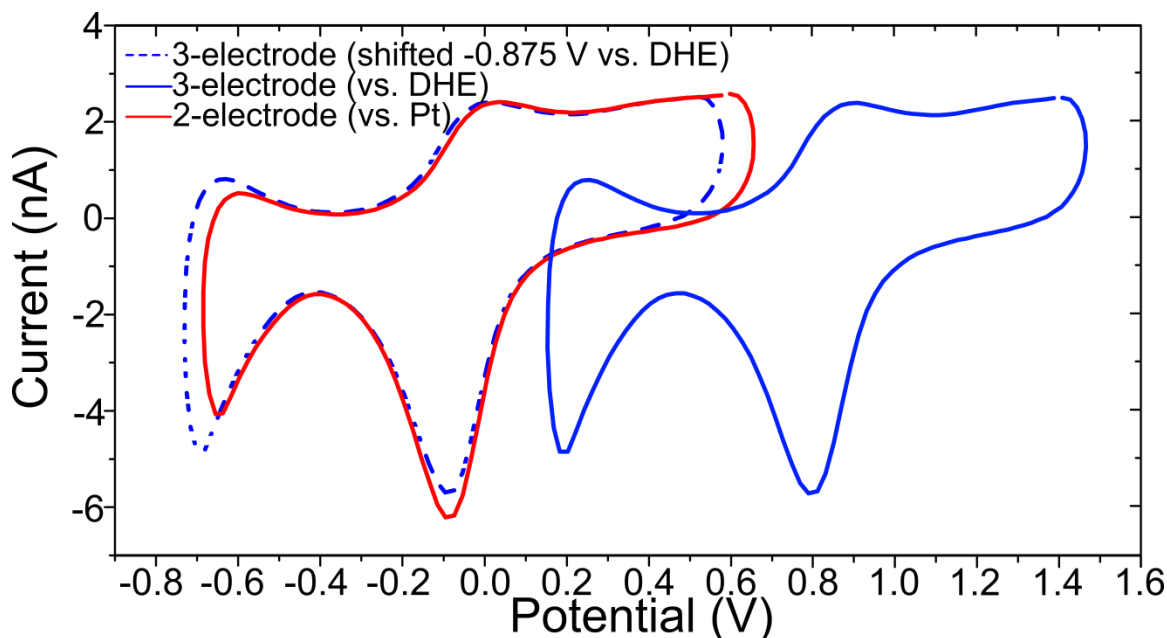


Figure 3.4. Cyclic voltammetry scans (2 V/s) for Pt/Nafion 211 at 90% RH with a dynamic hydrogen reference electrode (3-electrode) and with a platinized Pt mesh pseudo-reference (2-electrode). Potentials for 3-electrode cyclic voltammogram have been shifted (-0.875 V, dashed line) to overlap with the cyclic voltammogram of the 2-electrode configuration. Temperature: 70°C.

The effect of removing the reference electrode from the solid state electrochemical cell is observed to shift the potential of the ORR by -0.875 V vs. DHE, shown in Figure 3.4 for Pt/Nafion 211 equilibrated at 90% RH (70°C). For the cathodic portion of the sweep, platinum oxide reduction peak current exists at +0.8 V vs. DHE, where the offset cathodic current following Pt-O reduction is attributed to the ORR. H adsorption on Pt is observed from +0.4 to +0.2 V vs. DHE, where during the anodic sweep, H desorption occurs in the same potential range as adsorption, while platinum oxide formation occurs around +0.9 V vs. DHE. Overlaying the 3-electrode obtained CV scan with the 2-electrode CV sweep by -0.875 mV shows good agreement between the two systems.

Chronoamperometry was performed on Pt/ Nafion 211 in both 2- and 3-electrode cells, utilizing initial and final potential (V_i , V_f) values that are appropriate for each configuration., i.e., $V_i=+0.2$, $V_f=-0.6$ V and $V_i=+1.1$, $V_f=+0.4$ V for the 2- and 3- electrode system, respectively. The current was sampled at 100 milliseconds after applying the potential step and the potential axes of the 3-electrode data shifted by -0.875 V in order to normalize it against the 2-electrode data. The sampled-current as a function of V_f (normalized to the 2-electrode cell) is shown in Figure 3.5 The potential region more positive of -0.2 V vs. Pt, which indicates a rapidly rising current, lies in the kinetic or mixed kinetic/mass transport region of ORR. The potential region more negative of -0.5 V vs. Pt, showing the rise in sampled-current is due to the onset of H adsorption and, eventually, H₂ evolution. The plateau between -0.2 and -0.5 V vs. Pt represents a well-defined mass transport limited region. These characteristics are consistent with the physical interpretation of the features of CV's shown in Figure 3.4. Moreover, the overlap of the 2- and 3-electrode SCV's (Figure 3.4) analyzed at 100 milliseconds suggests that the use of the 2-electrode system is electrochemically acceptable.

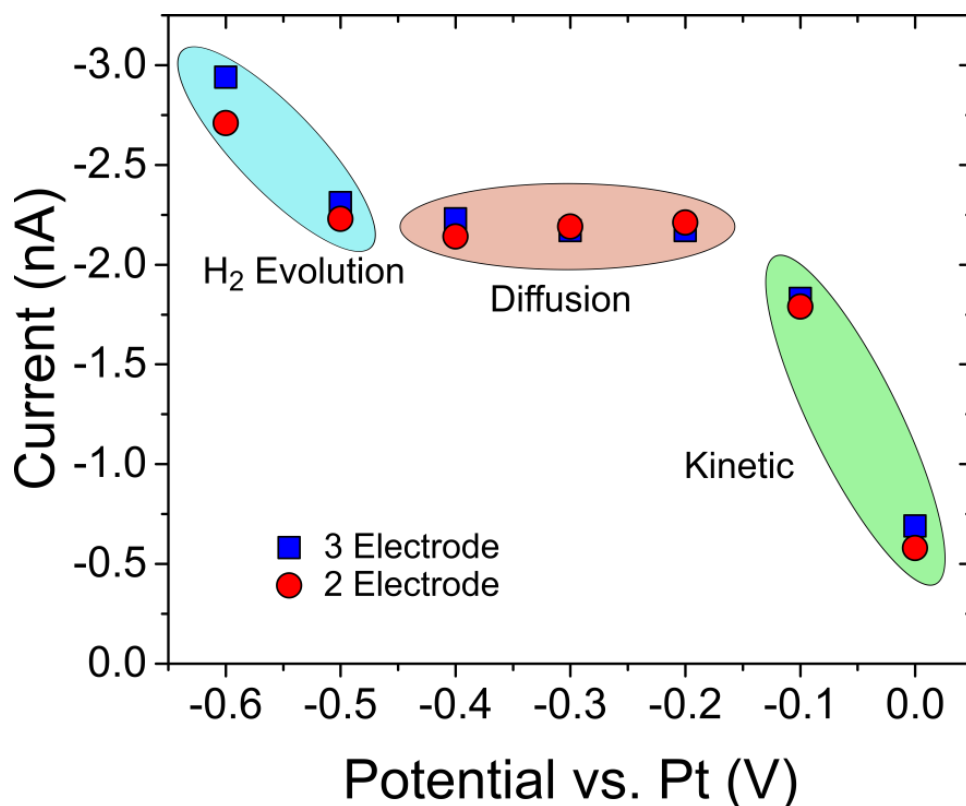


Figure 3.5. Sampled-current voltammograms for 2- and 3-electrode electrochemical cell with Nafion 211 membrane at 90% RH. Potentials have been shifted -0.875 V for 3-electrode data, overlaid current response for sample time of 100 ms after potential step. Three separate mechanisms are highlighted to indicate different processes occurring at specific potentials. Temperature: 70°C.

Further confirmation supporting the accuracy of the 2-electrode configuration was obtained by determining D_{bO_2} and c_{bO_2} values, which were obtained through potential step chronoamperometry measurements performed in the mass transport (MT) limiting region, using linear regression analysis presented in the experimental section. In this instance, the potential steps were from +0.2 to -0.3 V vs Pt for the 2-electrode system and +1.1 to +0.6 V vs DHE for the 3-electrode system. Mass transport parameters for the pseudo-reference electrode system, as well as the DHE reference electrode system, are shown in Table 3.1 to be within standard deviation. The proceeding sections therefore utilize the two-electrode pseudo-reference setup, as it will be shown that unlike the 3-electrode system, the 2-electrode system maintained the expected electrochemical activity under reduced RH. Stated potentials are reported versus Pt (-0.875 V vs. DHE) for the remainder of the presented data.

It is herein suggested that the high surface area of the platinum mesh electrode (1 cm^2) compared to the surface area of the working electrode ($7.85 \times 10^{-7} \text{ cm}^2$), combined with the small magnitude current response from electrochemical perturbation (few nA), results in an electrochemical

system where the current flowing to the pseudo-reference (Pt mesh) does not significantly polarize the electrode, and the cell does not experience any resulting potential drift during measurements.

Table 3.1 Oxygen diffusion coefficient, solubility, and permeability data for 2- and 3-electrode cells in Nafion 211 at 90% RH, 70°C, ambient air.

| | D_b (cm ² /s) $\times 10^6$ | c_b (mol/cm ³) $\times 10^6$ | $D_b \cdot c_b$ (mol/cm·s) $\times 10^{12}$ |
|-------------|--|--|---|
| 2-electrode | 0.24 \pm 0.01 | 17.1 \pm 0.3 | 4.1 \pm 0.3 |
| 3-electrode | 0.26 \pm 0.01 | 17.4 \pm 0.8 | 4.6 \pm 0.4 |

3.3.2. Electrochemically active surface area

Figure 3.6 shows typical cyclic voltammograms for Nafion 211 from 90-30% RH at 70°C in air obtained at 2 V/s. At 90% RH, the CV response is rather similar to previous works that have utilized a Pt pseudo-reference in the evaluation of PFSA membranes using Pt microelectrodes.¹³¹ When reducing the RH of the system the ORR peak is observed to shift to more negative potentials (higher overpotentials), and the peak current for the ORR decreases. As RH is reduced, the hydrogen adsorption peak shifts in a congruent manner with respect to the ORR peak, along with a decrease in the peak currents. A negative potential shift for both the Pt-oxide reduction as well as hydrogen adsorption/desorption has been reported when shifting from wet to dry gas for a Nafion/Pt(111) investigation.¹³² This was attributed to strong sulfonic acid group adsorption on the platinum surface, the magnitude of which was dependent on relative humidity, and was reversible. On the anodic sweeps, as RH increases there is a larger degree of oxide formation at potentials positive of +0.1 V. The effect of uncompensated resistance as well as double layer capacitance is investigated in both Section 2.1.1 and Appendix A, where the contributions are considered negligible in the timescale of chronoamperometric measurements.

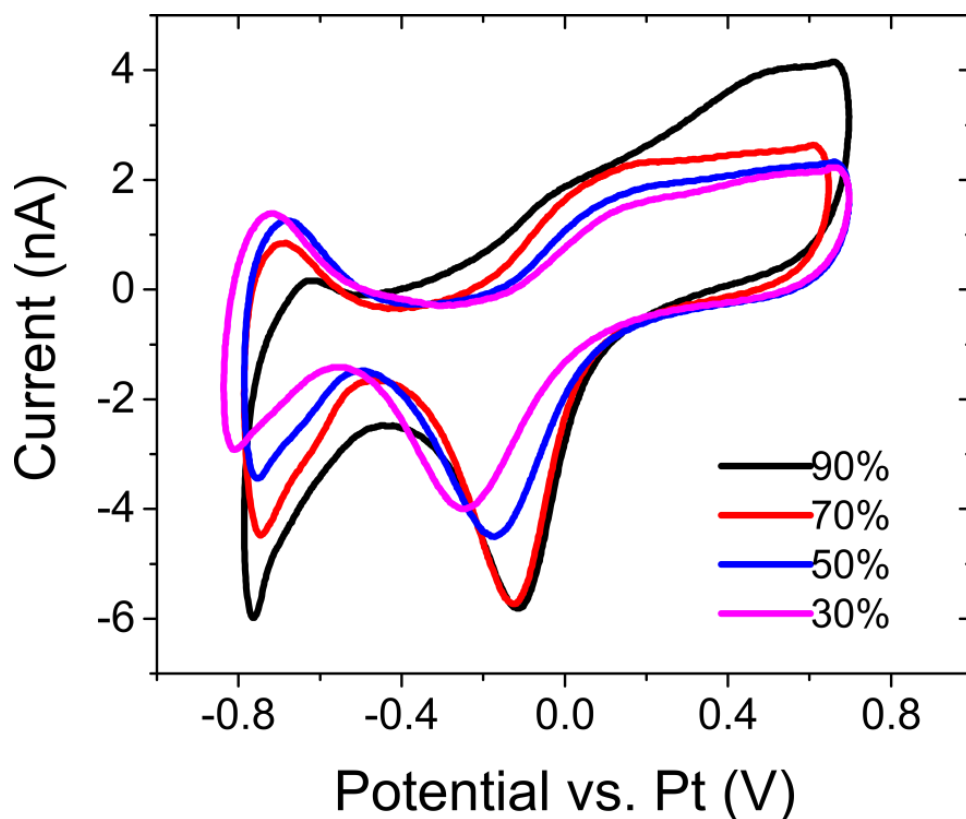


Figure 3.6. Cyclic voltammograms for Nafion 211 (2 V/s) under 90-30% RH at 70°C in air.

The electrochemically active surface area for both Nafion 211 and as-cast DE2020 ionomer solution was determined from the hydrogen adsorption charge, and is plotted in Figure 3.7. The error bars correspond to the deviation in hydrogen adsorption charge between three final sweeps in the cyclic voltammograms. As the deviation in sweeps was relatively low the error associated with cyclic voltammograms was not propagated through to the determination of mass transport parameters. The geometric area of the working electrode was $7.85 \times 10^{-7} \text{ cm}^2$, where polished polycrystalline platinum has a typical surface roughness of ~ 2 , which accounts for the larger effective calculated areas measured under high RH. The effective area is seen to decrease as relative humidity is lowered for both the membrane and cast-ionomer samples. This observation is congruent with conductive AFM studies that revealed a lower active surface area for a similar Nafion membrane, N212, as RH is reduced.¹²¹ As the degree of hydration is lowered, the Pt-exposed ionomer exhibits increasingly hydrophobic character. Considering that the conduction pathways are through hydrophilic channels, this phenomenon results in a lowered active surface area, as illustrated in the inset for Figure 3.7, where under low RH conditions there are isolated pockets of conductive hydrophilic channels at the ionomer/Pt interface. The combined area of conductive ionomer is averaged into a smaller circle than the geometric circle, where the resulting calculated radius is used in the analytical equations toward the determination of area-corrected mass transport parameters.

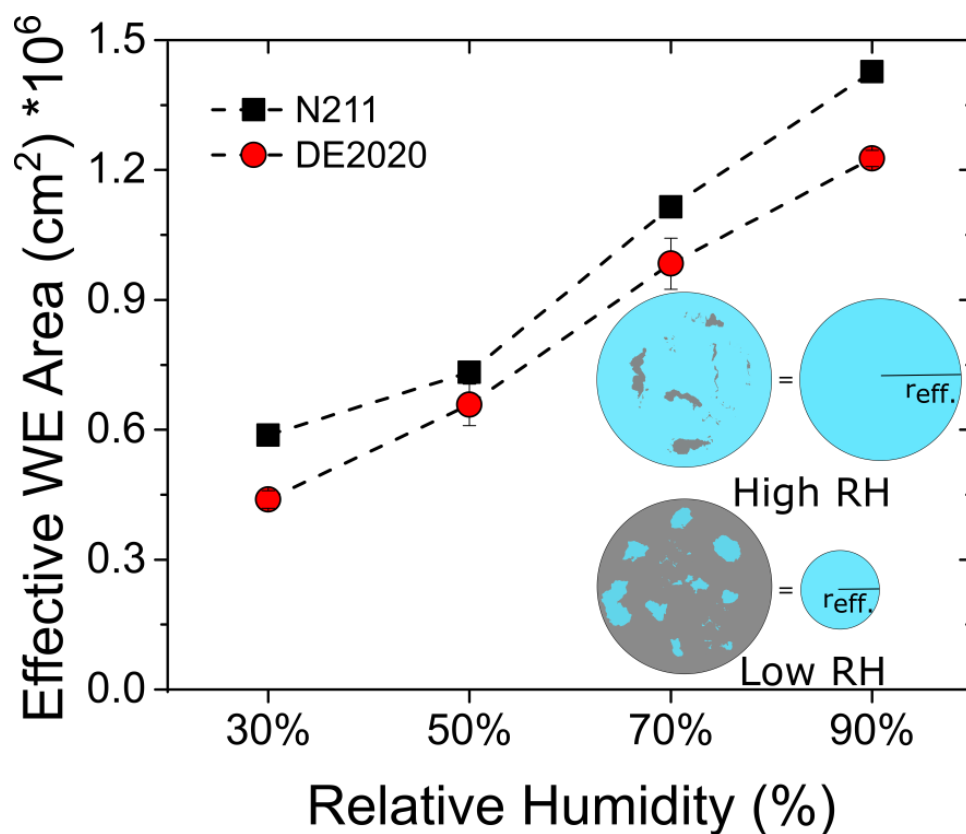


Figure 3.7. Effective working electrode area calculated from H-adsorption charge minus background capacitive current. (Inset) stylized working electrode/ionomer interface shown where blue region is water-rich conductive area and grey is Pt surface exposed to hydrophobic domains (non-active). Effective radius (r_{eff} , dramatized for effect) is derived from the electrochemically active surface area and used in mass transport calculations.

There exists an inherent uncertainty in the calculated ECSA values with regards to the impact of the hydrogen evolution region potentially overlapping with the hydrogen adsorption peak, which would result in errors during calculation. This is due to the assumption that the shift in the ORR peak is congruent with the shift in the H adsorption peak, which may overlap to a greater extent with the H_2 evolution region as RH is decreased. It has been suggested that the use of CO stripping voltammetry may be more accurate toward determining the effective surface area due to the ambiguity of the potential region where H adsorption ends, and gas evolution begins.¹³³ In the present study, the introduction of CO into the environmental chamber was not possible and thus the H adsorption method is used. A similar reduction in ECSA has been observed as RH is lowered using both CO stripping and H adsorption methods, although a discrepancy between calculated ECSA's was reported which may have arisen from the catalyst layer composition, comprised of porous void space and carbon support in addition to the platinum catalyst and ionomer.¹³⁴ The present usage of “effective area” calculated from H adsorption can be seen as a simplified model.

CV scans for cast DE2020 ionomer under controlled RH are shown in Figure 3.8. For the 90% RH CV there exists an anomalous oxidation peak at -0.35 V that has previously been attributed to an unknown oxygenated species that persists at low scan rates and low hydration conditions.¹³⁵ It is noted that the peak was observed intermittently during experiments for both Nafion 211 and as-cast DE2020 only when the RH was between 90 and 70% RH. Upon lowering the RH to 50 and 30% the anomalous peak was not observed. The nature of the peak's disappearance is unknown as it would be expected to persist and potentially increase in magnitude as hydration is lowered.

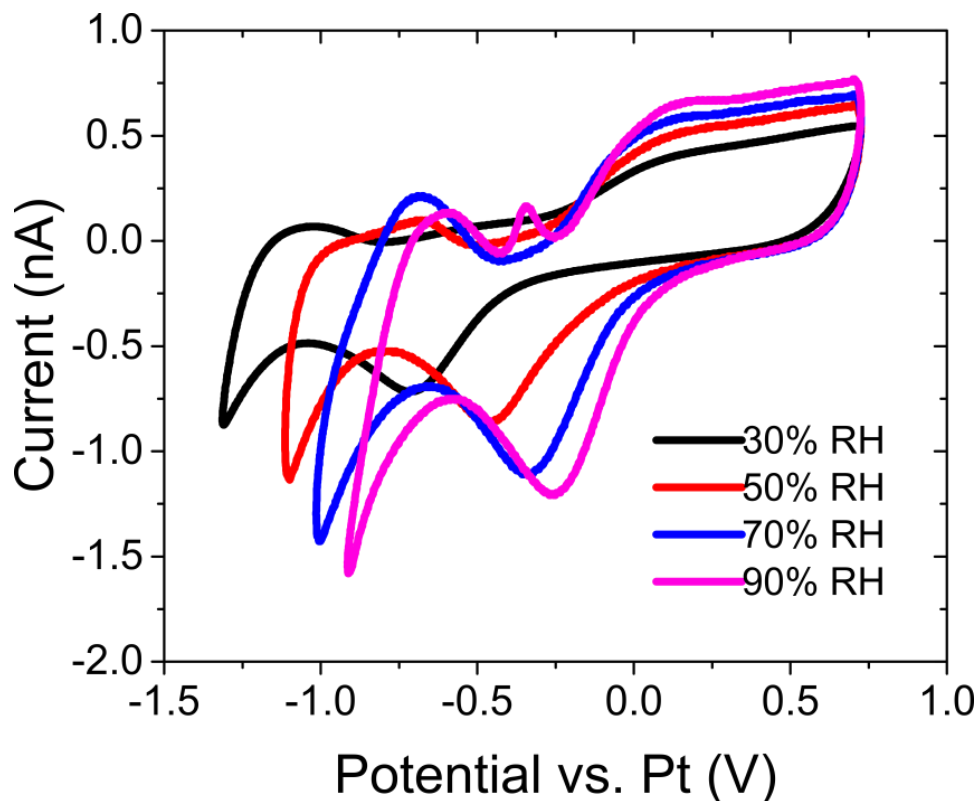


Figure 3.8. Cyclic voltammetry sweeps for cast DE2020 (1 V/s) from 90-30% RH at 70°C in air. Anomalous oxidation peak only present for 90% RH scan.

3.3.3. Oxygen reduction-limited chronoamperometry: Linear regression analysis

The electrochemical response at the Pt/PFSA interface changes as the relative humidity is lowered. The effect on the ORR is evident from the 2-electrode CV's shown in Figure 3.6. The potential of the peak current corresponding to ORR is progressively shifted to more negative potentials upon reducing the RH, while the peak current progressively decreases. The shift in peak position necessitates the aforementioned sampled-current voltammetry (SCV) analysis to determine the appropriate final applied potential, V_f , required to have confidence that CA measurements are analysed within the diffusion limited region. The initial potential region where the ORR was inactive, V_i , did not

change considerably with RH, thus a value of +0.3 V was used for the proceeding experiments. Moreover, applying V_i values higher or lower than +0.3 V resulted in either spiked SCV's due to oxide formation (that deposited on the electrode surface during the initial potential hold), or no current plateau resulting from being in the mixed kinetic regime. A clear representation of the importance of choosing V_i carefully is presented in Figure 3.9, which highlights how the current response varies if V_i is not electrochemically quiet. The resulting under- or over-represented current response had a significant effect on the resulting calculated O_2 mass transport parameters regardless of method used to analyze data.

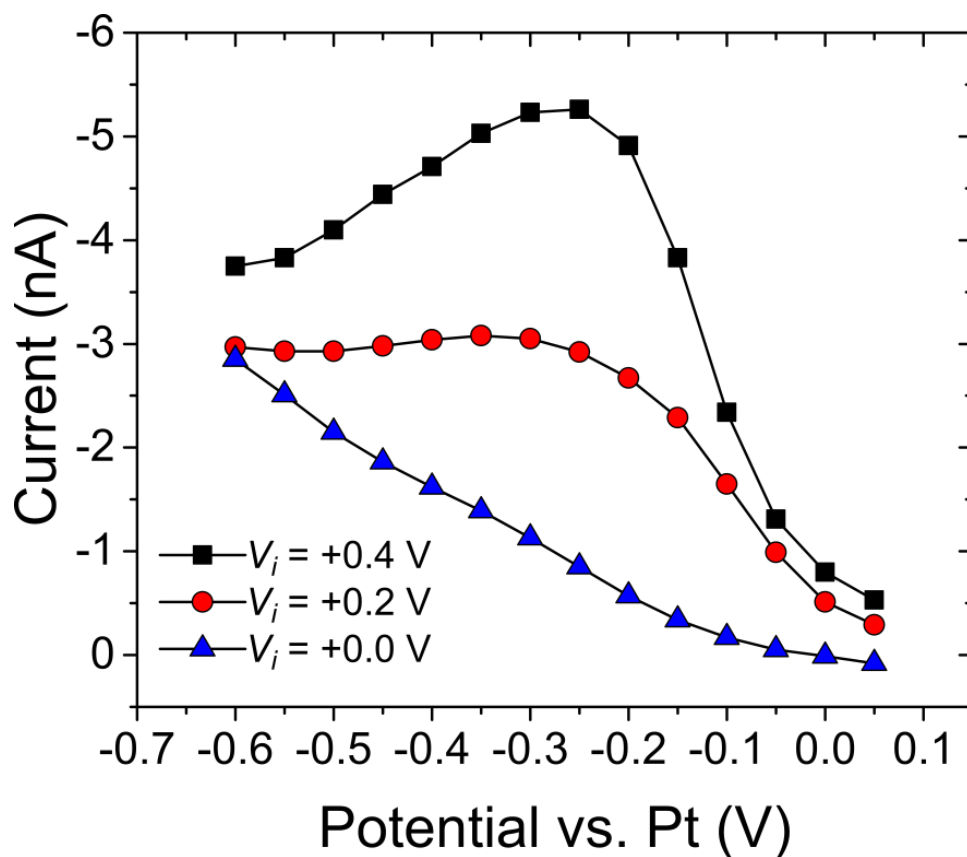


Figure 3.9. Sampled-current voltammograms obtained for Nafion 211 at 90% RH and 70°C with varied initial potential, V_i . Although the value of +0.3 V was chosen in the presented work, this particular example had a current plateau at +0.2 V. Sampled current voltammetry comparisons such as this can be used to determine optimal initial and final potentials for chronoamperometric measurements.

Once V_i is sufficiently positive so as to not be within the kinetic regime, e.g., +0.3 V, a limiting current plateau is obtained, indicating mass transport limiting conditions, as shown for 90-30% RH in Figure 3.10. In order to obtain a flat plateau for the sampled-current voltammograms the current had to be sampled at a specific time – which was observed to change with RH, with longer times required for reduced RH. The current sampling times to provide sufficient limiting current plateaus for Nafion 211

were 100, 115, 165, and 190 milliseconds from 90, 70, 50, and 30% RH. A similar shift in current sampling times was also observed for as-cast DE2020 ionomer samples. The rationale behind this occurrence is the increased resistance of the membrane as hydration is lowered.²⁵ The increased resistance prolongs the time to reach limiting current as the charging constant, R^*C , increases with decreasing RH. The current transients collected versus applied potential are shown in Figure 3.11, where the time at which a limiting plateau current is obtained can be seen, matched with the cathodic linear sweep that validates the expected potential to reach mass transport limitation.

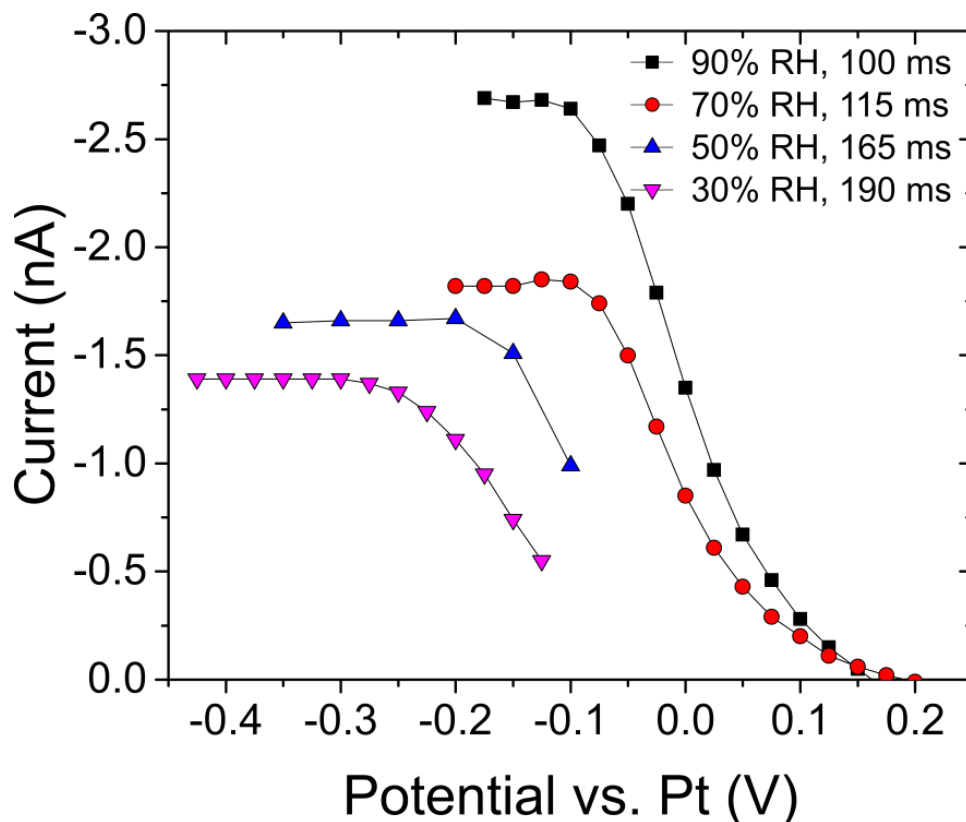


Figure 3.10. Sampled-current voltammograms for Nafion 211 from 90-30% RH (70°C). $V_i = +0.3$ V, plotted points are obtained by changing V_f for individual potential step measurements. Current sampling times are included in legend.

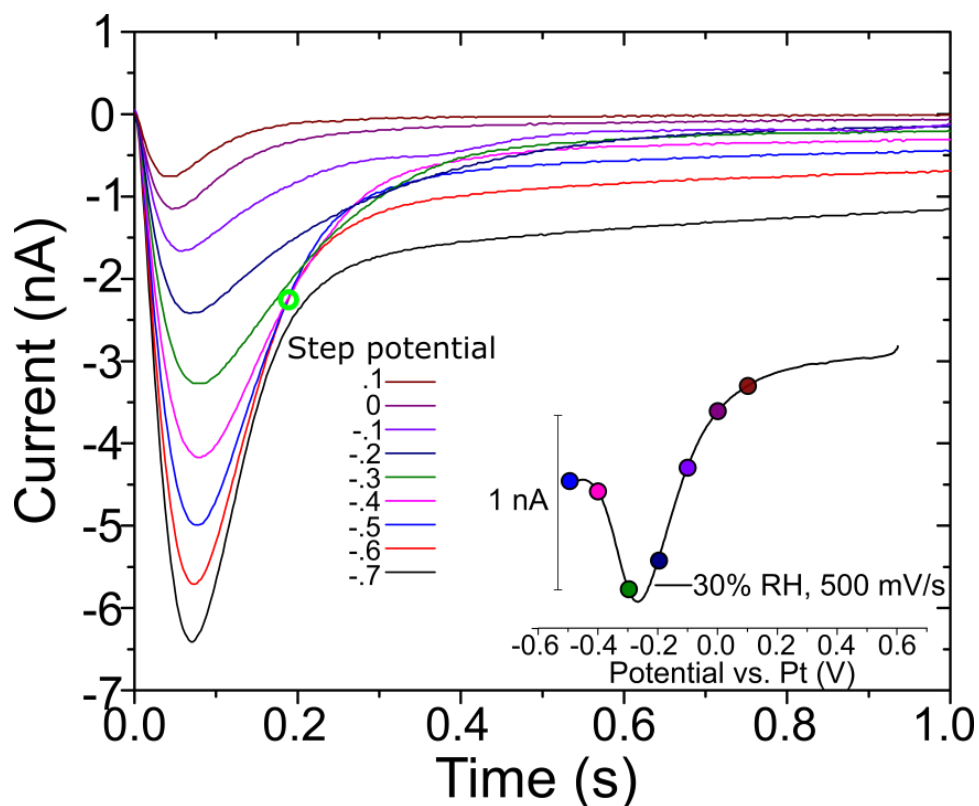


Figure 3.11. Potential step measurements for Nafion 211 at 30% RH. Small circle at 0.189 s shows mass transport limiting current in the applicable potential range. Inset: linear cathodic sweep with representative potential step indicators, mass transport begins at overpotentials past Pt-O reduction peak current.

Cottrell plots (Figure 3.12) were generated from current transients obtained in the well-defined mass transport limiting region. The linearity of the Cottrell plots was ensured by extending 5 data points before and after the times shown in Figure 3.10. The data acquisition was at a rate of 1,000 points per second, resulting in a window of 25 milliseconds for linear regression analysis. O_2 mass transport parameters were derived from the slopes and intercepts of the line, presented in Figure 3.12. Presented mass transport parameters are the average within the range of potentials which produce mass transport limiting conditions.

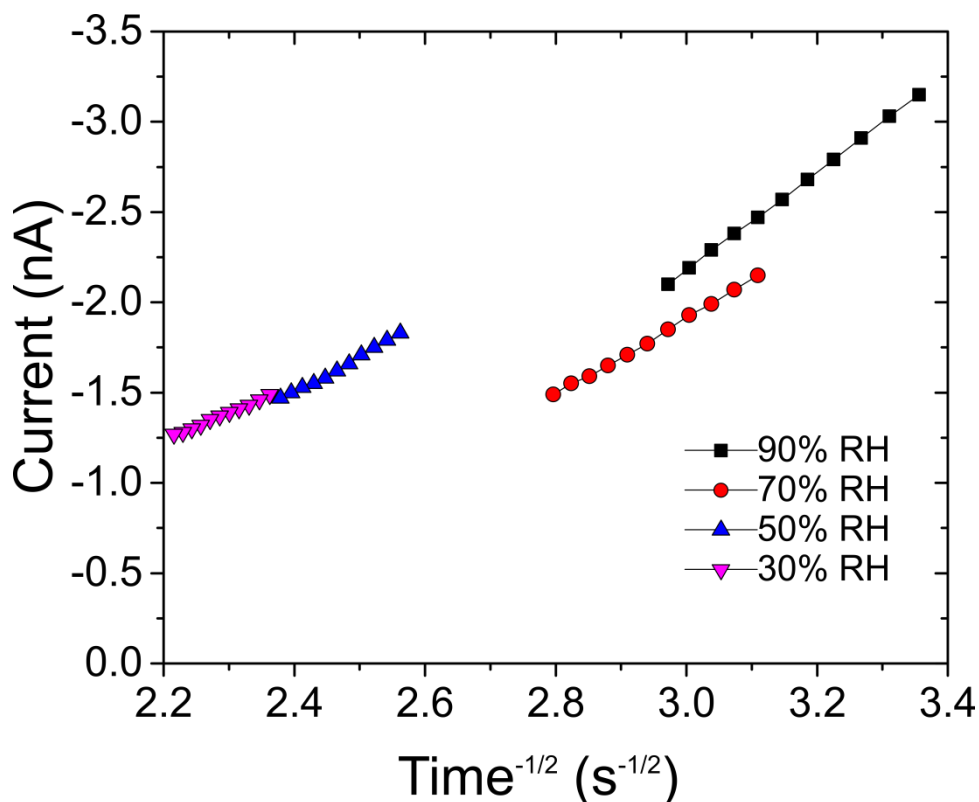


Figure 3.12. Cottrell plots for Nafion 211 at 90 to 30% RH and 70 °C.

Figure 3.13 shows calculated oxygen diffusion coefficients from linear regression analysis, with corrections for the reduced electrode area upon reducing the RH (see Figure 3.7). D_{bO_2} decreases for Nafion 211 membrane and as cast DE2020 ionomer as the relative humidity is lowered. This trend is consistent with studies which indicated that the higher the IEC, the higher the O_2 diffusion coefficients, due to there being a higher membrane water content.⁶² This is expected, as oxygen is predominantly considered to diffuse through hydrophilic domains.⁶¹ As RH is reduced the hydrophilic domains at the surface have been shown to be less accessible, leading to a higher mass transfer resistance.¹²¹ Error bars for oxygen diffusion coefficients correspond to the standard deviation of coefficients obtained for three current transients within mass transport limited potentials.

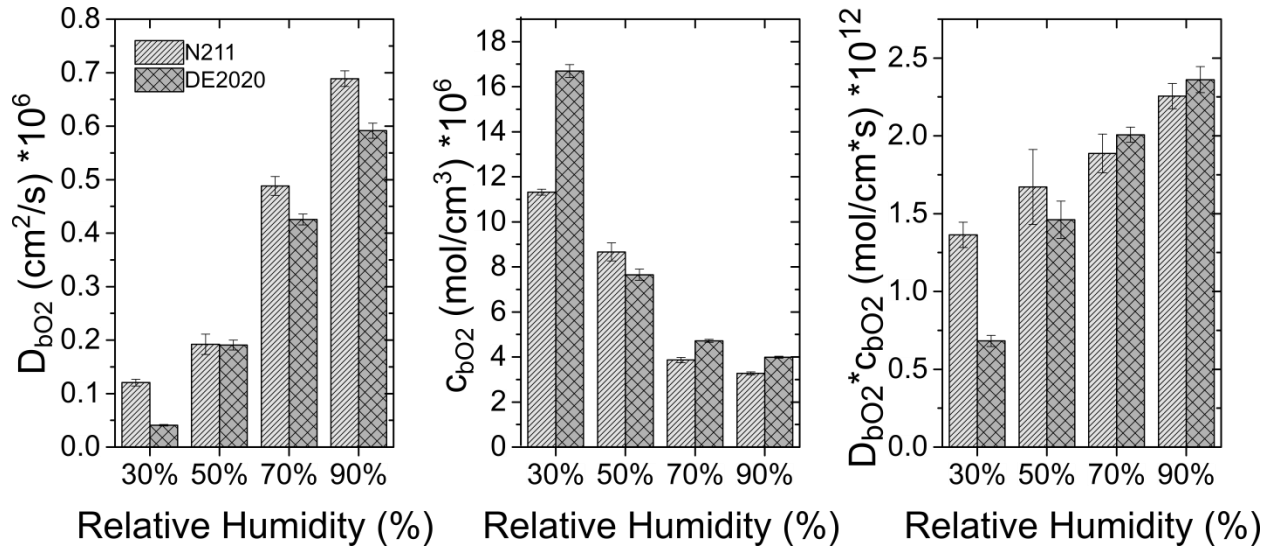


Figure 3.13. O_2 mass transport parameters calculated by linear regression versus RH for Nafion 211 membrane and cast DE2020 at 70°C in air, with effective working electrode area corrected in calculations.

Oxygen concentration (Figure 3.13) is shown to increase as the relative humidity is reduced, for both membranes and cast ionomer, when the area of the electrode is corrected for reduced RH. This behaviour is similarly expected from the previously mentioned IEC studies which showed that as IEC and water content increased oxygen concentration decreased.⁶² Oxygen is considered to dissolve predominantly in the hydrophobic domain, which increases in character as water content is decreased.⁶¹ Error bars for oxygen solubility correspond to the standard deviation of values obtained for three current transients within mass transport limited potentials.

Oxygen permeability ($D_{bo2} * C_{bo2}$) for both Nafion 211 and DE2020 decreases as relative humidity is reduced when the electrode area is corrected (Figure 3.13). This is caused by a larger decrease in the diffusion coefficients with respect to the increasing oxygen concentration. The oxygen permeability calculated by electrochemical techniques are consistent with reported trends using differential pressure methods.^{131,136} O_2 mass transport parameters obtained from area-corrected linear regression are presented in Table 3.2. Error bars for oxygen permeability correspond to the added relative uncertainties of oxygen diffusion coefficients and solubility values.

Table 3.2 Water content, oxygen diffusion coefficients, solubility, and permeability data for Nafion 211 and DE2020 at 70°C in ambient air obtained through area-corrected linear regression analysis.

| | RH (%) | Hydration number (λ) | Water Uptake ($\text{g}_{\text{H}_2\text{O}}/\text{g}_{\text{dry}}$) | $D_{bo2} \text{ (cm}^2\text{/s)} \times 10^6$ | $C_{bo2} \text{ (mol/cm}^3\text{)} \times 10^6$ | $D_{bo2} * C_{bo2} \text{ (mol/cm}^2\text{s)} \times 10^{12}$ |
|-------------------------|--------|--------------------------------|--|---|---|---|
| Nafion 211 ¹ | 30 | 2.5 | 4.5 | 0.12 ± 0.01 | 11 ± 0.1 | 1.4 ± 0.1 |
| | 50 | 3.8 | 7.5 | 0.20 ± 0.02 | 8.7 ± 0.4 | 1.7 ± 0.2 |

| | | | | | | |
|--------------------------|----|-----|------|------------------|---------------|-----------------|
| | 70 | 5.9 | 9.75 | 0.49 ± 0.02 | 3.9 ± 0.1 | 1.9 ± 0.1 |
| | 90 | 9.3 | 15 | 0.69 ± 0.01 | 3.3 ± 0.1 | 2.3 ± 0.1 |
| Cast DE2020 ² | 30 | 3.8 | | 0.04 ± 0.001 | 17 ± 0.3 | 0.70 ± 0.01 |
| | 50 | 5.5 | | 0.19 ± 0.01 | 7.7 ± 0.3 | 1.5 ± 0.1 |
| | 70 | 6.3 | | 0.43 ± 0.01 | 4.7 ± 0.1 | 2.0 ± 0.01 |
| | 90 | 9 | | 0.59 ± 0.01 | 4.0 ± 0.1 | 2.4 ± 0.01 |

1 Water content data taken from reference ²⁵.

2 Water content data taken from reference ¹³⁷.

If the effective electrochemical area of the working electrode is not accounted for in the regression analysis (Figure 3.14), it can be seen that the conclusions are orthogonal: while there still exists an overall trend of decreasing diffusion coefficient with decreasing relative humidity, the change is much smaller. The oxygen concentration values are seen to fluctuate for both samples if the electrode area is not corrected, which is not congruent with Henry's law, which states that solubility increases proportionally with increasing partial pressure, which reasserts that the electrode area must be corrected for in the analytical equation to account for the decreasing area with decreasing RH. Figure 3.15 reveals a proportional trend for the area-corrected data, where solubilities uncorrected for area do not exhibit Henry's law type behaviour, For non-area corrected analysis, the oxygen permeability decreases as relative humidity is lowered for the Nafion 211 membrane, however for the cast ionomer it increases upon lowering the RH from 90 to 70 RH%, and then decreases from 70 to 30% RH.

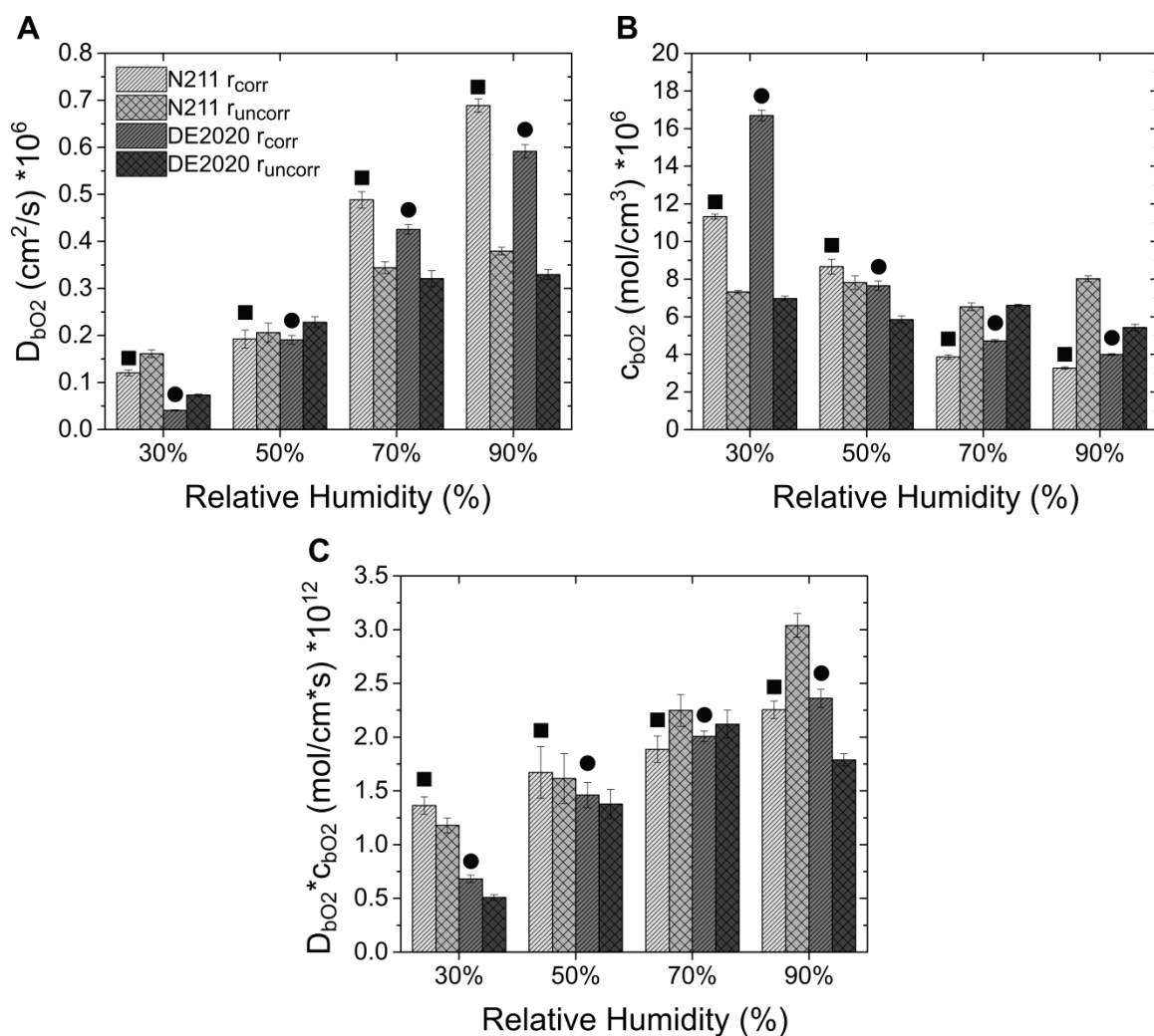


Figure 3.14. O_2 mass transport parameters calculated by linear regression analysis versus RH for Nafion 211 membrane and cast DE2020 at 70°C in air, where ■ and ● emphasize r_{corr} , respectively. (A) D_{bo2} , (B) c_{bo2} , (C) $D_{bo2}c_{bo2}$.

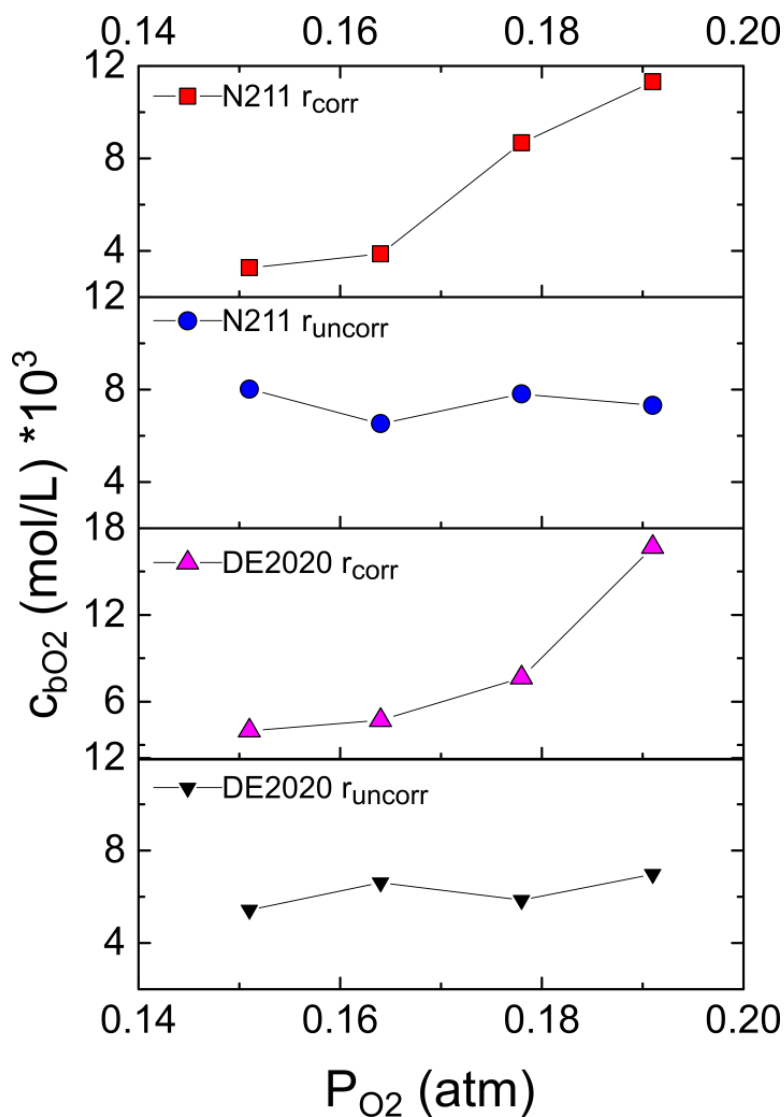


Figure 3.15. Oxygen solubilities versus oxygen partial pressure for radius corrected and uncorrected datasets. Increasing P_{O_2} corresponds with decreasing RH.

Comparison of the presented mass transport parameters with those previously reported in literature is difficult to make in part due to the general absence of experimental reports using microelectrode studies under low P_{O_2} (air) and P_{H_2O} (water vapour). Gode et al. offer the closest comparison in their cylindrical microelectrode investigation, wherein a comparison of O_2 mass transport parameters, found in Figure 3.16, shows comparable values with presented Nafion 211 radius corrected data.¹³¹

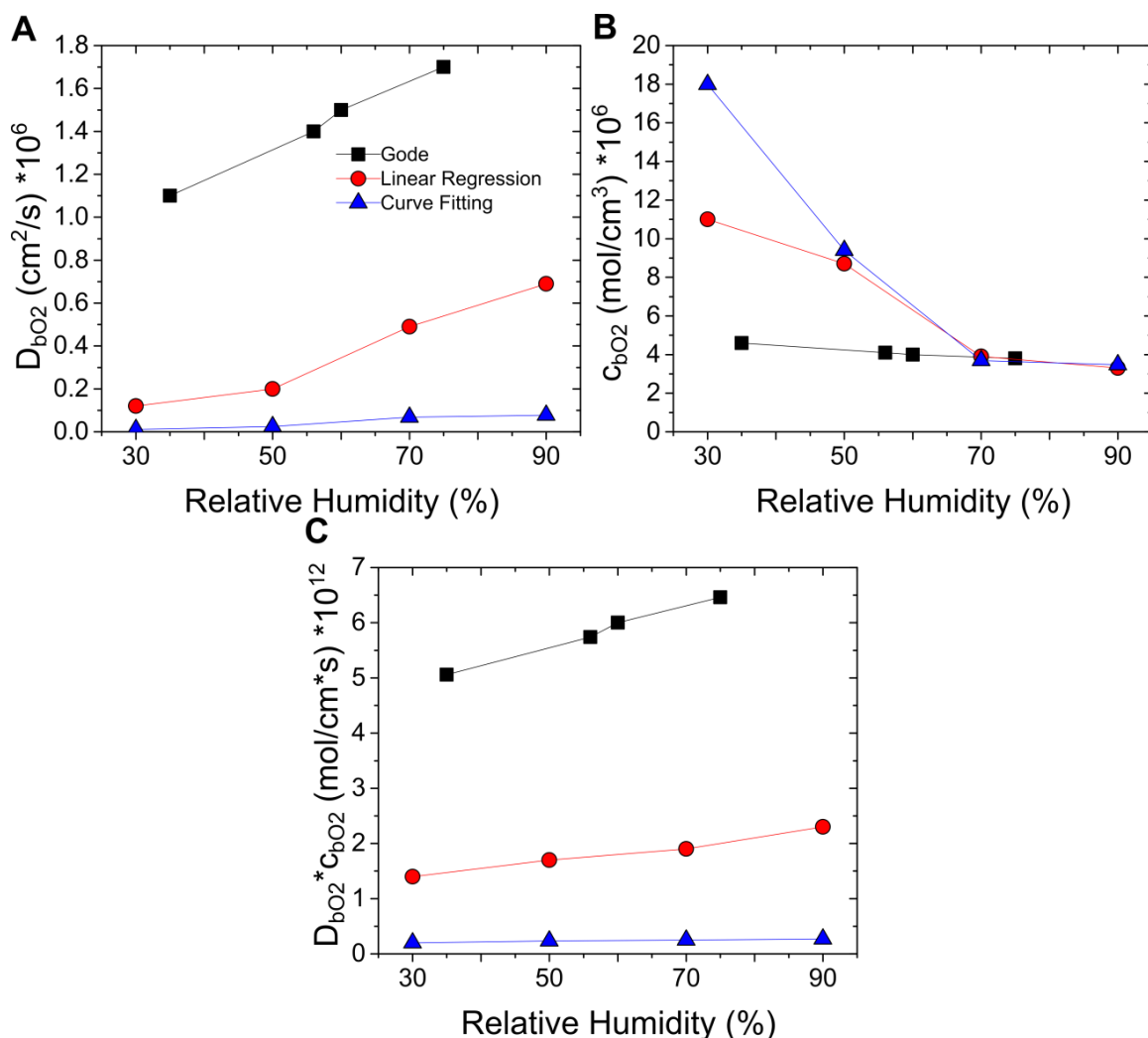


Figure 3.16. (A) D_{bo2} , (B) c_{bo2} , (C) $D_{bo2}c_{bo2}$ comparison between linear regression obtained, area corrected Nafion 211 data taken at 70°C in air (present work), non-linear curve fitting obtained, area corrected Nafion 211 data taken at 70°C in air (present work), and Pt microcylinder study with Nafion 117 data taken at 60°C and fed with O₂ gas (ref ¹³¹).

3.3.4. Oxygen reduction-limited chronoamperometry: Non-linear curve fitting analysis

The Shoup-Szabo equation was used to confirm the presence of a trend in the oxygen mass transport parameters, where non-linear curve fitting was utilized to determine the parameters for the entire current transient time of 5 seconds after perturbation. Figure 3.17 shows an area-corrected current transient fit for Nafion 211 at 90% RH with an $R^2=0.82$. Curve fits for all values of RH for both Nafion 211 and cast DE2020 had similar R^2 coefficients. The mass transport parameters obtained through non-linear curve fitting methods are compiled in Figure 3.18, where, when correcting for electrode area with RH, D_{bo2} decreases as relative humidity is reduced for both Nafion 211 and cast

ionomer. The magnitude of change versus RH is similar to the trend observed using linear regression analysis, while the mass transport parameters themselves are an order of magnitude lower than those calculated by linear regression.

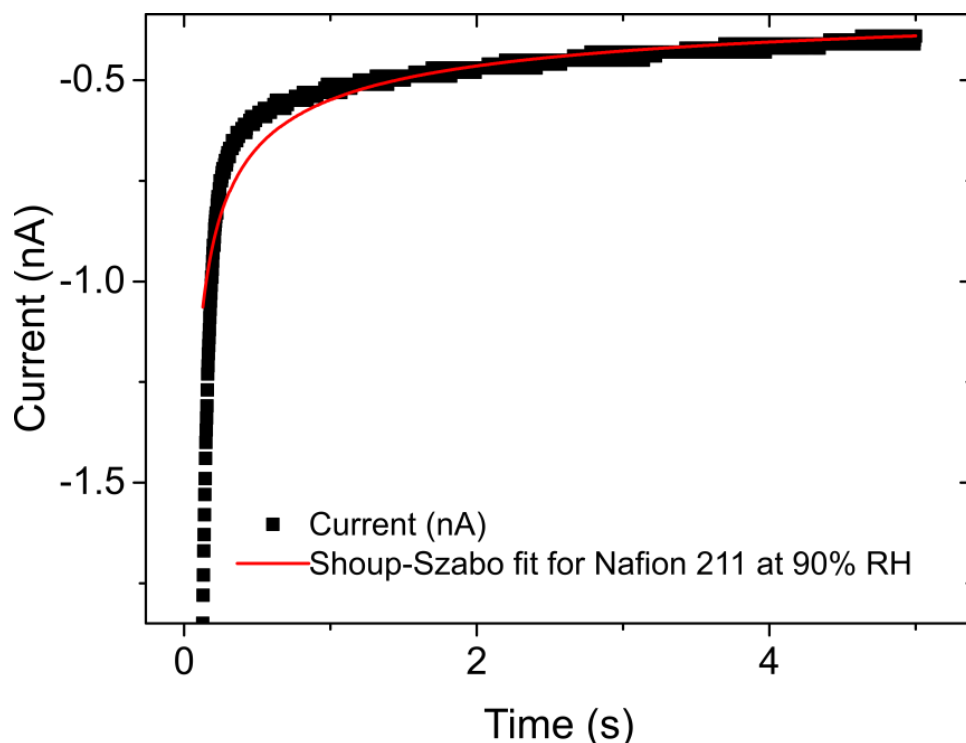


Figure 3.17. Non-linear curve fit for current transient obtained for Nafion 211 at 90% RH and 70°C.

The oxygen concentration values (Figure 3.18) are shown to increase as relative humidity decreases for both membrane and cast ionomer, for the area-corrected fittings. The calculated values match well with those obtained using linear regression analysis in both trend and magnitude. Comparing mass transport parameters with reported literature values that were obtained under lower temperature and under oxygen gas may help to explain the discrepancy (Figure 3.16). Considering previous electrochemical studies that indicated higher oxygen pressures yield larger D_{bO_2} and c_{bO_2} values, the non-linear curve fitting analysis presented herein seems reasonable.⁶⁵ Similarly, there is uncertainty in the true diffusion field thickness in the short time domain used in the linear regression analysis when accounting for the charging current that has been suggested to increase with reduced RH. With an estimated maximum 2 μm penetration depth for the linear regression analysis data, it may be, in reality, much smaller, when accounting for the tortuosity of the membrane or cast ionomer, and reduced connectedness of hydrophilic channels at reduced RH. If the true diffusion field thickness only probes the predominantly hydrophobic surface skin, one might expect to see higher values of oxygen concentration with lower oxygen diffusion coefficients. While higher values of oxygen concentration are

observed, there are also higher values for the oxygen diffusion coefficients with linear regression analysis compared to non-linear curve fitted data.

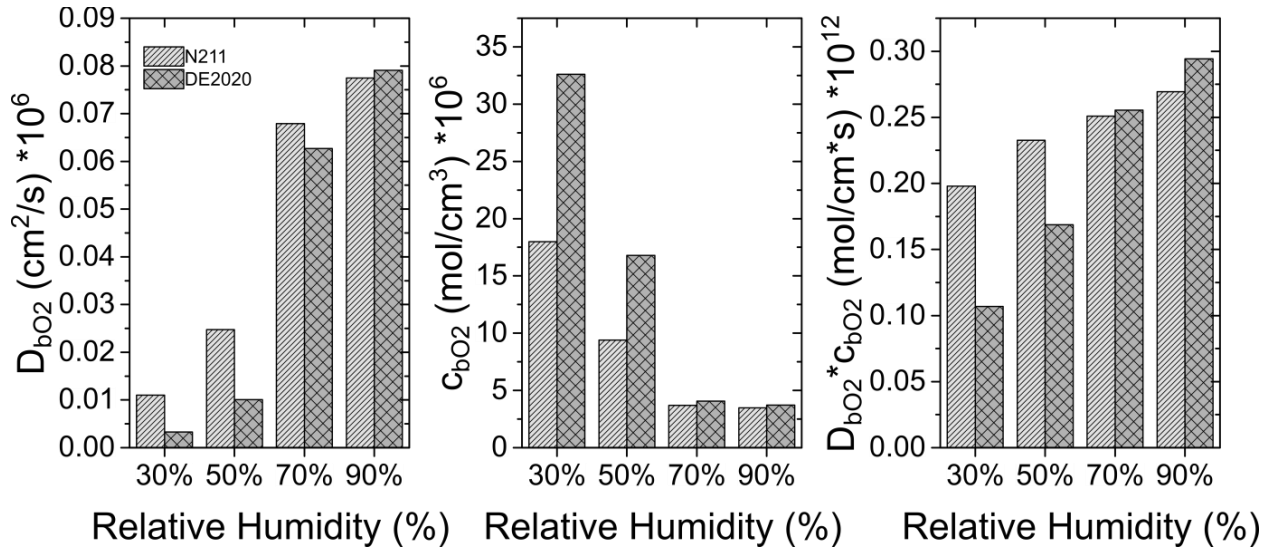


Figure 3.18. O₂ mass transport parameters calculated by non-linear curve fitting versus RH for Nafion 211 membrane and cast DE2020 at 70°C in air, using the effective (corrected) working electrode area.

Oxygen permeabilities (Figure 3.18) obtained by non-linear curve fitting are observed to decrease with relative humidity for both Nafion 211 and cast ionomer, with a similar trend in behaviour compared to linear regression analysis. For the non-corrected (area) datasets (Figure 3.19), D_{bO_2} is observed to decrease as relative humidity is reduced for Nafion 211 except for an increase at 70% RH, and the same lowered alteration as was observed in the linear regression analysis was seen for the cast DE2020. c_{bO_2} increases with lowered RH for Nafion 211 and cast ionomer, where 90% RH has a higher value than 70% RH for both ionomers. The permeability changes with relative humidity for non-corrected (area) datasets show decreasing permeability for Nafion 211 and cast ionomer as relative humidity is lowered. For non-linear curve fitting it was thus crucial to correct for the electrode radius, as in the case of the linear regression analysis.

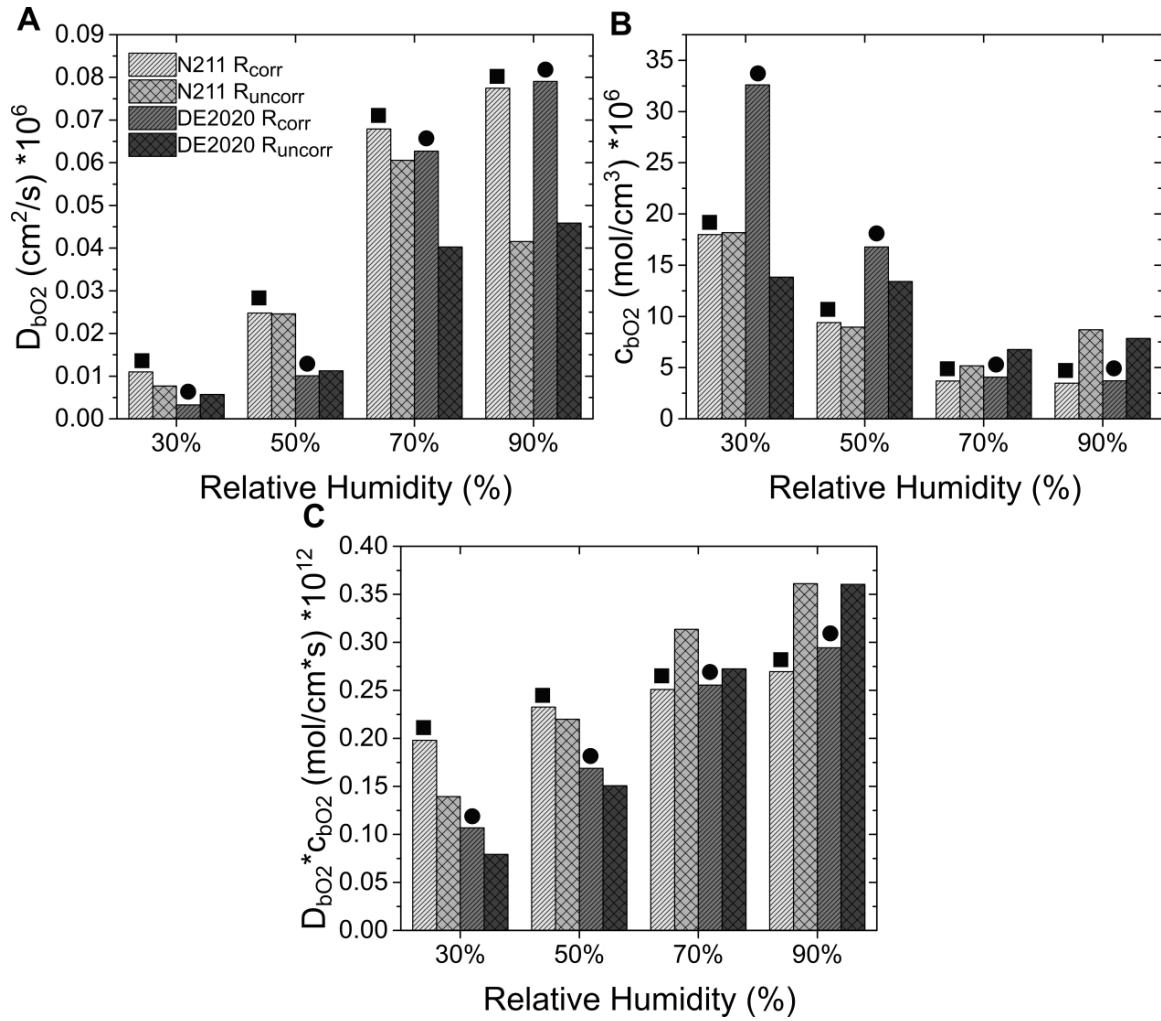


Figure 3.19. O_2 mass transport parameters calculated by non-linear curve fitting versus RH for Nafion 211 membrane and cast DE2020 at 70°C in air, where ■ and ● emphasize r_{corr} , respectively. (A) D_{bo2} , (B) c_{bo2} , (C) $D_{bo2}c_{bo2}$.

3.3.5. Evaluation of analytical treatments

The oxygen permeability can be estimated by the equation which describes the steady state current for a microdisk electrode (Eqn. 2.5) $I(t \rightarrow \infty) = 4nFc_bD_br$. The current at 5 seconds is taken as steady-state, shown in Figure 3.20, which results in an estimated oxygen reduction mass transport limited parameter c_bD_b .

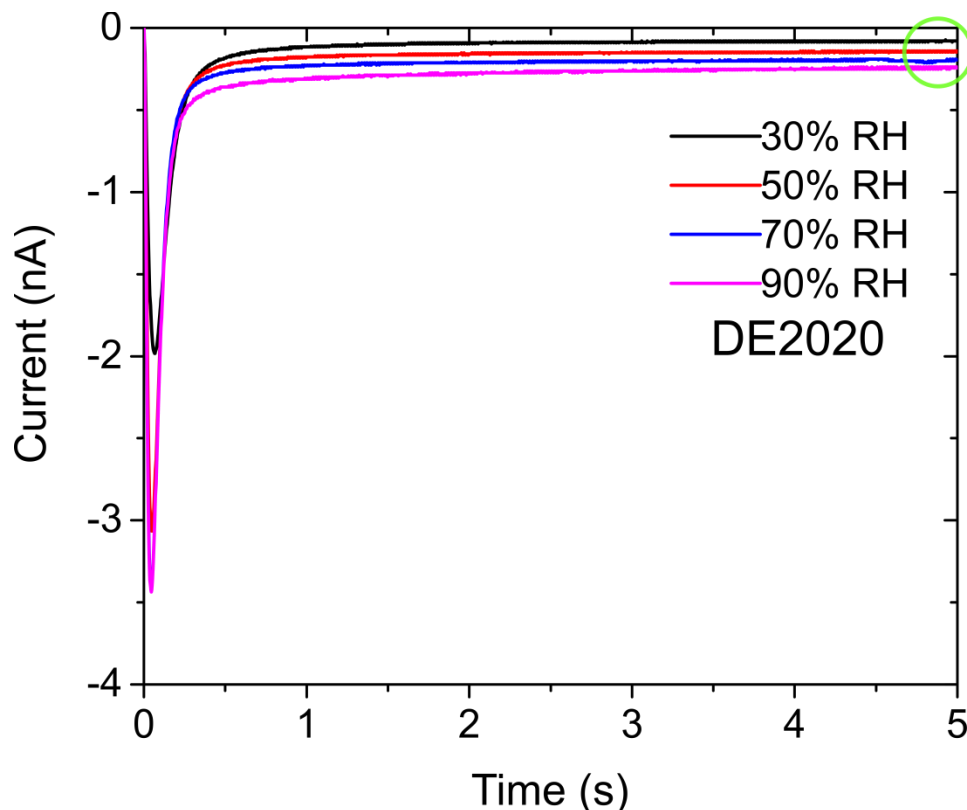


Figure 3.20. Current transients for DE2020 ionomer film at 70°C in air, where the green circle at 5 seconds is taken as the steady-state current.

Plots of the resulting steady-state derived permeability versus values obtained using the Cottrell equation and the Shoup-Szabo equation for both Nafion 211 and DE2020 are shown in Figure 3.21, where values for oxygen permeability from the Cottrell equation are almost an order of magnitude higher than predicted by the steady-state current equation. In fitting short time data with the Cottrell equation the resulting mass transport parameters are impacted greatly by the slope and intercept of the current vs. $t^{-1/2}$ line which can be significantly affected by background noise and range of time used in analysis. For these reasons, nonlinear fitting of the Shoup-Szabo equation was chosen to be used in subsequent work (Chapter 4) over the Cottrell equation as it fits more data points and considers oxygen reduction at short, intermediate, and long times.

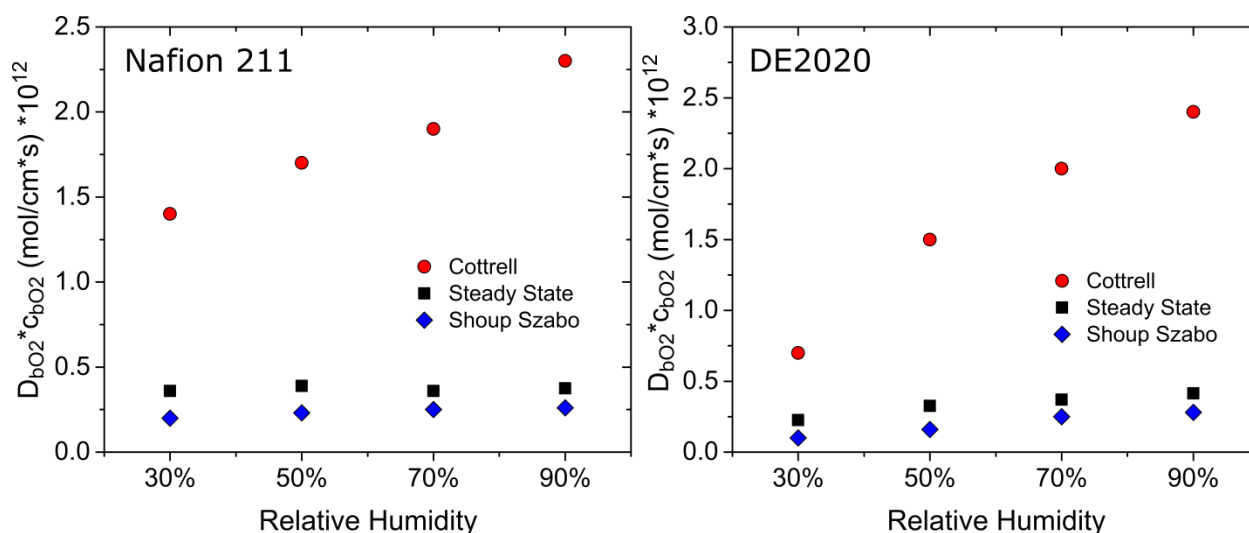


Figure 3.21. O_2 mass transport parameters comparison for steady state, short times (Cottrell), and all times (Shoup-Szabo) in both Nafion 211 and DE2020 at 70°C in air.

3.4. Conclusions

In the present investigation, several experimental and analytical techniques were employed and developed toward the determination of O_2 mass transport parameters under lowered relative humidity and elevated temperature. A two-electrode electrochemical cell was deemed sufficient to use in a low hydration environment compared to a conventional three-electrode configuration. Sampled-current voltammetry was utilized at specific times per relative humidity in order to determine appropriate mass transport limiting potentials. A working electrode area correction was employed in order to account for changes in the effective accessible conductive area of the electrode/electrolyte interface. Solid state chronoamperometric measurements at the Nafion 211/ or cast DE2020/Pt interface were analyzed by linear regression fitting of the Cottrell equation and non-linear curve fitting of the Shoup-Szabo equations, of which both analytical treatments suggest that the relative humidity affects interfacial oxygen mass transport parameters.

For both Nafion 211 membranes and films of DE2020 ionomer in contact with a platinum microdisk the oxygen diffusion coefficient was shown to decrease as relative humidity is reduced, while oxygen solubility was shown to increase. The magnitude of change in the diffusion coefficient decreases more rapidly than the oxygen solubility increases, leading to an oxygen permeability that decreases as the relative humidity is decreased. A comparison of the analytical treatments led to a better correlation between mass transport parameters obtained using the Shoup-Szabo equation and the steady-state current equation, compared to the results of the Cottrell equation.

Chapter 4. Determination of O₂ mass transport at the Pt | HMT-PMBI-OH⁻ interface under reduced relative humidity

This chapter is reproduced from: David Novitski, Aslan Kosakian, Thomas Weissbach, Marc Secanell, and Steven Holdcroft, *Journal of the American Chemical Society*, **2016**, Vol. 138 (47) 15465-15472 with permission from The American Chemical Society. Aslan Kosakian performed the numerical modeling work in Section 4.3.4, which is further explained in Appendix B. Thomas Weissbach performed the water uptake, ion exchange capacity, and lambda measurements described in Sections 4.2.1-4.2.4 and analyzed the data as shown in Section 4.3.1.

4.1. Introduction

Anion exchange membranes (AEMs) for use in alkaline anion exchange membrane fuel cells (AAEMFCs) rely on the transport of hydroxide ions. Benefits of AAEMFCs, over traditional proton exchange membrane (PEM) fuel cells, include the prospect of eliminating noble metal based catalysts.^{18,138,139} Several approaches to designing AEMs having hydroxide ion stability have been explored, and include membranes based on polymers bearing cationic tetraalkylammonium²⁷, phosphonium²⁸, DABCO²⁹, and imidazolium head groups.³⁰ The synthesis of hexamethyl-*p*-terphenyl poly(methylbenzimidazolium) (HMT-PMBI, schematically shown in Figure 4.1), was recently reported.³³ In this ionic polymer the backbone serves as both the hydrophobic and hydrophilic component. Steric hindrance provided by the hexamethyl-*p*-terphenyl (HMT) group alleviates a major degradation pathway, ring opening, caused by hydroxide attack on the C2 position of the benzimidazolium group.^{140,141} The precursor polymer can be controllably methylated to increasing extents to provide ionomers with varying ion exchange capacity (IEC). A polymer with 89% degree of methylation (which corresponds to an ion exchange capacity of 2.5 meq/g) is alcohol or water-alcohol soluble, water insoluble, and exhibits a hydroxide conductivity of 17.3 mS/cm at 95% RH and 90°C.¹⁴² HMT-PMBI-OH⁻ exhibits a high resistance to hydroxide attack: only 6% loss of functional groups after 7 days in 2M NaOH at 80 °C.^{33,142,143}

In basic media, the 4-e⁻ oxygen reduction reaction (ORR, $E^0 = 0.4V$ vs. SHE) occurs according to the following equation:



In the case of catalyst layers in AAEMFCs, a thin hydroxide-conducting ionomer is employed to provide hydroxide ion conductivity, and to provide the basic media for the reaction in the cathode catalyst layer. Oxygen must diffuse into, and transport through, the ionomer film in order to reach catalyst sites and participate in the ORR. Ingress of water into the ionomer is also critical because water is a reactant in the ORR.

Oxygen mass transport in hydroxide conducting ionomers has thus far been sparsely investigated, and the reports that are available use highly humidified or liquid water hydrated conditions.^{82,144} For example, under fully humidified inlet gas streams, oxygen gas permeabilities were observed for a commercially available quaternary ammonium based AEM (Tokuyama A201, Tokuyama Corp., Tsukuba, Japan) in OH⁻ form (3.99×10^{-12} mol/cm·s).⁸² The permeabilities (which are similar to Nafion 211) were attributed to a high oxygen diffusion coefficient in the AEM. Using a hydroxide conducting ionomer (AS-4 ionomer solution, Tokuyama Corp., Tsukuba, Japan) cast on a rotating disk electrode, another study reported an oxygen permeability of 4.99×10^{-12} mol/cm·s in 0.1 M KOH.¹⁴⁴ The same group suggested that mass transport losses observed in an operating fuel cell were attributed to loss of water at the cathode catalyst layer rather than poor oxygen permeability.¹⁹

Solid state electrochemical techniques using microdisk electrodes to study ORR have been used to elucidate oxygen mass transport parameters in PEM materials over a wide range of environmental conditions. It is observed that an increase in temperature, pressure, or IEC ordinarily results in larger oxygen diffusion coefficient and permeability in both perfluorinated and hydrocarbon-based polymers.^{62–66,122,145} In this report solid state electrochemical methods are applied, namely chronoamperometry, to study ORR in HMT-PMBI-OH⁻ films cast from methanol solutions. A comparison of the HMT-PMBI-OH⁻ ORR mass transport parameters is made with respect to a commercially available AEM obtained from FuMA-Tech GmbH, FAA-3, which is a quaternary ammonium-based hydroxide polymer which has been successfully characterized in complete AAEMFC systems.^{146,147}

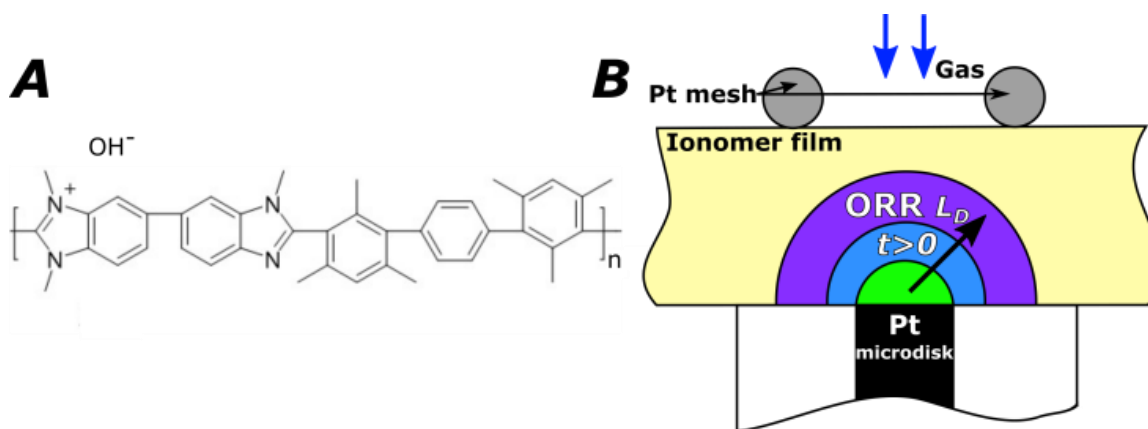


Figure 4.1. (A) Greater than 50% methylation of HMT-PMBI results in HMT-PMBI-OH⁻. The ion exchange capacity is controlled by the degree of methylation (50% methylation corresponds to 0 meq/g, 100% methylation corresponds to 3.14 meq/g). (B) Illustration of the oxygen depletion region (where L_D is diffusion length) in an ionomer film at a Pt microdisk electrode during ORR. The Pt mesh serves as the counter electrode, and allows for gas exchange directly above the platinum microdisk.

In this chapter, the current transients that result from chronoamperometry were analyzed using only the Shoup-Szabo equation to ascertain mass transport parameters. In order to investigate the limitations of the Shoup-Szabo equation for the case of thin films deposited on working electrodes, a numerical model was also developed which accounted for the expanding oxygen depletion region in the films (Figure 4.1B). Characteristic changes in electrochemically active surface area (ECSA) and oxygen mass transport parameters are reported for HMT-PMBI-OH⁻ possessing 3 values of IEC, and for FAA-3 membranes, at 60°C in air. The relative humidity was lowered from near-saturated conditions (98% RH) to 70%, which adds a higher level of complexity to the measurements due to lower water content of the film and an increase in ionic resistance. By reducing the RH, the dependence of ORR on the level of hydration was examined. These data are discussed and compared in the context of varying the IEC, with respect to commercial AEM materials, and with respect to PEM materials, where more is known about ORR mass transport.

4.2. Experimental

The foundation of the numerical model¹ is described in Appendix B. Electrochemical potentials are reported versus a Pt pseudo-reference electrode as described in Chapter 3, which was determined to be approximately -0.875 V vs. the dynamic hydrogen electrode.

4.2.1. Water uptake and lambda measurements

Water uptake and lambda measurements² were performed only on 2.5 meq/g IEC HMT-PMBI-OH⁻ for a basis of comparison with perfluorosulfonic acid membranes (Nafion 211). Films were cast separately from those used on the microelectrodes as a larger mass of sample was required for testing.

4.2.2. Membrane preparation for water uptake and lambda measurements

HMT-PMBI membranes were prepared by dissolving 0.685 g of polymer (HMT-PMBI-I⁻) in 6.170 g MeOH by stirring and gently heating at 65 °C for 12 h to obtain a solution with a concentration of 10 wt%. A 750 µm thick polymer film was cast on a levelled glass plate using a K202 Control Coater casting table and an adjustable doctor blade (RK PrintCoat Instruments Ltd). The polymer film was dried in an oven at room temperature for at least 12 h, peeled off the glass plate, soaked in 5 L distilled water for 24 h, and dried under vacuum at 80 °C for 24 h. Membranes that were cast for the water uptake and lambda measurements had a thickness of 81 ±3 µm.

4.2.3. Ion exchange capacity

The ion exchange capacity (IEC) was determined by acid-base back-titration, described as follows. Potassium hydrogen phthalate (KHP) was dried at 80 °C for 24 hours under vacuum, and an aqueous 11.53 ±0.01 mM solution was prepared. To determine the concentration of the NaOH solution accurately, 10 mL KHP solution was given to 30 mL 2 M NaCl solution and the mixture was titrated to pH=7.000 using a Metrohm 848 Titrino Plus auto-titrator. The accurate concentration of the HCl solution was determined in the same manner. Three membrane samples with dimensions of 2 x 3 cm in Cl⁻ form were soaked twice in 1 M KOH for 24 hours, washed with multiple aliquots of DI water over 48 hours, and placed in 30 mL 2 M NaCl solution for 12 hours. After removing the membranes from the

¹ The numerical model investigation was performed by Mr. Aslan Kosakian (University of Alberta)

² Water uptake, lambda, and ion exchange capacity were measured by Mr. Thomas Weissbach (Simon Fraser University)

solution, 10 mL of an aqueous 6.54 ± 0.03 mM HCl solution was added and the remaining acid was titrated to pH=7.000. The membranes were then washed multiple times with DI water and weighed after drying at 80 °C for 12 hours under vacuum to obtain the dry weight in Cl⁻ form.

The amount of exchangeable ions (n_{X^-}) can be calculated by Eqn. 4.2, where V_{HCl} and [HCl] are volume and concentration of the HCl solution, V_{NaOH} and [NaOH] are the volume and concentration of the NaOH solution, respectively.

$$n_{X^-} = V_{HCl} \cdot [HCl] - V_{NaOH} \cdot [NaOH] \quad (4.2)$$

The IEC in hydroxide form was calculated according to Eqn. 4.3, where m_{dry,Cl^-} is the dry mass of the membrane sample in chloride form and M_{Cl^-} and M_{OH^-} are the molar mass of chloride and hydroxide, respectively.

$$IEC_{OH^-} = \frac{n_{X^-}}{m_{dry,Cl^-} + n_{X^-} \cdot (M_{OH^-} - M_{Cl^-})} \quad (4.3)$$

The reported IEC values are the average over three samples (standard deviation shown below). The IEC was also determined from the degree of methylation (dm) by NMR according to Eqn. 4.4, where dm is the degree of methylation in %, $M_{50\%}$ the molar mass of one repeating unit with a 50% dm (572.8 g/mol) and M_{MeOH} the molar mass of methanol, respectively.

$$IEC_{NMR} = \frac{4 \cdot \frac{dm - 50\%}{100\%}}{M_{50\%} + 4 \cdot M_{MeOH} \cdot \frac{dm - 50\%}{100\%}} \quad (4.4)$$

The dm of the HMT-PMBI polymer used in the water uptake and lambda measurements was determined to be $89.2 \pm 0.5\%$. Based on the dm, the ion exchange capacity (IEC_{NMR}) is 2.52 ± 0.2 mmol/g for the OH⁻ form. Acid-base titration showed about 20% lower IEC values: IEC_{OH^-} was found to be 2.00 ± 0.06 mmol/g. The reason for the discrepancy between methodologies of IEC determination can include incomplete ion exchange during preparation or inaccessible ion exchange sites during the back titration measurements. Seeing as how there can be $\cong 20\%$ variation between methods, the NMR derived values for IEC are cited throughout this manuscript for ease of comparison to the accompanying degree of methylation. It must be noted, however, that the experimentally

determined value of 2.00 mmol/g was used in calculating water uptake and lambda values for the 89% dm HMT-PMBI-OH⁻, the details are described below.

4.2.4. Water uptake

The membrane samples in iodide form were immersed in argon purged 1 M KOH solution for 24 hours and washed several times with argon purged DI water over 24 hours in a closed container until the wash solution was a neutral pH. The wet membranes (now in OH⁻ form) were quickly placed in a Surface Measurement Systems DVS Advantage dynamic vapour sorption (DVS) analyzer at 60 °C running under nitrogen purge. After an initial equilibration for 6 hours at 95 % relative humidity (RH), the RH was incrementally decreased after a minimum of 4 hours of equilibration time at each RH. The average mass at a given RH ($m_{x\%RH}$) and RH and deviation of the last 30 minutes of each equilibration was used to calculate the RH-dependent water uptake according to Eqn. 4.5, where $m_{0\%RH}$ is the mass at 0 % RH.

$$water\ uptake_{x\%RH} = \frac{m_{x\%RH} - m_{0\%RH}}{m_{0\%RH}} \quad (4.5)$$

The water uptake can also be expressed with a dependence on the amount of available ion exchange groups as described in Eqn. 4.6, where $\lambda_{x\%RH}$ is the RH-dependent number of water molecules per ion exchange site, M_{H_2O} is the molar mass of water and IE_{OH^-} the ion exchange capacity determined by acid-base titration.

$$\lambda_{x\%RH} = \frac{water\ uptake_{x\%RH}}{M_{H_2O} \cdot IE_{OH^-}} \quad (4.6)$$

4.2.5. Film preparation for the solid state electrochemical cell

HMT-PMBI-I⁻ at 82%, 86%, and 89% degrees of methylation (corresponding to ion exchange capacities of 2.1 meq/g, 2.3 meq/g, and 2.5 meq/g, respectively) were synthesized³ according to a previously published method, and solutions were prepared having 10 wt% in methanol to aid in solvent evaporation when drop casting onto the working electrode.³³ The same 5 µm radius platinum microdisk working electrode used in Chapter 3 was used here in the same way. To cast ionomer dispersions on

³ HMT-PMBI-I⁻ was synthesized by Dr. Andrew Wright (Simon Fraser University)

the working electrode, after polishing and washing with MilliQ water, the electrode was held upright in a clamp and dried with a heat gun. For HMT-PMBI-I⁻ ionomer, a glass capillary was used to coat the disk surface as well as ~2 mm down the sides of the electrode in order to ensure no separation of the film from the electrode during immersion in hydroxide for OH⁻ exchange. A heat gun was used (<30 s) to assist in driving off solvent.

A FuMA-Tech GmbH FAA-3 anion exchange membrane, reported to have an ion exchange capacity of 2.0 meq/g, was immersed in 1M KOH for 48 hours before use, followed by a brief rinse with MilliQ water. The ionomer films and FAA-3 membrane were considered to be in the mixed carbonate form as no steps were made to prevent exposure to CO₂-containing air. As experiments are conducted where the oxygen reduction reaction is allowed to proceed, conversion of carbonate species to hydroxide at the electrochemical interface is expected to occur.¹⁴⁸ With this in mind, to the ionomer films and membranes are referred to as in the OH⁻ form.

4.2.6. Solid-state electrochemical cell

Using the same electrochemical cell as in Chapter 3, only variations are noted in Chapter 4. For modeling purposes, an assumption was made that the space directly above the working electrode was a mesh pore exposed to the environment to facilitate oxygen diffusion through the ionomer-gas interface. FAA-3 membranes were inserted into a vertically aligned membrane holder which is open on both sides where the pseudo-reference and working electrodes sandwiched the membrane. Once ionomer samples were loaded into the environmental chamber, the relative humidity was held at 90% RH at 60°C for 1 hour to allow for equilibration from the initial liquid state, before measurements were taken. After switching relative humidity values, at least 10 minutes were allowed for equilibration. After experiments, cast ionomer for HMT-PMBI-OH⁻ was removed from the working electrode and checked for thickness with a micrometer, and samples for all degrees of methylation were 53.8 ±1.6 μm. Post experiment micrometer measurement of the FAA-3 membrane gave a thickness of 52.3 ±1.3 μm.

4.2.7. Chronoamperometric, potential step measurements

Chronoamperometry of the ORR was performed by holding the working electrode at a potential where no Faradaic reaction occurs (+0.2 V vs. Pt), and switching to a potential where ORR is mass transport limited (e.g., -0.5 V vs. Pt) at an acquisition rate of 400 data points per second within a current range of 10 nA. The mass transport limiting potential region for ORR was determined by linear sweep voltammetry between +0.2 V and -0.5 V vs. Pt using a scan rate of 150 mV/s. Current transient

responses from the ORR mass transport limiting region were reproducible, and the averaged current transient was analyzed using the Shoup-Szabo equation (Eqn. 3.1). Nonlinear curve fitting was performed using *MATLAB* software. The *MATLAB* script used to fit the current transients required truncation of several initial data points in order to eliminate contributions of non-faradaic (double layer) charging. This step was performed as it is generally considered to be good practice to disregard at least the first 5 cell time constants, $R_u \cdot C_d$, (where R_u is uncompensated resistance and C_d is double-layer capacitance), in order to assume an instant change in interfacial oxygen concentration at the adjusted $t=0$ (non-faradaic charging complete).² In determining oxygen transport coefficients in thick Nafion films, Kudo and coworkers disregarded the first 0.2 seconds of data to account for double-layer discharging.⁸⁰ In this work, a time truncation of $\cong 0.2s$ was also deemed sufficient.¹⁴⁹ The *MATLAB* script includes time shifting in the fitting, so as to dynamically account for the non-faradaic charging removed during truncation, and sets the initial point of the truncated data at $t=t_{trunc}-t_{shift}$ in order to provide a reliable fit that removes all temporal electrochemical effects. If the fitting algorithm truncated the first 200 ms of data, then the script would shift the data (beginning at $t=0.201s$) by $-0.200s$, so that the Shoup-Szabo equation could be applied correctly. Shifting the current transient time after accounting for non-Faradaic charging has been previously applied by Xiong *et al.* in the determination of mass transport coefficients in acetonitrile and ionic liquids.¹²⁷

4.3. Results

4.3.1. Water uptake and lambda

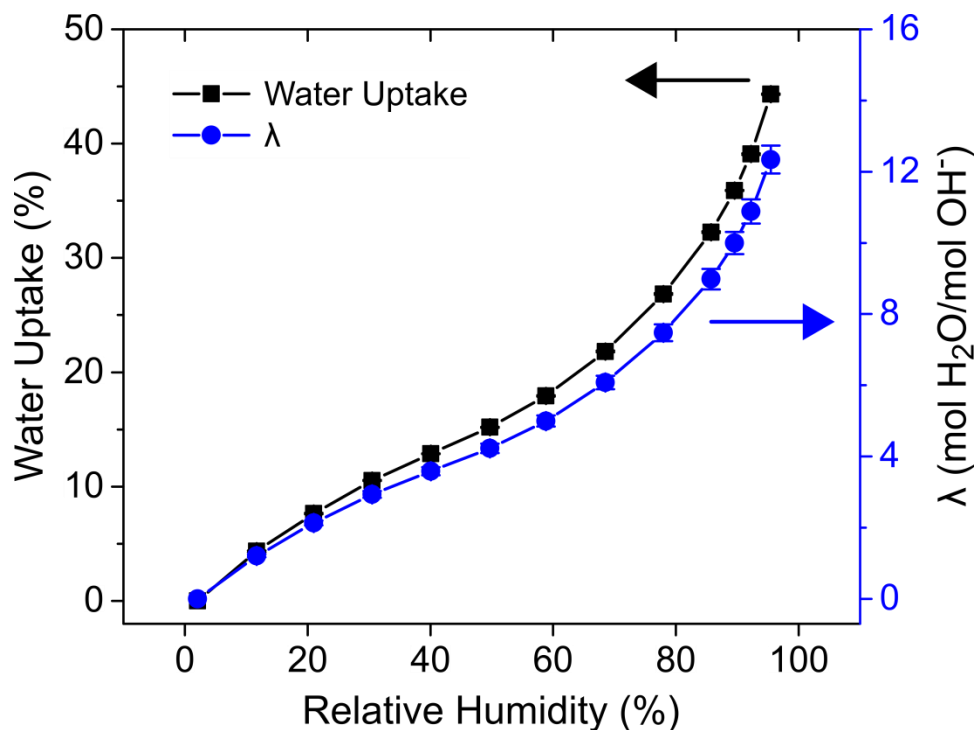


Figure 4.2. Water uptake and water molecules per ion exchange site (λ) of 2.5 meq/g HMT-PMBI-OH⁻ as a function of RH at 60 °C. Film thickness 81 ± 3 μm .

As the water content of ionomer films was expected to influence ORR parameters, water uptake was measured and the number of water molecules per ion exchange site (λ) as a function of RH were calculated (shown in Figure 4.2). Both water uptake and λ increase linearly from 20% to 75% RH. At 75% RH, 6 water molecules are present for each ion exchange site. At RH higher than 75%, λ increases exponentially, reaching a value of 12 at 95% RH. λ values for HMT-PMBI-OH⁻ (2.5 meq/g IEC) are similar to those reported for Nafion 211 under similar conditions.²⁵

4.3.2. Electrochemically active surface area

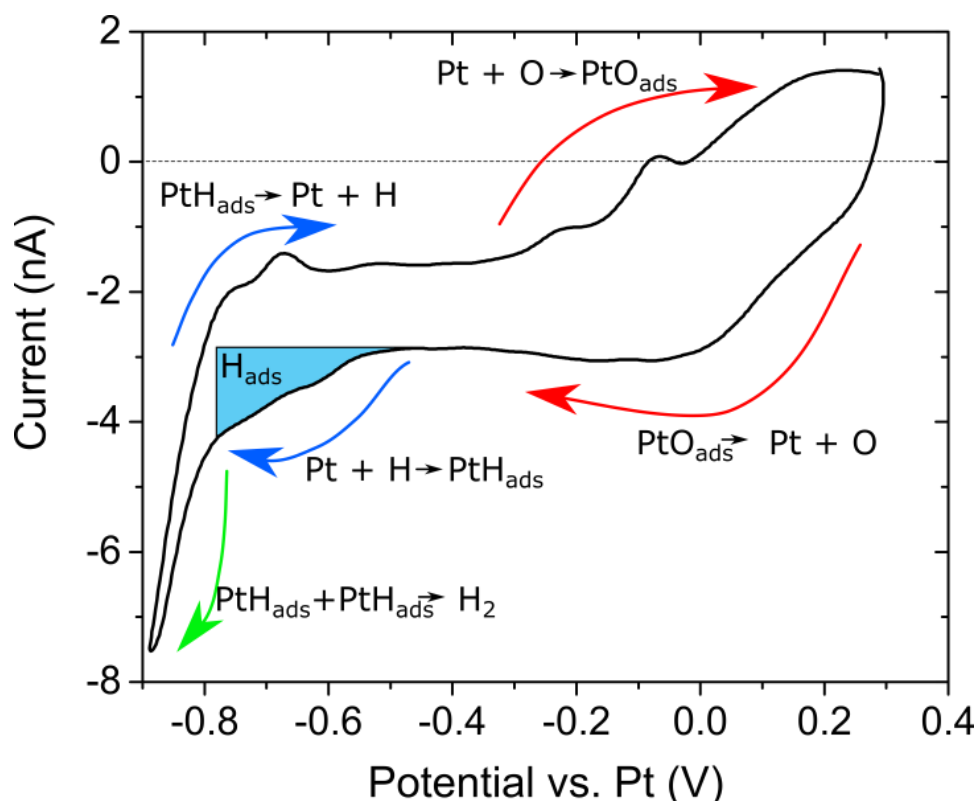


Figure 4.3. Cyclic voltammogram for 2.5 meq/g HMT-PMBI-OH⁻ at 90% RH and 60 °C, with scan rate of 250 mV/s. Platinum oxide reduction and oxidation is represented by lower and upper red arrows, respectively. Hydrogen adsorption and desorption is represented by the lower and upper blue arrows, respectively. Hydrogen adsorption charge density is used for effective surface area. Green arrow corresponds with hydrogen evolution.

A representative cyclic voltammogram (CV) obtained for HMT-PMBI-OH⁻ (IEC 2.5 meq/g) at 60°C, 90% RH is shown in Figure 4.3. The cathodic current bias results from the presence of oxygen in the air in the environmental chamber. Representative CVs for other hydroxide conducting ionomer films are shown in Figure 4.4. As can be seen in Figure 4.3, sweeping the applied potential to values more negative than the initial +0.3 V versus the pseudo-Pt reference electrode gives rise to a peak which is due to the reduction of platinum oxide (-0.06 V), followed by cathodic current due to hydrogen adsorption, which onsets at -0.5 V, and hydrogen evolution which onsets at -0.8 V. On the reverse potential sweep, anodic current due to hydrogen desorption onsets at -0.77 V, followed by platinum oxide formation which onsets at -0.26 V. The CV indicates that the ORR is occurring at the Pt electrode and that the ionomer is supporting ORR, i.e., it does not poison the catalyst.

For ionomers and membranes used in this study, standard hydrogen underpotential deposition methods were used in the determination of ECSA.¹⁰⁴ This was achieved by integrating the charge

under the H adsorption region, from -0.5 V to -0.77 V vs Pt for the 2.5 meq/g IEC HMT-PMBI-OH⁻ ionomer case (Figure 4.3). The potentials for hydrogen adsorption were chosen based on the typically reported potentials for hydrogen underpotential deposition between 0.05 V and 0.4 V versus reversible hydrogen electrode (RHE) cited in literature, shifted to more negative potentials by about 875 mV for the platinum pseudo-reference electrode.¹⁵⁰ The range of potentials used for hydrogen adsorption varied between 25 and 50 mV based on relative humidity, as drying of the ionomer results in increased anion (sulfonic acid) adsorption on the platinum, which has been observed to shift the hydrogen adsorption/desorption region to more negative potentials.^{132,134}

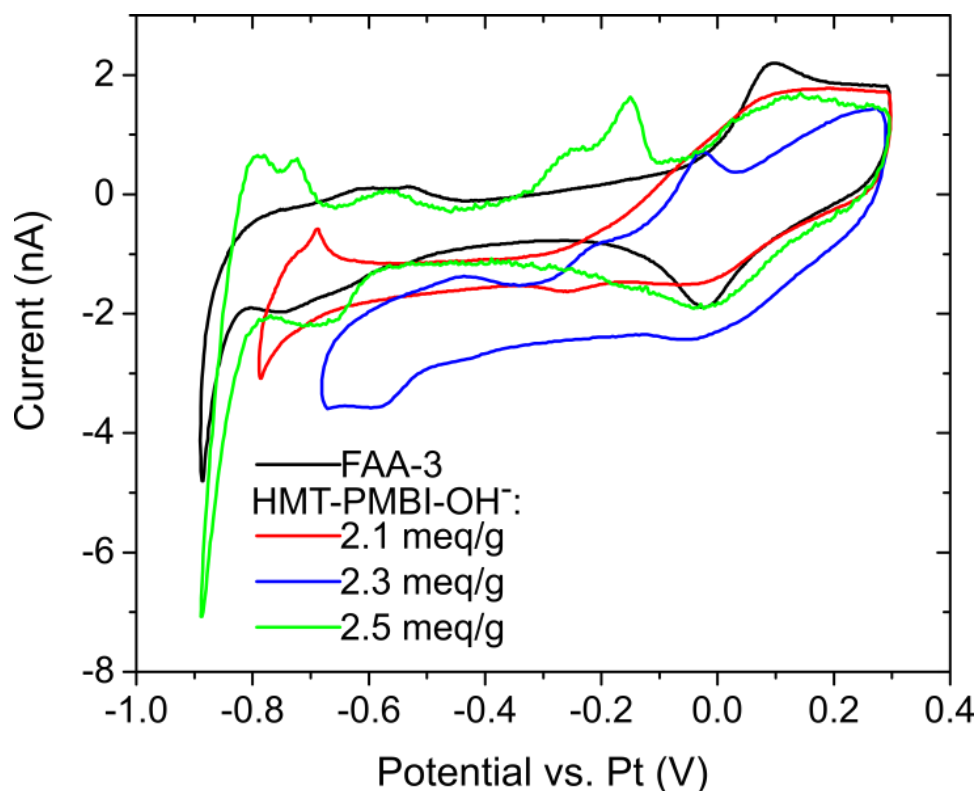


Figure 4.4. Cyclic voltammograms for ionomer samples at 90% RH and 60 °C, with scan rate of 250 mV/s, except for 2.3 meq/g which had a scan rate of 500 mV/s (corrected for in surface area calculations).

From Figure 4.4, a shift in the hydrogen underpotential deposition region depending on the sample was observed, thus the H_{ads} potential range was accounted for in the ECSA calculation. Lindström et al. have shown that the hydrogen underpotential deposition region is influenced by hydration conditions as well as the nature of the electrochemical interface, which may help explain the range of potentials for H_{ads} and H_{des} .¹³³ The platinum oxide reduction peaks, however, were consistently near 0.0 V vs. Pt for all samples as shown in Figure 4.4.

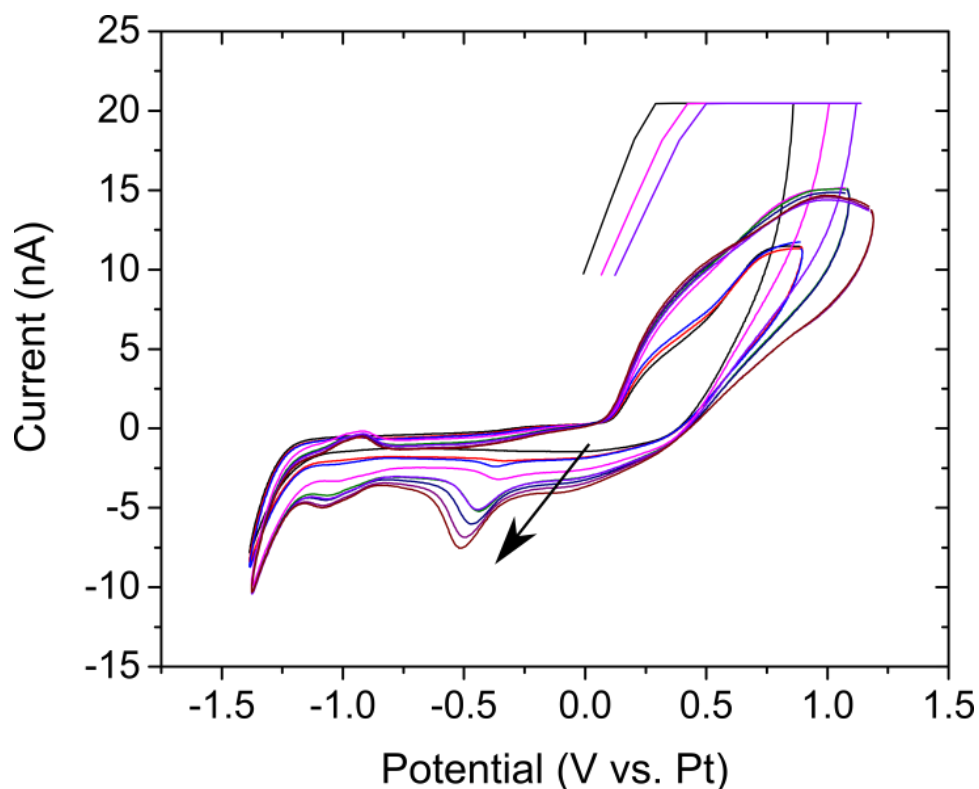


Figure 4.5. Cyclic voltammogram of 2.5 meq/g HMT-PMBI-I⁻ at 70% RH, 70 °C in air at 250 mV/s. After first 3 scans, upper potential range was changed from +0.9 V to +1.1 V. Arrow denotes increasing scan number.

A cyclic voltammogram of HMT-PMBI-I⁻ is shown in Figure 4.5, which displays a lack of H adsorption/desorption (near -1.0 V) in the first scan (black line) attributed to strong I species adsorption on the Pt electrode surface. Over the course of three minutes of cyclic voltammetry, noticeable peak shapes emerged, attributed to the interfacial generation of hydroxide ions during ORR displacing the adsorbed I species, where Pt-O reduction emerges near -0.5 V and H adsorption/desorption emerges at -1.0 V. Ionomer-film coated electrodes were immersed overnight in 1 M KOH to convert from iodide to hydroxide form, where CV's which showed consistent peaks similar to the final scans from Figure 4.3 were used to qualitatively show conversion from I⁻ to OH⁻ forms.

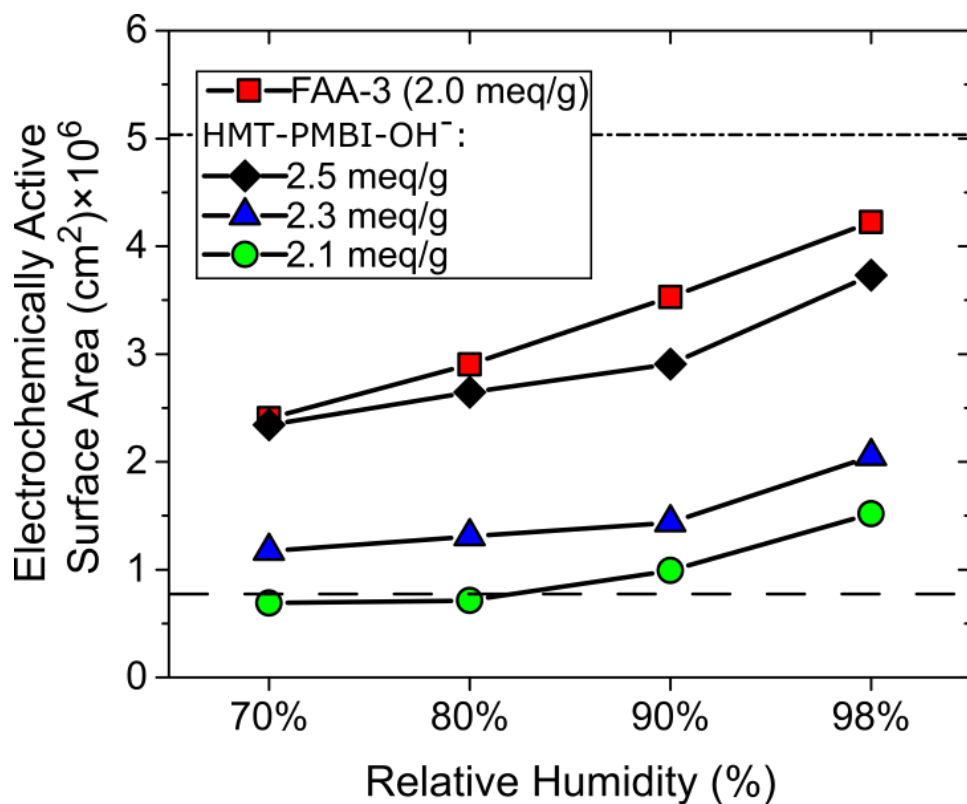


Figure 4.6. Calculated effective working electrode surface area at 60°C in air. Dashed line (---) indicates the geometric surface area, $7.85 \times 10^{-7} \text{ cm}^2$, while double dash-dash (- - - -) line represents the maximum effective surface area of the electrode in 1M KOH, $5.05 \times 10^{-6} \text{ cm}^2$.

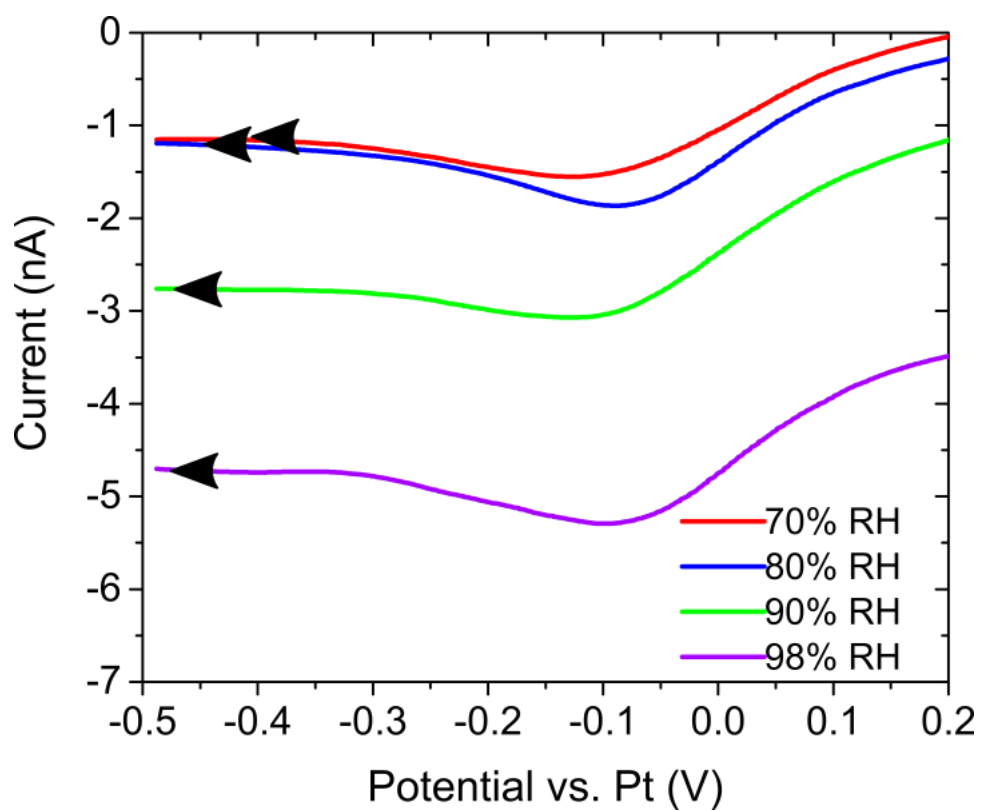


Figure 4.7. Linear sweep voltammograms for 2.5 meq/g HMT-PMBI-OH⁻ at 60°C in air, 150 mV/s scan rate. Arrows denote sweep direction.

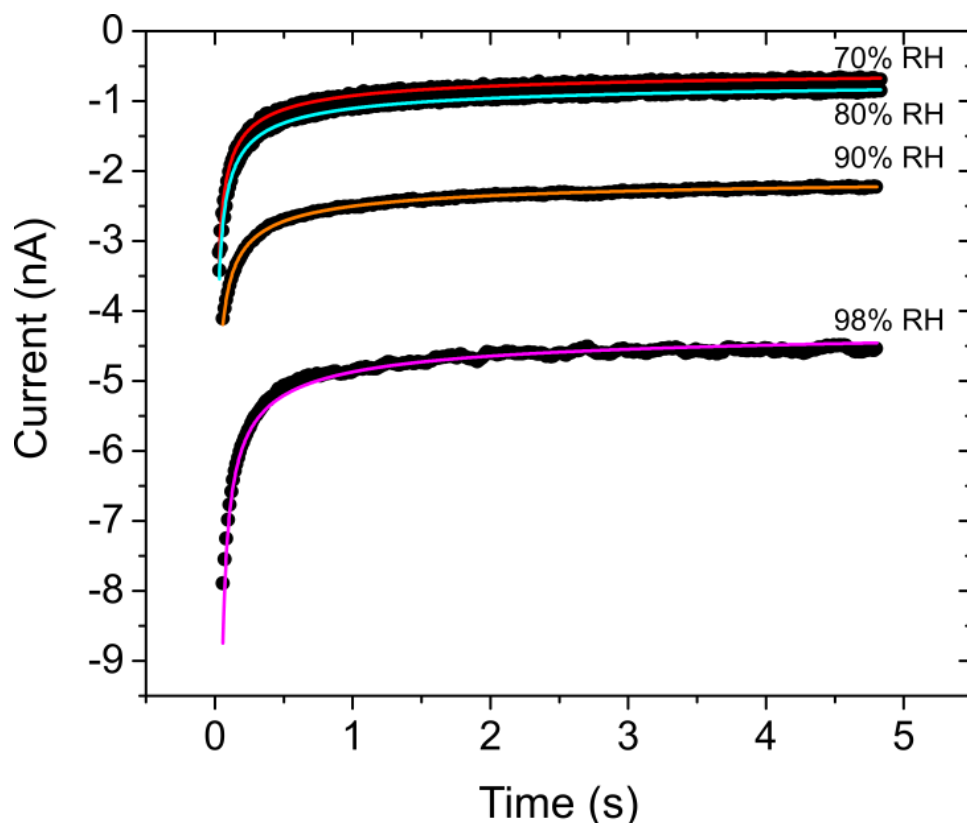


Figure 4.8. Oxygen reduction reaction current transients for HMT-PMBI-OH⁻ 2.5 meq/g at 60°C in air. Least squares fit solutions for the Shoup-Szabo equation are overlaid as fitted curves.

Lindström et al. observed a marked decrease in the ECSA of carbon supported Pt catalyst in a membrane electrode assembly when the RH was decreased.¹³³ The lower ECSA was attributed to an increase of hydrophobic character at the ionomer-electrode interface blocking access to the Pt surface. Similar behaviour has been revealed through conductive atomic force microscopy, where the interfacial conductive area drastically dropped from ~95% active area at 84% RH to 4.1% at 30% RH for Nafion 212 membrane.¹²¹ In order to determine whether a similar interfacial inversion occurs in anion exchange ionomers, the ECSA of the Pt microdisk electrode was calculated from cyclic voltammograms at 60°C under different conditions of RH by integrating the charge due to hydrogen adsorption (between -0.5 V and -0.77 V vs. Pt) after correcting for double-layer charging. Khadke and Krewer calculated the ECSA for Pt/C coated particles with a thin film of anion exchange ionomer (AS-4, Tokuyama) in 0.1 M KOH by averaging the charges for the H_{ads} and H_{des} peaks.¹⁴⁴ In the present investigation only the H_{ads} peak is used for ECSA determination because the H_{ads} and H_{des} peaks are distorted cathodically by the early onset of the H_2 evolution peak, caused at low RH and on polycrystalline electrodes, a limitation of the solid-state electrochemical setup.¹³³

The calculated ECSA values are shown in Figure 4.6, wherein the dashed line represents the geometric surface area of the working electrode. The effective surface areas obtained are higher than the geometric area due to surface roughness which is typically >2 for polycrystalline platinum, but lower than the ECSA determined in aqueous KOH (1M).⁶⁵ As RH is lowered, a decrease in the electrochemically active surface area is observed for all thin films studied, which is attributed to a collapse of ionically conductive domains at the electrode interface with decreasing water content. The decrease in ECSA with a reduction in RH is congruent with the ECSA measurements on perfluorinated proton exchange polymers in Chapter 3. The IEC of the HMT-PMBI-OH⁻ samples affects the ECSA, where a higher IEC, and therefore higher water content, results in a higher ECSA throughout the RH values investigated. FAA-3 membrane, with an IEC of 2.0 meq/g, on the other hand, exhibited an ECSA higher than the 2.5 meq/g HMT-PMBI-OH⁻ film, suggesting different ionic channel characteristics of the two polymers. As a point of context, at 70% RH the electrochemically active surface area of the films decrease to approximately half their original surface area at 98% RH for all samples investigated, which is similar to the conducting active area observed for Nafion 212 membrane at 70% RH.¹²¹ The effective ECSA for the working electrode was used to determine an effective radius, r_{eff} , in the calculation of D_{bO_2} and c_{bO_2} (r_{eff} was computed using $\pi r_{eff}^2 = ECSA_{eff}$). The use of r_{eff} instead of the geometric radius is justified based on the results of Chapter 3.

4.3.3. Potential step chronoamperometry

The initial and final applied potential values used for potential step chronoamperometry were based on linear sweep voltammograms, LSV, shown in Figure 4.7. There exists an offset in total current resulting in lower total currents with decreasing relative humidity. This current shift, which results in a lower limiting current as well as slower kinetic responses, result from increased ohmic resistance contributions as the anion conductivity decreases as relative humidity was lowered.¹⁵¹ From LSVs, the initial potential of +0.2 V vs. Pt was chosen since it was outside the mass transport limiting region and before oxide formation. The final potential ranged from -0.4 to -0.5 V vs. Pt as this region was well within ORR mass transport limiting conditions. The chronomperometric current transients obtained by stepping from +0.2 V to -0.4 V and from +0.2 V to -0.5 V were averaged, with a maximum error obtained from range-normalized root mean square deviation (NRMSD, Eqn. 4.7) between averaged and original experimental transients of 3.9% for 2.3 meq/g IEC HMT-PMBI-OH⁻ at 98% RH (1% average deviation across the other samples). Representative current transients for 2.5 meq/g IEC HMT-PMBI-OH⁻ at 60°C and under RH between 70 to 98% are shown in Figure 4.8, together with least squares fits of the Shoup-Szabo equation to the current transients. 2D contour plots of the relative errors, where the diffusion coefficient and solubility are the y- and x- axis, respectively, have been

previously reported and are used to graphically indicate the range of solutions to the Shoup-Szabo equation with the lowest error.¹²⁷ Least squares fitting of the averaged current transient resulted in a best fit exhibiting 0.66% error, shown as the red point in Figure 4.9, while the green domain corresponds to Shoup-Szabo equation fits with an error less than the NRMSD of the averaged sets (i.e., <1.2% for the case of Figure 4.9). Other ionomer films yielded similar contour plots and error percentages (i.e., approximately 1% error).

$$NRMSD = \frac{\sqrt{\sum_{i=1}^m \frac{(I_{exp,i} - I_{avg,i})^2}{m}}}{\max(I_{exp}) - \min(I_{exp})} \quad (4.7)$$

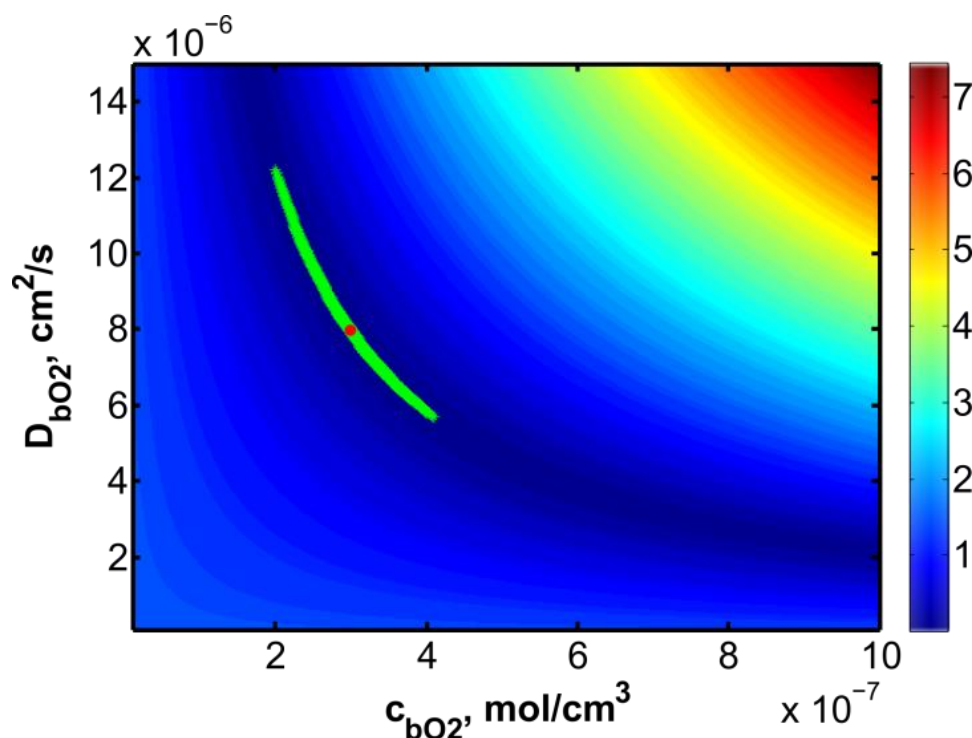


Figure 4.9. Contour plot for solutions of the Shoup-Szabo equation for 2.5 meq/g HMT-PMBI-OH⁻ at 98% RH and 60 °C in air. The colour corresponds to % error, with the solution of minimum error being the red point and points that lie within experimental error represented by green points.

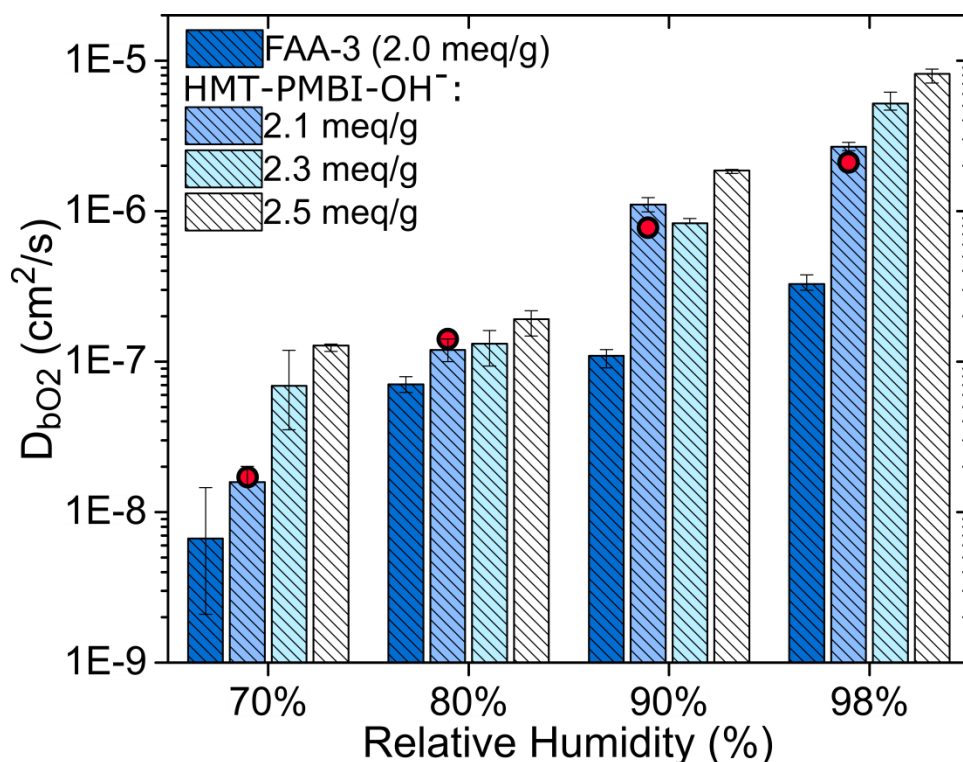


Figure 4.10. Oxygen diffusion coefficients obtained for HMT-PMBI-OH⁻ ionomer films and FAA-3 membranes by least squares fitting of the Shoup-Szabo equation versus RH, 60°C in air. The red points indicate values obtained for HMT-PMBI-OH⁻ 2.1 meq/g from numerical modeling (see text). Error bars correspond to the range of solutions for the mass transport limited current transients fit to the Shoup-Szabo equation.

Calculated oxygen diffusion coefficients obtained from least squares fitting are shown in Figure 4.10, where the best fitting error is generally < 1%. In both the HMT-PMBI-OH⁻ series and FAA-3 ionomers, at any specific relative humidity, D_{bO_2} displays a downward trend with decreasing IEC. This is because oxygen diffusion is correlated to the water content; where water content is proportional to the IEC within a similar family of polymer. For a given IEC, as RH is lowered there is a corresponding decrease in the oxygen diffusion coefficient. For example, the oxygen diffusion coefficient decreased by a factor of 170, 75, and 64 for the HMT-PMBI-OH⁻ series exhibiting 2.1, 2.3, and 2.5 meq/g IEC when the RH was decreased from 98% to 70%. The magnitude of the change in D_{bO_2} for HMT-PMBI-OH⁻ films indicates that the higher the IEC, the less sensitive changes in RH are compared to lower IEC films. By comparison, FAA-3 membrane (IEC 2.0 mmol/g), decreased by a factor of 49 as RH was lowered from 98% to 70%.

Oxygen solubility values determined by chronoamperometry are shown in Figure 4.11, where oxygen solubility is observed to decrease with increasing IEC at a specific RH. Given that molecular oxygen predominantly prefers to dissolve in hydrophobic domains the findings are consistent with the

highest c_{bO_2} value being observed for polymers with the lowest water content, which occurs under conditions of lowest RH and polymers with the lowest IEC. For example, the oxygen concentration increases by a factor of 10 for HMT-PMBI-OH⁻ 2.1, 2.3, and 2.5 meq/g IEC when the RH is reduced from 98% to 70%. For FAA-3, the oxygen concentration increases by a factor of 12 upon decreasing RH from 98% to 70%.

Oxygen permeability, $D_{bO_2}c_{bO_2}$, obtained from the product of oxygen diffusion coefficient and solubility are shown in Figure 4.12. Also plotted, as a green star, is the oxygen permeability calculated from the pseudo-steady-state current, I_{ss} , obtained at $t = 5s$ in the current transient (e.g. see Figure 4.8) using Eqn. 4.8:

$$I_{ss} = -4nFrD_{bO_2}c_{bO_2} , \quad (4.8)$$

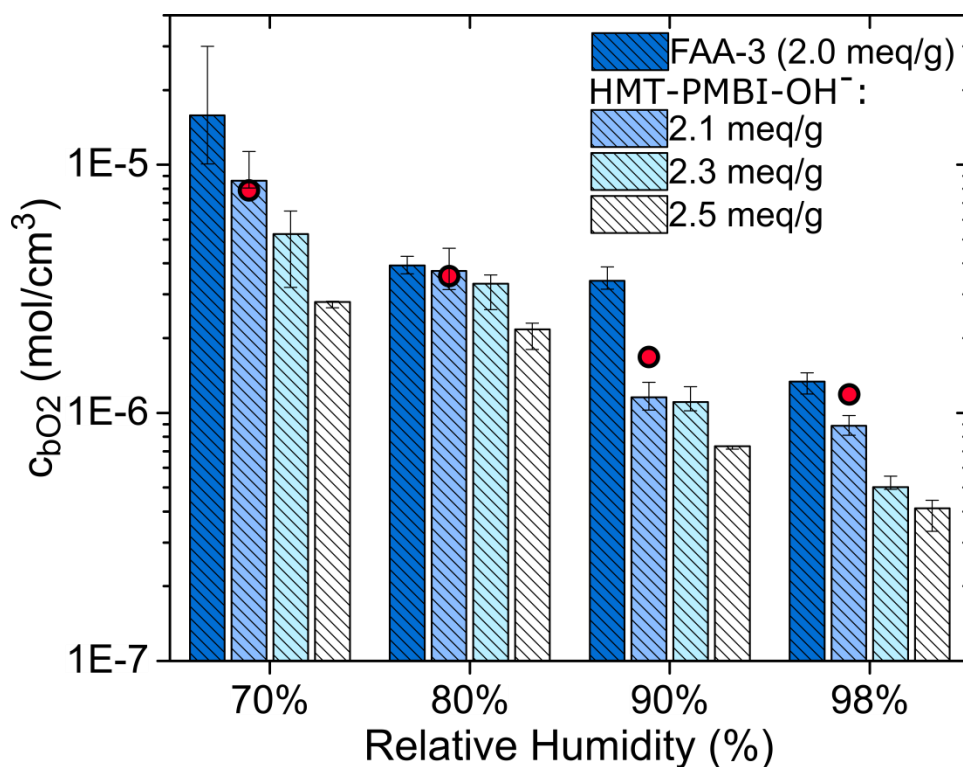


Figure 4.11. Oxygen solubility obtained for HMT-PMBI-OH⁻ ionomer films and FAA-3 membranes by least squares fitting of the Shoup-Szabo equation versus RH, 60°C in air. The red points indicate values obtained for HMT-PMBI-OH⁻ 2.1 meq/g from numerical modeling. Error bars correspond to the range of solutions for the mass transport limited current transients fit to the Shoup-Szabo equation.

where n is equal to 4, F is 96,485 C/mol, r (cm) is the radius of the electrode (calculated from the effective electrode surface area). The permeability obtained from I_{ss} are generally larger than those obtained from curve fitting, with oxygen permeability being within 12% of the curve fit values at 98%

RH, or as high as 100% in variation at lower RH, e.g., 70% RH. The variation in permeability obtained through fitting the Shoup-Szabo equation and extracted from I_{SS} can be explained by the fact that the latter method only uses one data point, and is not at a true steady state, whereas the former technique incorporates contributions from short, intermediate, and long periods of time after stepping to ORR potentials. Within the HMT-PMBI- OH^- series at a specific RH the permeability is observed to decrease with decreasing IEC. At a specific RH, as in investigations with hydrocarbon proton exchange membranes of varying IEC, there is no definitive trend.⁶² Comparing the extent with which the oxygen diffusion coefficient decreases to that with which the oxygen solubility increases (see Figure 4.10 and Figure 4.11), oxygen diffusion is the dominant factor that causes the oxygen permeability to decrease as RH is lowered. The oxygen permeability decreases by a factor of 4 for FAA-3; and 17, 7, and 7, for HMT-PMBI- OH^- 2.1, 2.3, and 2.5 meq/g IEC, respectively, upon decreasing the RH from 98 to 70%.

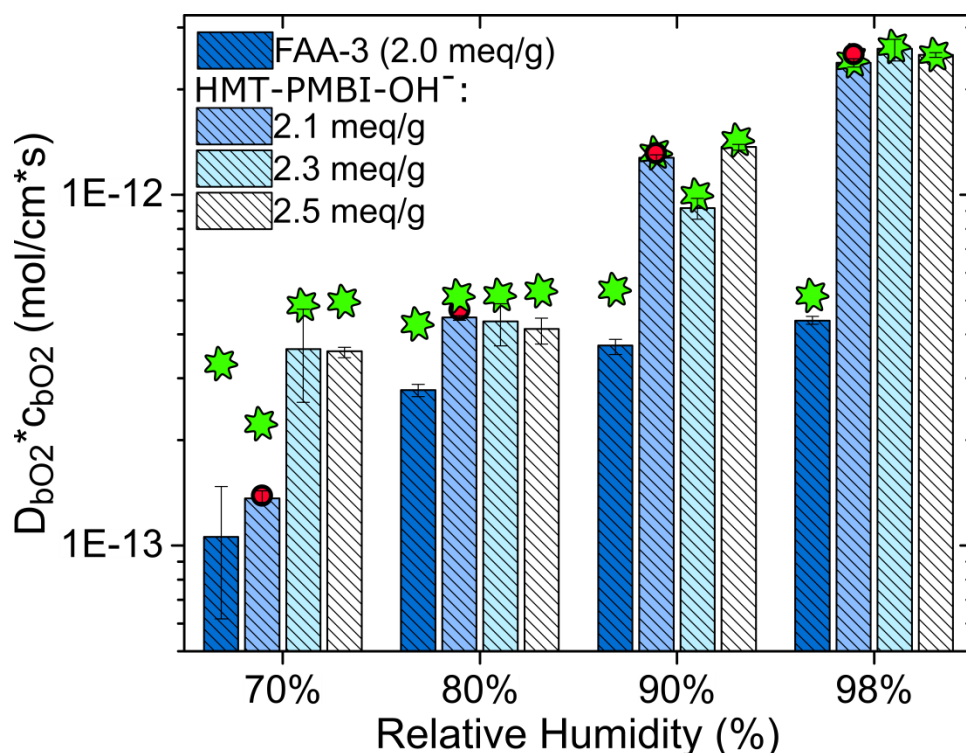


Figure 4.12. Oxygen permeability obtained for HMT-PMBI- OH^- ionomer films and FAA-3 membranes by least squares fitting of the Shoup-Szabo equation versus RH, 60°C in air. Green stars represent permeability determined from steady state current, while red points indicate values obtained for HMT-PMBI- OH^- 2.1 meq/g from numerical modeling. Error bars correspond to the range of solutions for the mass transport limited current transients fit to the Shoup-Szabo equation.

The HMT-PMBI- OH^- 2.5 meq/g film displays almost 5 times higher oxygen permeability at 90% RH, but half the oxygen permeability at 70% RH, compared to Nafion 211 values in Chapter 3. Further comparison reveals that FAA-3 exhibits a slightly higher oxygen permeability at 90% RH compared to

Nafion 211 but half the permeability at 70% RH. Since the rate of oxygen diffusion (and by association, water content) have been considered to play a dominant role in oxygen permeability, the combination of high IEC and absence of an oxygen-dissolving, fluorine backbone in hydrocarbon films, explain the higher oxygen permeability for alkaline membranes at high RH.

A Tokuyama A201 quaternized ammonium anion exchange membrane (IEC 1.8 meq/g) is reported to exhibit a D_{bO_2} of 4.29×10^{-6} cm²/s under full hydration, 1 atm oxygen, at 20°C. c_{bO_2} is reported to be 0.93×10^{-6} mol/cm³, and the product, $D_{bO_2} \times c_{bO_2}$, 3.99×10^{-12} mol/cm*s.⁸² Oxygen mass transport parameters of similar magnitude were reported for a Tokuyama AS-4 ionomer film in 0.1 M KOH.¹⁴⁴ At 98% RH, and for a comparable IEC (2.1 meq/g), D_{bO_2} : 2.7×10^{-6} cm²/s; c_{bO_2} : 0.89×10^{-6} mol/cm³; and $D_{bO_2} \cdot c_{bO_2}$: 2.4×10^{-12} mol/cm*s are reported. Comparison of oxygen mass transport parameters reported here as well as previously, for Nafion 211, are presented for two similar values of relative humidity in Table 4.1.

Table 4.1. Oxygen mass transport parameters obtained through nonlinear curve fitting of the experimental data with the Shoup-Szabo equation

| Ionomer | RH | D_{bO_2} (cm ² /s) $\times 10^7$ | c_{bO_2} (mol/cm ³) $\times 10^6$ | $D_{bO_2} \cdot c_{bO_2}$ (mol/cm*s) $\times 10^{12}$ |
|--|-----|---|---|---|
| HMT-PMBI-OH ⁻ (2.1 meq/g) | 70% | 0.16 | 8.6 | 0.14 |
| | 90% | 11.0 | 1.2 | 1.3 |
| FAA-3 (2.0 meq/g) | 70% | 0.067 | 15.0 | 0.11 |
| | 90% | 0.11 | 3.4 | 0.37 |
| Nafion 211 (0.91 meq/g) from Chapter 3 | 70% | 0.68 | 3.7 | 0.25 |
| | 90% | 0.77 | 3.5 | 0.27 |

The discrepancy between mass transport parameters reported here and by those observed previously can be explained by the use of a) different polymer materials and b) different analytical models for parameter estimation. Gunasekara uses the Cottrell equation in the form that represents the first two terms in the short-time expansion by Aoki and Osteryoung and thus is subject to the restraint, $\frac{4D_{bO_2}t}{r^2} < 1$.¹⁵² For the reported electrode radius of 50 μm and 20 s duration of the experiment, the applicability range of the Cottrell equation is limited to D_{bO_2} values of $< 3.125 \times 10^{-7}$ cm²/s, which is much smaller than the fitted value of 4.29×10^{-6} , and may be out of the range of validity of the analytical model.

Comparing the values in Table 4.1, the oxygen diffusion coefficient for HMT-PMBI-OH⁻ 2.1 meq/g decreases 70 times more than Nafion 211 under similar conditions. The presented chronoamperometric measurements suggest a very strong dependence of oxygen diffusion on water

content for HMT-PMBI-OH⁻, which is consistent with the report by Khadke et al. on Tokuyama AS-4 ionomer films, in which it was suggested that ORR mass transport limitations result from a lack of reactant water, rather than the availability of oxygen.¹⁹

For comparative purposes, values for D_{bO_2} , c_{bO_2} , and $D_{bO_2} \cdot c_{bO_2}$ for all samples calculated using the geometric radius of the working electrode (5 μm) in the Shoup–Szabo equation, rather than the effective radius, are shown in Figure 4.13–Figure 4.15. The stark difference between approaches can be seen in the solubility comparison (Figure 4.14), where oxygen concentration is found to increase with decreasing IEC when using the geometric radius, which is counter to trends observed in literature where a higher water content afforded by higher IEC should cause oxygen solubility to decrease.^{62,153} In contrast, using the effective radius to determine oxygen concentration provides the expected, logical trend of decreasing oxygen concentration with increasing IEC/water content.

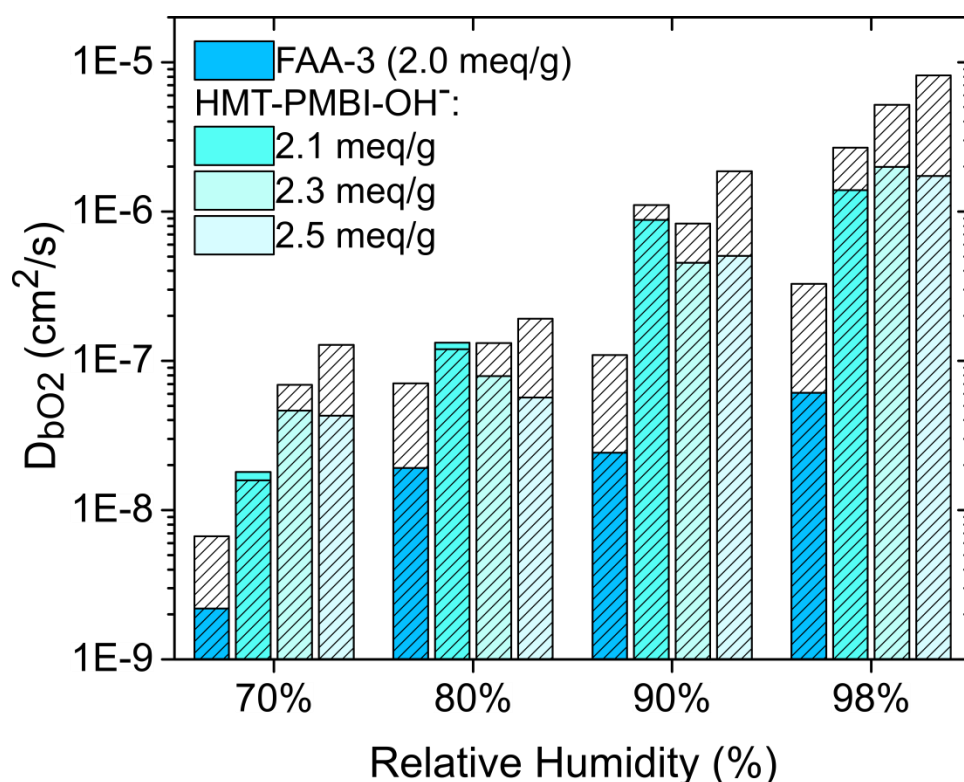


Figure 4.13. Oxygen diffusion coefficients obtained for HMT-PMBI-OH⁻ ionomer films and FAA-3 membranes by least squares fitting of the Shoup-Szabo equation versus RH, 60°C in air. Colored fill corresponds to geometric radius of 5 μm used in the Shoup-Szabo equation. Patterned fill corresponds to effective surface area-derived radius used in the Shoup-Szabo equation.

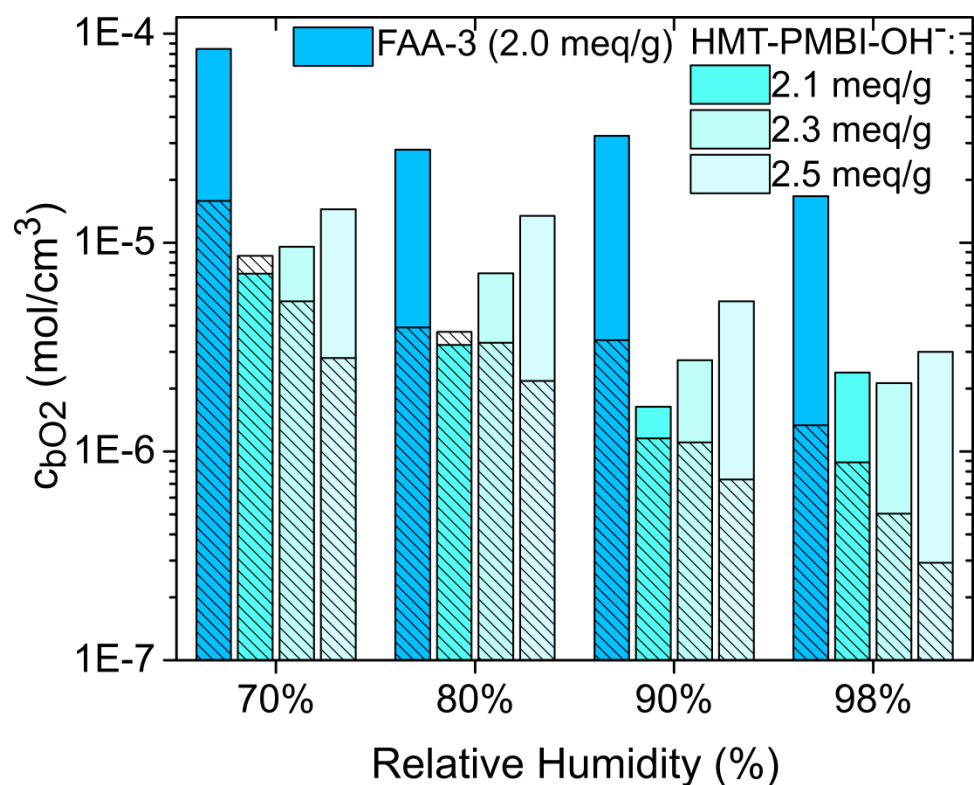


Figure 4.14. Oxygen solubility obtained for HMT-PMBI-OH⁻ ionomer films and FAA-3 membranes by least squares fitting of the Shoup-Szabo equation versus RH, 60°C in air. Colored fill corresponds to geometric radius of 5 μm used in the Shoup-Szabo equation. Patterned fill corresponds to effective surface area-derived radius used in the Shoup-Szabo equation.

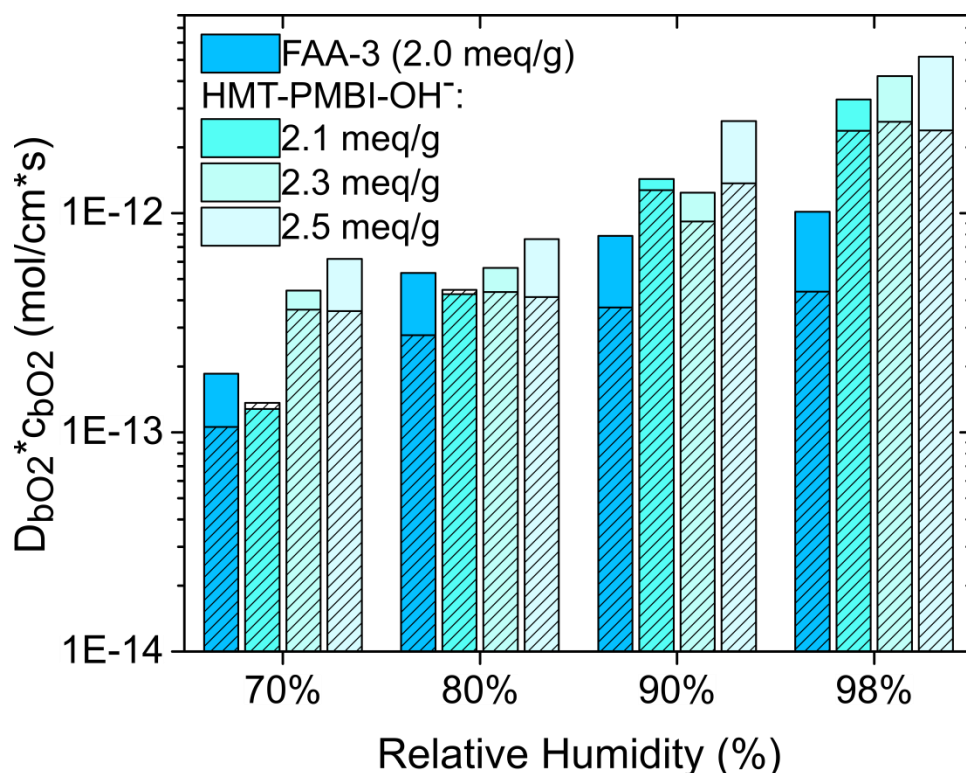


Figure 4.15. Oxygen permeability obtained for HMT-PMBI-OH⁻ ionomer films and FAA-3 membranes by least squares fitting of the Shoup-Szabo equation versus RH, 60°C in air. Colored fill corresponds to geometric radius of 5 μm used in the Shoup-Szabo equation. Patterned fill corresponds to effective surface area-derived radius used in the Shoup-Szabo equation.

As a means of comparison, Figure 4.16 shows normalized values for proton (Nafion 211) and hydroxide (2.5 meq/g HMT-PMBI) conductivities taken from literature versus relative humidity. Oxygen diffusion coefficients obtained using the Shoup-Szabo equation for Nafion 211 from Chapter 3 are compared with oxygen diffusion coefficients from Figure 4.10. Normalized to the 90% RH values, both proton and hydroxide conductivities decrease in a similar fashion from 90 to 70% RH. A stark difference in behaviour is noted in the oxygen diffusion coefficients when decreasing the RH from 90 to 70%, which the change in ionic conductivity does not explain. The drastic decrease in oxygen diffusion coefficient with relative humidity for the HMT-PMBI compared to the Nafion 211 is thus explained by the fact that water is a reactant in alkaline oxygen reduction and is therefore significantly impacted by a decrease in reactant concentration at the interface when relative humidity is decreased.

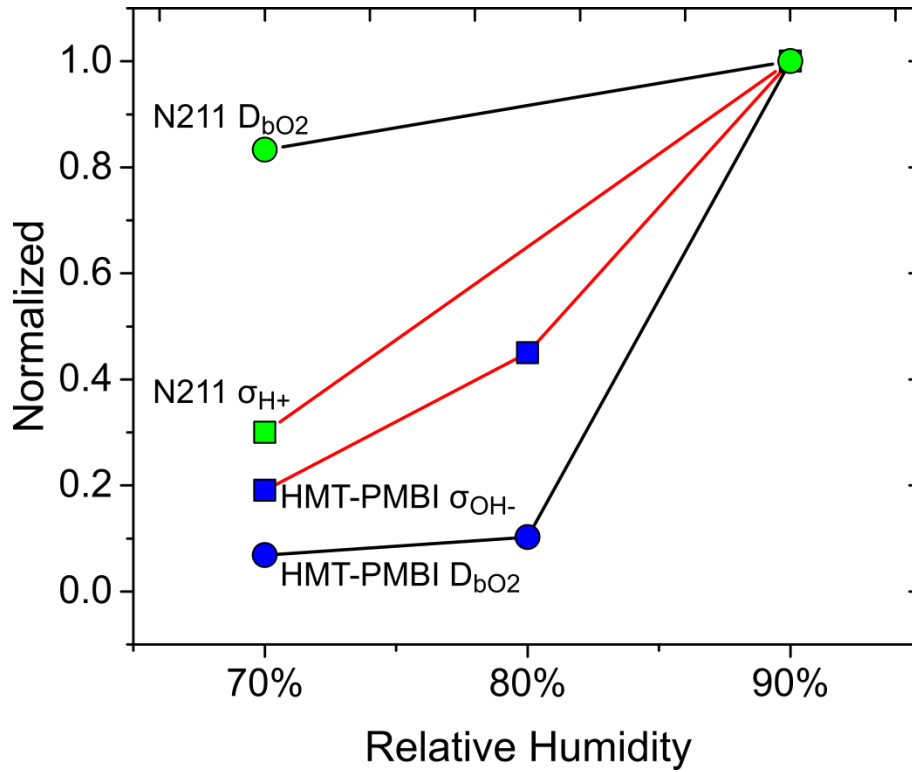


Figure 4.16. Diffusion coefficients and conductivities (proton and hydroxide) normalized to 90% RH values for Nafion 211 and 89% methylated (2.5 meq/g) HMT-PMBI versus relative humidity in air. Proton conductivity values taken from reference ²⁵, hydroxide conductivities taken from reference ¹⁴².

4.3.4. Numerical modeling

The results reported above were obtained using the Shoup-Szabo equation (Eqn. 3.1). A critical assumption made in utilizing this equation is that the ionomer is infinitely thick and hence the oxygen depletion region does not reach the surface of the film during the lifetime of the experiment.¹²⁶ It is also recognized that the Shoup-Szabo equation has a limited power of approximation of the radial diffusion, which are given by the second and subsequent terms of the short- and long-time expansions of the equation obtained by Aoki and Osteryoung.^{126,152} In order to examine the applicability of the Shoup-Szabo equation for these particular ionomer films, under these particular conditions, an axisymmetric, two-dimensional numerical model of the diffusion process in cylindrical coordinates was developed and solved in the open source Fuel Cell Simulation Toolbox (OpenFCST).¹⁵⁴ Fuller details of the model are provided in Appendix B.

Numerical modeling was performed for the HMT-PMBI- OH^- 2.1 meq/g IEC ionomer. As can be seen from Table B1, the diffusion length, L_D , estimated as $2\sqrt{5D_{bO_2}^{an}}$, is much smaller than the thickness of the ionomer in the 70% RH case for the experimental time interval of 5 s. The diffusion length is

close to the film thickness when the RH is 90% RH, and it is well beyond the film thickness at 98% RH, where the water content of the film and the corresponding diffusion coefficients are much larger. It is surmised that the analytically obtained results (using the Shoup-Szabo equation) are less valid in the latter two cases. Using the numerical simulation the errors associated with the assumptions made in deriving the Shoup-Szabo model were estimated.

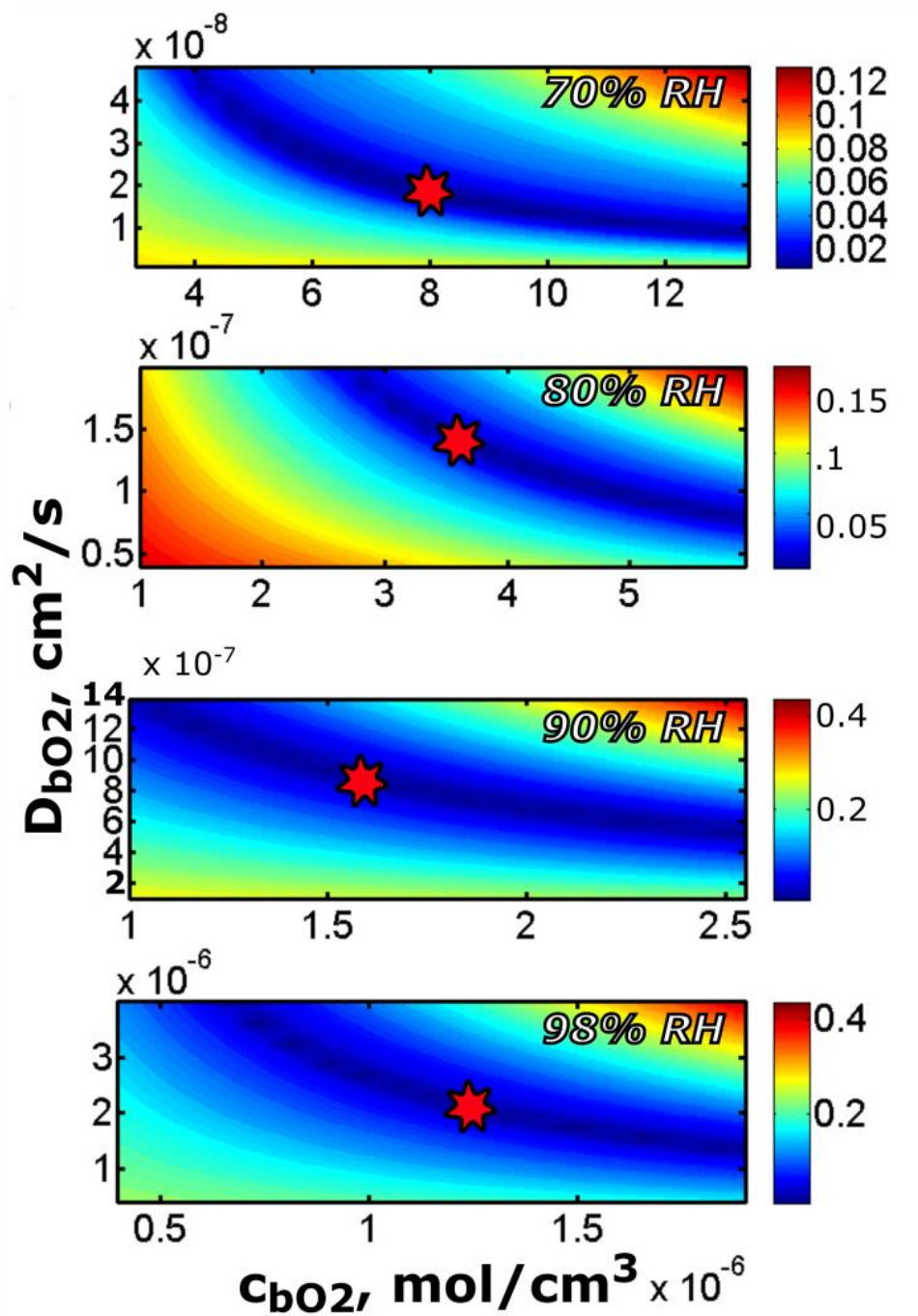


Figure 4.17. Contour plots for numerical fit normalized root mean square deviation (NRMSD) for 2.1 meq/g HMT-PMBI-OH⁻ at 60°C in air. Colour corresponds to % NRMSD, where the red stars correspond to minimum % NRMSD.

Table 4.2. Comparison of numerical and analytical results for 2.1 meq/g IEC HMT-PMBI-OH⁻ at 60°C

| RH, % | Exp. NRMSD, % | Num. NRMSD, % | $c_{bo_2}^{num},$ mol/cm ³ | $D_{bo_2}^{num},$ cm ² /s | $c_{bo_2} * D_{bo_2},$ mol/ cm * s | $t_{trunc},$ s | $t_{shift},$ s |
|-----------------------------------|------------------|------------------|--|---|---------------------------------------|-------------------|----------------|
| 70 | 0.71 | 0.95 | $7.950 * 10^{-6}$ | $1.850 * 10^{-8}$ | $1.471 * 10^{-13}$ | 0.165 | 0.150 |
| Difference from analytical fit, % | | | 8.6 | 14.6 | 7.5 | 0.01 | 0.43 |
| 80 | 0.37 | 0.53 | $3.600 * 10^{-6}$ | $1.408 * 10^{-7}$ | $5.069 * 10^{-13}$ | 0.162 | 0.138 |
| Difference from analytical fit, % | | | 3.8 | 14.9 | 11.7 | 3.04 | 1.35 |
| 90 | 0.53 | 0.69 | $1.588 * 10^{-6}$ | $8.700 * 10^{-7}$ | $1.382 * 10^{-12}$ | 0.165 | 0.140 |
| Difference from analytical fit, % | | | 27.2 | 26.9 | 7.6 | 13.4 | 10.1 |
| 98 | 0.73 | 1.08 | $1.240 * 10^{-6}$ | $2.110 * 10^{-6}$ | $2.616 * 10^{-12}$ | 0.179 | 0.162 |
| Difference from analytical fit, % | | | 28.5 | 27.0 | 9.0 | 17.9 | 12.2 |

Numerically obtained oxygen transport properties are shown in Table 4.2, and the values for D_{bO_2} , c_{bO_2} , and $D_{bO_2} \cdot c_{bO_2}$ are also plotted in Figure 4.10-4.12 as red points in order to visually compare them to analytically obtained values. Contour plots showing the associated NRMSD, including the solutions with minimum error, obtained from applying the numerical model on the current transients for 70% to 98% RH can be seen in Figure 4.17. The magnitude of change in D_{bO_2} , c_{bO_2} , and $D_{bO_2} \cdot c_{bO_2}$ observed as RH decreases for 2.1 meq/g HMT-PMBI-OH⁻ relates well to the analytically obtained results. Specifically, D_{bO_2} decreased by 114 times (compared to 170, analytically) while $D_{bO_2} \cdot c_{bO_2}$ decreased by 18 times (compared to 17, analytically) when the RH was lowered from 98% to 70%, and c_{bO_2} increased by 6 times (compared to 10, analytically). Results for the 80% RH case were the closest to analytically fitted values, exhibiting only a 3.8% difference in oxygen solubility and a 14.9% difference in oxygen diffusion coefficient. As the oxygen diffusion coefficient increases with increasing RH (and thus water content), the gas distribution in the domain is increasingly affected by its encroachment on the film's physical boundary, making conventional analytical models, such as Cottrell and Shoup-Szabo analyses, less accurate. The difference between the numerical and analytical solution, computed with respect to the numerical results, was 27.2% and 28.5% with respect to oxygen solubility at 90% and 98% RH, respectively; and 26.9% and 27.0%, respectively, for diffusivity. The product of oxygen solubility and oxygen diffusion coefficient, i.e., permeability, was found to be reasonably accurate (<12 % error) in all cases. The Shoup-Szabo equation fits obtained analytically were quite reasonable, with an NRMSD from experimental data of 0.53-0.73%; however, the Shoup-Szabo equation introduces a significant error in the computation of D_{bO_2} and c_{bO_2} independently due to the fact that the simplifying assumptions are not valid when the oxygen diffusion length reaches the film thickness during the experimental time scale. As an example, Figure 4.18 shows the dimensionless distribution of oxygen concentration along dimensionless axis, $x=0$, (coinciding with the central axis of the electrode or the axis of symmetry of the computational domain) at $t \cong 5$ s for different RH conditions. Coordinate $y=1$ represents the gas-ionomer interface, and a non-zero slope of concentration around that point at 90% and 98 % RH indicates the presence of a non-zero flux of oxygen diffusing into the domain. This effect is not taken into account by any conventional analytical model, be it the Cottrell or the Shoup-Szabo equation. It is also worth noting that the analytical relation used to estimate diffusion length in Table B1, $2\sqrt{D_{bO_2}t}$, does not provide sufficient insight into actual diffusion propagation as it clearly underestimates it. Therefore, when possible, the numerical model is recommended over the analytical approximations for the purpose of fitting the gas transport properties in ionomers in order to obtain accurate results.

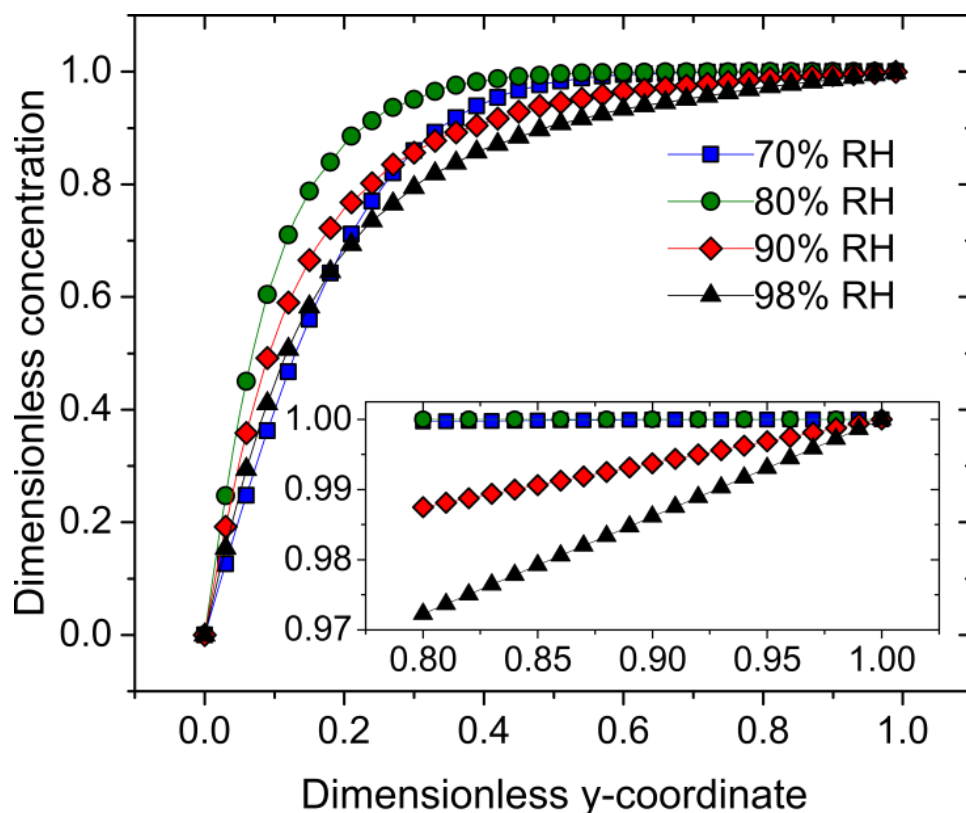


Figure 4.18. Dimensionless oxygen concentration (where a value of 1 represents bulk oxygen) distribution under the center of the electrode ($x=0$) versus dimensionless y -coordinate (film thickness normalized to gas-ionomer boundary) for 2.1 meq/g HMT-PMBI-OH⁻ for 70%, 90%, and 98% RH at 60°C, $t \cong 5s$. Inset: zoom showing slopes present at 90% and 98% RH which indicate oxygen flux at gas-ionomer boundary.

4.4. Conclusions

A novel anion exchange ionomer as well as a commercially available AAEM membrane of comparative thickness were investigated for ORR transport parameters using a 2-electrode solid state microelectrode electrochemical cell. It was discovered that the effective surface area of the working electrode decreased as relative humidity was reduced. The effective surface area was also lower for lower IEC membranes. In contrast, although FAA-3 possesses a lower IEC than the HMT-PMBI-OH⁻ films analyzed, a higher overall effective working electrode area was observed. All three effects correlated to the films water content. The effective surface areas approached that in aqueous KOH under conditions of high RH.

Oxygen mass transport parameters were calculated using least squares fitting of the Shoup-Szabo equation, where the oxygen diffusion coefficient was observed to decrease for all ionomer films as relative humidity and/or ion exchange capacity were reduced. The oxygen solubility, on the other hand, was observed to increase as either ion exchange capacity or relative humidity were reduced. The oxygen permeability decreased by over an order of magnitude when subjected to less than a 30% drop in RH at 60 °C.

The accuracy of the fits of the Shoup-Szabo equation for analysing oxygen mass transport in thin ionomer films was investigated by numerical modeling, which showed parity for oxygen permeability (between 7% and 12% accuracy). For accurate D_{bO_2} and c_{bO_2} estimation however, the numerical model is preferable over the Shoup-Szabo equation due to the simplifying assumptions needed to derive the model. The large decrease in D_{bO_2} observed when RH is lowered, coupled with the large decrease in current response at 70% RH compared to higher humidities, reinforces a primary limiting factor in anion exchange ionomer design, that the hydration of the membrane limits mass transport of reactants in the cathode catalyst layer.

Chapter 5. Conclusions and future work

5.1. Conclusions

In the presented work, oxygen mass transport parameters for proton and alkaline anion exchange ionomers were investigated using solid state electrochemical methods. The catalyst/ionomer interface was probed with platinum microelectrodes positioned at the ionomer interface in order to emulate ionomer coating catalyst agglomerates in the cathode catalyst layer. The ex-situ technique allowed for the investigation of oxygen transport characteristics under reduced relative humidity and elevated temperature.

In Chapter 2, a reversible time-dependence on oxygen mass transport parameters was elucidated during potential-step measurements with varying amounts of open circuit rest-time. For Nafion 117 membrane at 70% RH and 50 °C, a trend of mass transport parameters having a relationship with the previous measurement was observed. The electrochemical generation of small quantities (<nL) of liquid water at the platinum/ionomer interface at 70% RH was shown to increase oxygen permeability up to a plateau value over several successive measurements that each generated interfacial liquid water. The presented data suggests that the morphology of the polymer in contact with the platinum electrode changes in the presence of liquid water, to a state with a higher degree of hydrophilic channels at the ionomer/platinum interface compared to the vapour equilibrated state. This is supported by the fact that the oxygen diffusion coefficient, which is water-dependent, increased in the same fashion as the permeability, while the oxygen solubility, which is generally attributed to the hydrophobic phase, was not greatly affected. With greater relaxation time between water generation steps, the oxygen diffusion coefficient and oxygen permeability decreased to lower values, and was attributed to hydrophilic channels shrinking in size as available water at the surface decreases. While this effect was readily observed in extruded (i.e. Nafion 117) membranes, it was not readily reproducible in cast (i.e. Nafion 211) membranes. Analysis of repeated chronoamperometric measurements after an interfacial rest time of 5 minutes at open circuit potential in Nafion 211 and cast DE2020 films revealed markedly differing behaviours from the Nafion 117 study. Notably, for both

Nafion 211 and cast DE2020 there is little to no difference in the calculated oxygen diffusion coefficient, while a time dependency exists and becomes more pronounced as RH is reduced for calculated oxygen solubilities. The rate of morphological change resulting from the electrochemical generation of water may be too rapid for the present technique to measure in terms of mass transport parameters.

In Chapter 3, several experimental and analytical techniques were employed and developed toward the determination of oxygen mass transport parameters from 90-30% RH at 70°C. A two-electrode setup with pseudo-reference was deemed sufficient to use in a low hydration environment when compared to a conventional three-electrode cell, afforded by the use of a sufficiently small microelectrode. Sampled-current voltammetry was utilized at discrete times per RH in order to determine appropriate mass transport limiting potentials, as the appropriate values shifted to more negative overpotentials as relative humidity was decreased. A working electrode area correction obtained from hydrogen adsorption in cyclic voltammetry was employed in order to account for changes in the effective accessible conductive area of the electrode/electrolyte interface. The effective active surface area of the working electrode was observed to decrease as relative humidity was lowered in both Nafion 211 and DE2020 ionomer films in a similar fashion. Solid state chronoamperometry measurements at the Nafion 211/Pt or cast DE2020/Pt interface, analyzed by linear regression and non-linear curve fitting methods, indicate that the RH affects interfacial oxygen mass transport parameters. The oxygen diffusion coefficient was shown to decrease by as much as 24 times when decreasing from 90-30% RH, while oxygen solubility was shown to increase by a maximum of 9 times from 90-30% RH. The magnitude of change in the diffusion coefficient decreases more rapidly than the oxygen solubility increases, leading to an oxygen permeability that decreases by a factor of 3 from 90-30% RH.

In Chapter 4, an alkaline anion exchange ionomer, HMT-PMBI-OH⁻, as well as a comparative commercially available AAEM (FAA-3), were investigated for oxygen transport parameters using a 2-electrode solid state electrochemical cell. It was discovered that the effective surface area of the working electrode decreased as relative humidity was reduced, as well as when ion exchange capacity was lowered in the polymer through reduced degree of methylation on the backbone. On the contrary, although FAA3 has a lower IEC than the lowest methylated sample tested, a higher overall effective working electrode area was observed. In this investigation, the relative humidity was capped at 70% at 60°C as the lowest value. This was caused by a significant decrease in measured current (<1 nA)

attributed to a significant reliance on liquid water as reactant in basic ORR conditions that is not present in acidic PFSA ionomers.

The oxygen diffusion coefficient was observed to decrease by up to a factor of 100 when decreasing the relative humidity from 98-70% at 60°C in air for 82% methylated HMT-PMBI-OH⁻ ionomer. At most values of RH, as the degree of methylation was lowered and therefore IEC and water content lowered, the diffusion coefficient was observed to decrease while oxygen solubility increased, and overall oxygen permeability decreased. The drastic decrease in the oxygen diffusion coefficient, coupled with the large decrease in current response at 70% RH compared to higher humidities reinforces a primary limiting factor in anion exchange ionomer design, notable the necessity for high hydration during operating conditions to reduce mass transport losses. Further, there may be a coupled component of water transport within the reported oxygen mass transport parameters, where a more suitable descriptor may be for the entire oxygen reduction reaction (oxygen + water mass transport) rather than just for oxygen gas.

The lambda values for Nafion and HMT-PMBI-OH⁻ as relative humidity is lowered are similar enough to not fully explain the significant differences in oxygen mass transport parameters between polymer systems. This suggests that either there may be a significantly different oxygen transport mechanism for HMT-PMBI-OH⁻/Pt compared to Nafion/Pt, exacerbated by the fact that water is a reactant in alkaline ORR. As well, mixed (oxygen + water) transport parameters may be present, where water transport at reduced RH is significantly slower than oxygen gas.

To summarize, the electrochemical determination of oxygen mass transport parameters in less than fully hydrated systems is a dynamic process in the polymers studied herein. The amount of vapour and liquid water present at the electrochemical interface can have a significant effect on the resulting electrochemistry.

5.2. Future work

Based on the presented findings, it is suggested that thin ionomer films <100 nm should be investigated for their respective oxygen mass transport parameters. This would allow correlation between what is observed in bulk-scale membranes tested here (>10 µm) and what is present in the catalyst layer. For the investigation of thin films, nanoscale electrode arrays can be utilized to see if

there is an opportunity to probe true catalyst layer type thin films of ionomer, as the literature has recently revealed the contrary nature of confined thin ionomer films compared to bulk membranes. There are several challenges, notable the extremely small currents (pA and lower) to resolve, as well as the extremely short times in which the linear diffusion regime exists. These implications may prove to be too difficult to reasonably investigate real nanoscale properties electrochemically.

Further investigation into the effective surface area as humidity is lowered may be fruitful, especially if such an effect can be observed for nano-thin films of ionomer which is relevant to what may exist in a catalyst layer film. There are several methods of analysis such as with CO stripping voltammetry, which avoids the problems of uncertainty with hydrogen evolution overlap. Similarly, the work of Amatore on blocked electrode surfaces could provide an adequate treatment to describe the islands of conductive area more accurately than the aggregated island method used in this work.¹⁵⁵

Ideally, the methodology for thin ionomer films could be used to test the efficacy of ionomer candidates, where reactant mass transport is of paramount importance. If desired parameters (temperature and humidity) are set and measurements can be standardized for a wide variety of ionomer candidates, there is a potential to explain the differences in fuel cell operation in the context of reactant mass transport which can help in the development of future ionomers for maximizing gas permeability. Understanding and tailoring the permeability of oxygen in the ionomer in the cathode catalyst layer can lead to real world improvements in automotive fuel cells by increasing the power output at lower platinum loadings which translates to significantly lower costs.

Asking the “blue-sky” question of “what would the ideal cathode ionomer look like without restrictions?” may give insights for future directions in ionomer research. Specialized ionomer chemistries are presently being commercially investigated which are designed to increase oxygen permeability for the cathode catalyst layer. The introduction of a non-functionalized moiety such as a fluorinated cyclic group or linear chain creates void spaces for improved oxygen transport which has been claimed to significantly improve fuel cell performance even at typical mass transport-limiting currents.¹⁵⁶ A “dream” ionomer for the cathode catalyst layer, where reality need not apply, would be as thin and uniform as possible to reduce mass transport losses, while maintaining excellent proton and gas transport properties irrespective of environmental water content. A recent investigation in functionalizing the carbon support led to a more even distribution of ionomer which reduced oxygen mass transport resistance due to a more uniform ionomer thickness in the catalyst layer.¹⁵⁷

Zooming in on the ionomer structure, a balance between hydrophobic and hydrophilic domains would be ideal. Well-defined channels would have an optimum volumetric ratio between fast oxygen transport in hydrophilic channels and hydrophobic “oxygen sinks”, which readily supply oxygen to the hydrophilic channels. Judging from the results described in the chapters of this work, it would seem that some type of rigid structural scaffolding in place to keep the hydrophilic channel access open at the surface would lead to improved gas transport at lower relative humidities.

References

- (1) Grove, W. R. On Voltaic Series and Combination of Gases by Platinum. *Phil. Mag.* **1839**, 14, 127–130.
- (2) Bard, A. J.; Faulkner, L. R. *Electrochemical Methods: Fundamentals and Applications*; Wiley, 2000; Vol. 6.
- (3) Grove, W. R. On a Gaseous Voltaic Battery. *Philos. Mag.* **2012**, 92 (31), 3753–3756.
- (4) Mond, L.; Langer, C. A New Form of Gas Battery. *Proc R Soc London* **1889**, 46, 296–304.
- (5) Mench, M. *Fuel Cell Engines*; John Wiley & Sons, Inc, 2008.
- (6) Larminie, J.; Dicks, A. *Fuel Cell Systems Explained*; J. Wiley, 2003.
- (7) Zhang, J. *PEM Fuel Cell Electrocatalysts and Catalyst Layers*; Zhang, J., Ed.; Springer London: London, 2008.
- (8) Haynes, W. M. *CRC Handbook of Chemistry and Physics*; CRC Press, Inc., 2015.
- (9) Barbir, F. *PEM Fuel Cells: Theory and Practice*; New York: Elsevier Academic Press, 2005.
- (10) Hirschenhofer, J.; Stauffer, D.; Engleman, R.; Klett, M. Fuel Cell Handbook. **1998**, No. November.
- (11) Ju, H.; Wang, C. Y. Experimental Validation of a PEM Fuel Cell Model by Current Distribution Data. *J Electrochem Soc* **2004**, 151, A1954-60.
- (12) Eikerling, M.; Kulikovskiy, A. *Polymer Electrolyte Fuel Cells: Physical Principles of Materials and Operation*; CRC Press, Inc., 2015.
- (13) Behling, N. H. *Fuel Cells: Current Technology Challenges and Future Research Needs*; Elsevier, 2013.
- (14) Holdcroft, S. Fuel Cell Catalyst Layers: A Polymer Science Perspective. *Chem. Mater.* **2014**, 26 (1), 381–393.
- (15) Neyerlin, K. C.; Gu, W.; Jorne, J.; Clark, A.; Gasteiger, H. a.; Jr., A. C. Cathode Catalyst Utilization for the ORR in a PEMFC. *J. Electrochem. Soc.* **2007**, 154 (2), B279.

- (16) Varcoe, J. R.; Atanassov, P.; Dekel, D. R.; Herring, A. M.; Hickner, M. a.; Kohl, P. a.; Kucernak, A. R.; Mustain, W. E.; Nijmeijer, K.; Scott, K.; Xu, T.; Zhuang, L. Anion-Exchange Membranes in Electrochemical Energy Systems. *Energy Environ. Sci.* **2014**, 7 (10), 3135–3191.
- (17) Zhang, H. W.; Chen, D. Z.; Xianze, Y.; Yin, S. B. Anion-Exchange Membranes for Fuel Cells: Synthesis Strategies, Properties and Perspectives. *Fuel Cells* **2015**, No. 6, 761–780.
- (18) Merle, G.; Wessling, M.; Nijmeijer, K. Anion Exchange Membranes for Alkaline Fuel Cells: A Review. *J. Memb. Sci.* **2011**, 377 (1–2), 1–35.
- (19) Khadke, P. S.; Krewer, U. Performance Losses at H₂/O₂ Alkaline Membrane Fuel Cell. *Electrochem. commun.* **2015**, 51, 117–120.
- (20) Scherer, G. G. Polymer Membranes for Fuel Cells. *Berichte der Bunsengesellschaft für Phys. Chemie* **1990**, 94 (9), 1008–1014.
- (21) Mauritz, K. a; Moore, R. B. State of Understanding of Nafion. *Chem. Rev.* **2004**, 104 (10), 4535–4585.
- (22) Hoogers, G. *Fuel Cell Technology Handbook*; CRC Press, Inc., 2003.
- (23) Vielstich, W.; Lamm, A.; Gasteiger, H. A. (Hubert A.; Yokokawa, H. *Handbook of Fuel Cells : Fundamentals, Technology, and Applications*; Wiley, 2003.
- (24) Gebel, G. Structural Evolution of Water Swollen Perfluorosulfonated Ionomers from Dry Membrane to Solution. *Polymer (Guildf)*. **2000**, 41 (15), 5829–5838.
- (25) Peron, J.; Mani, A.; Zhao, X.; Edwards, D.; Adachi, M.; Soboleva, T.; Shi, Z.; Xie, Z.; Navessin, T.; Holdcroft, S. Properties of Nafion® NR-211 Membranes for PEMFCs. *J. Memb. Sci.* **2010**, 356 (1–2), 44–51.
- (26) Varcoe, J. R.; Slade, R. C. T. Prospects for Alkaline Anion-Exchange Membranes in Low Temperature Fuel Cells. *Fuel Cells* **2005**, 5 (2), 187–200.
- (27) Wang, J.; Wang, J.; Zhang, S. Synthesis and Characterization of Cross-Linked Poly(arylene Ether Ketone) Containing Pendant Quaternary Ammonium Groups for Anion-Exchange Membranes. *J. Memb. Sci.* **2012**, 415–416, 205–212.
- (28) Noonan, K. J. T.; Hugar, K. M.; Kostalik, H. a; Lobkovsky, E. B.; Abruña, H. D.; Coates, G. W. Phosphonium-Functionalized Polyethylene: A New Class of Base-Stable Alkaline Anion Exchange Membranes. *J. Am. Chem. Soc.* **2012**, 134 (44), 18161–18164.
- (29) Faraj, M.; Elia, E.; Boccia, M.; Filpi, A.; Pucci, A.; Ciardelli, F. New Anion Conducting Membranes Based on Functionalized Styrene-Butadiene-Styrene Triblock Copolymer for Fuel Cells Applications. *J. Polym. Sci. Part A Polym. Chem.* **2011**, 49 (15), 3437–3447.

- (30) Chen, D.; Hickner, M. A. Degradation of Imidazolium- and Quaternary Ammonium-Functionalized Poly(fluorenyl Ether Ketone Sulfone) Anion Exchange Membranes. *ACS Appl. Mater. Interfaces* **2012**, 4 (11), 5775–5781.
- (31) Kreuer, K.-D. *Fuel Cells: Selected Entries from the Encyclopedia of Sustainability Science and Technology*; Springer, 2013.
- (32) Thomas, O. D.; Soo, K. J. W. Y.; Peckham, T. J.; Kulkarni, M. P.; Holdcroft, S. A Stable Hydroxide-Conducting Polymer. *J. Am. Chem. Soc.* **2012**, 134 (26), 10753–10756.
- (33) Wright, A. G.; Holdcroft, S. Hydroxide-Stable Ionenenes. *ACS Macro Lett.* **2014**, 3 (5), 444–447.
- (34) Srinivasan, S.; Ticianelli, E. A.; Derouin, C. R.; Redondo, A. Advances in Solid Polymer Electrolyte Fuel Cell Technology with Low Platinum Loading Electrodes. *J. Power Sources* **1988**, 22 (3–4), 359–375.
- (35) Wilson, M. S.; Gottesfeld, S. Thin-Film Catalyst Layers for Polymer Electrolyte Fuel Cell Electrodes. *J. Appl. Electrochem.* **1992**, 22 (1), 1–7.
- (36) Wilson, M. S.; Gottesfeld, S. High Performance Catalyzed Membranes of Ultra-Low Pt Loadings for Polymer Electrolyte Fuel Cells. *J. Electrochem. Soc.* **1992**, 139 (2), L28.
- (37) Paddison, S. J.; Promislow, K. S. *Device and Materials Modeling in PEM Fuel Cells*; Paddison, S. J., Promislow, K. S., Eds.; Topics in Applied Physics; Springer New York: New York, NY, 2009; Vol. 113.
- (38) Eikerling, M.; Kornyshev, A.; Kucernak, A. Water in Polymer Electrolyte Fuel Cells: Friend or Foe? *Phys. Today* **2006**.
- (39) Malek, K.; Eikerling, M.; Wang, Q.; Navessin, T.; Liu, Z. Self-Organization in Catalyst Layers of Polymer Electrolyte Fuel Cells. *J. Phys. Chem. C* **2007**, 111 (36), 13627–13634.
- (40) Owejan, J. P.; Owejan, J. E.; Gu, W. Impact of Platinum Loading and Catalyst Layer Structure on PEMFC Performance. *J. Electrochem. Soc.* **2013**, 160 (8), F824–F833.
- (41) Hitchcock, A. P.; Berejnov, V.; Lee, V.; West, M.; Colbow, V.; Dutta, M.; Wessel, S. Carbon Corrosion of Proton Exchange Membrane Fuel Cell Catalyst Layers Studied by Scanning Transmission X-Ray Microscopy. *J. Power Sources* **2014**, 266, 66–78.
- (42) Lee, M.; Uchida, M.; Yano, H.; Tryk, D. A.; Uchida, H.; Watanabe, M. New Evaluation Method for the Effectiveness of Platinum/carbon Electrocatalysts under Operating Conditions. *Electrochim. Acta* **2010**, 55 (28), 8504–8512.
- (43) Sadeghi, E.; Putz, A.; Eikerling, M. Effects of Ionomer Coverage on Agglomerate Effectiveness in Catalyst Layers of Polymer Electrolyte Fuel Cells. *J. Solid State Electrochem.* **2014**, 18 (5), 1271–1279.

- (44) Liu, Y.; Murphy, M. W.; Baker, D. R.; Gu, W.; Ji, C.; Jorne, J.; Gasteiger, H. a. Proton Conduction and Oxygen Reduction Kinetics in PEM Fuel Cell Cathodes: Effects of Ionomer-to-Carbon Ratio and Relative Humidity. *J. Electrochem. Soc.* **2009**, *156* (8), B970.
- (45) Shinozaki, K.; Morimoto, Y.; Pivovar, B. S.; Kocha, S. S. Suppression of Oxygen Reduction Reaction Activity on Pt-Based Electrocatalysts from Ionomer Incorporation. *J. Power Sources* **2016**, *325* (2016), 745–751.
- (46) Park, Y.-C.; Tokiwa, H.; Kakinuma, K.; Watanabe, M.; Uchida, M. Effects of Carbon Supports on Pt Distribution, Ionomer Coverage and Cathode Performance for Polymer Electrolyte Fuel Cells. *J. Power Sources* **2016**, *315*, 179–191.
- (47) Bass, M.; Berman, A.; Singh, A.; Konovalov, O.; Freger, V. Surface Structure of Nafion in Vapor and Liquid. *J. Phys. Chem. B* **2010**, *114* (11), 3784–3790.
- (48) Benziger, J.; Bocarsly, A.; Cheah, M. J.; Majsztrik, P.; Satterfield, B.; Zhao, Q. Mechanical and Transport Properties of Nafion: Effects of Temperature and Water Activity; 2011; pp 85–113.
- (49) Neyerlin, K. C.; Gasteiger, H. a.; Mittelsteadt, C. K.; Jorne, J.; Gu, W. Effect of Relative Humidity on Oxygen Reduction Kinetics in a PEMFC. *J. Electrochem. Soc.* **2005**, *152* (6), A1073.
- (50) Eikerling, M. Water Management in Cathode Catalyst Layers of PEM Fuel Cells. *J. Electrochem. Soc.* **2006**, *153* (3), E58.
- (51) Modestino, M. a.; Paul, D. K.; Dishari, S.; Petrina, S. a.; Allen, F. I.; Hickner, M. a.; Karan, K.; Segalman, R. a.; Weber, A. Z. Self-Assembly and Transport Limitations in Confined Nafion Films. *Macromolecules* **2013**, *46* (3), 867–873.
- (52) Paul, D. K.; Karan, K. Conductivity and Wettability Changes of Ultrathin Nafion Films Subjected to Thermal Annealing and Liquid Water Exposure. *J. Phys. Chem. C* **2014**, *118* (4), 1828–1835.
- (53) Page, K. A.; Kusoglu, A.; Stafford, C. M.; Kim, S.; Kline, R. J.; Weber, A. Z. Confinement-Driven Increase in Ionomer Thin-Film Modulus. *Nano Lett.* **2014**, *14* (5), 2299–2304.
- (54) Kalisvaart, W. P.; Fritzsche, H.; Mérida, W. Water Uptake and Swelling Hysteresis in a Nafion Thin Film Measured with Neutron Reflectometry. *Langmuir* **2015**, *31* (19), 5416–5422.
- (55) Paul, D. K.; Karan, K. Conductivity and Wettability Changes of Ultrathin Nafion Films Subjected to Thermal Annealing and Liquid Water Exposure. *J. Phys. Chem. C* **2014**, *118* (4), 1828–1835.
- (56) Adachi, M.; Navessin, T.; Xie, Z.; Li, F. H.; Tanaka, S.; Holdcroft, S. Thickness Dependence of Water Permeation through Proton Exchange Membranes. *J. Memb. Sci.* **2010**, *364* (1–2), 183–193.
- (57) Duan, Q.; Wang, H.; Benziger, J. Transport of Liquid Water through Nafion Membranes. *J. Memb. Sci.* **2012**, *392–393*, 88–94.

- (58) Chen, C.; Pan, J.; Han, J.; Wang, Y.; Zhu, L.; Hickner, M. A.; Zhuang, L. Varying the Microphase Separation Patterns of Alkaline Polymer Electrolytes. *J. Mater. Chem. A* **2016**, 4 (11), 4071–4081.
- (59) Ogumi, Z.; Takehara, Z.; Yoshizawa, S. Gas Permeation in SPE Method I. Oxygen Permeation through Nafion and Neosepta. *J. Electrochem. Soc.* **1984**, 362 (1968), 769–773.
- (60) Ogumi, Z. Gas Permeation in SPE Method. *J. Electrochem. Soc.* **1985**, 132 (11), 2601.
- (61) Sakai, T.; Takenako, H.; Torikai, E. Gas Diffusion in the Dried and Hydrated Nafions. *J. Electrochem. Soc.* **1986**, 133 (1), 88.
- (62) Basura, V. I.; Chuy, C.; Beattie, P. D.; Holdcroft, S. Effect of Equivalent Weight on Electrochemical Mass Transport Properties of Oxygen in Proton Exchange Membranes Based on Sulfonated A, β , β -Trifluorostyrene (BAM®) and Sulfonated Styrene-(Ethylene-Butylene)-Styrene Triblock (DAIS-Analytical) Copolymers. *J. Electroanal. Chem.* **2001**, 501 (1–2), 77–88.
- (63) Parthasarathy, A. Pressure Dependence of the Oxygen Reduction Reaction at the Platinum Microelectrode/Nafion Interface: Electrode Kinetics and Mass Transport. *J. Electrochem. Soc.* **1992**, 139 (10), 2856.
- (64) Parthasarathy, A. Temperature Dependence of the Electrode Kinetics of Oxygen Reduction at the Platinum/Nafion® Interface—A Microelectrode Investigation. *J. Electrochem. Soc.* **1992**, 139 (9), 2530.
- (65) Beattie, P. D.; Basura, V. I.; Holdcroft, S. Temperature and Pressure Dependence of O₂ Reduction at Pt| Nafion® 117 and Pt| BAM® 407 Interfaces. *J. Electroanal. Chem.* **1999**, 468 (2), 180–192.
- (66) Basura, V.; Beattie, P.; Holdcroft, S. Solid-State Electrochemical Oxygen Reduction at Pt| Nafion® 117 and Pt| BAM3G™ 407 Interfaces. *J. Electroanal. Chem.* **1998**, 458 (1–2), 1–5.
- (67) Xie, Z.; Holdcroft, S. Polarization-Dependent Mass Transport Parameters for Orr in Perfluorosulfonic Acid Ionomer Membranes: An EIS Study Using Microelectrodes. *J. Electroanal. Chem.* **2004**, 568, 247–260.
- (68) Zhang, L.; Ma, C.; Mukerjee, S. Oxygen Reduction and Transport Characteristics at a Platinum and Alternative Proton Conducting Membrane Interface. *J. Electroanal. Chem.* **2004**, 568, 273–291.
- (69) Zhang, J.; Gasteiger, H. a.; Gu, W. Electrochemical Measurement of the Oxygen Permeation Rate through Polymer Electrolyte Membranes. *J. Electrochem. Soc.* **2013**, 160 (6), F616–F622.
- (70) Sakai, K.; Sato, K.; Mashio, T.; Ohma, A.; Yamaguchi, K.; Shinohara, K. Analysis of Reactant Gas Transport in Catalyst Layers; Effect of Pt-Loadings. In *ECS Transactions*; ECS, 2009; Vol. 25, pp 1193–1201.

- (71) Ohma, A.; Mashio, T.; Sato, K.; Iden, H.; Ono, Y.; Sakai, K.; Akizuki, K.; Takaichi, S.; Shinohara, K. Analysis of Proton Exchange Membrane Fuel Cell Catalyst Layers for Reduction of Platinum Loading at Nissan. *Electrochim. Acta* **2011**, 56 (28), 10832–10841.
- (72) Greszler, T. a.; Caulk, D.; Sinha, P. The Impact of Platinum Loading on Oxygen Transport Resistance. *J. Electrochem. Soc.* **2012**, 159 (12), F831–F840.
- (73) Tabe, Y.; Nishino, M.; Takamatsu, H.; Chikahisa, T. Effects of Cathode Catalyst Layer Structure and Properties Dominating Polymer Electrolyte Fuel Cell Performance. *J. Electrochem. Soc.* **2011**, 158 (10), B1246–B1254.
- (74) Kudo, K.; Suzuki, T.; Morimoto, Y. Analysis of Oxygen Dissolution Rate from Gas Phase into Nafion Surface and Development of an Agglomerate Model. In *ECS Transactions*; 2010; Vol. 33, pp 1495–1502.
- (75) Nonoyama, N.; Okazaki, S.; Weber, A. Z.; Ikogi, Y.; Yoshida, T. Analysis of Oxygen-Transport Diffusion Resistance in Proton-Exchange-Membrane Fuel Cells. *J. Electrochem. Soc.* **2011**, 158 (4), B416.
- (76) Weber, A. Z.; Kusoglu, A. Unexplained Transport Resistances for Low-Loaded Fuel-Cell Catalyst Layers. *J. Mater. Chem. A* **2014**, 2 (41), 17207–17211.
- (77) Ono, Y.; Mashio, T.; Takaichi, S.; Ohma, A.; Kanesaka, H.; Shinohara, K. The Analysis of Performance Loss with Low Platinum Loaded Cathode Catalyst Layers. In *ECS Transactions*; The Electrochemical Society, 2010; Vol. 28, pp 69–78.
- (78) Mashio, T.; Ohma, A.; Yamamoto, S.; Shinohara, K. Analysis of Reactant Gas Transport in a Catalyst Layer. *ECS Trans.* **2007**, 11 (1), 529–540.
- (79) Nouri-Khorasani, A.; Malek, K.; Malek, A.; Mashio, T.; Wilkinson, D. P.; Eikerling, M. H. Molecular Modeling of the Proton Density Distribution in a Water-Filled Slab-like Nanopore Bounded by Pt Oxide and Ionomer. *Catal. Today* **2016**, 262 (2016), 133–140.
- (80) Kudo, K.; Jinnouchi, R.; Morimoto, Y. Humidity and Temperature Dependences of Oxygen Transport Resistance of Nafion Thin Film on Platinum Electrode. *Electrochim. Acta* **2016**, 209 (2016), 682–690.
- (81) Jinnouchi, R.; Kudo, K.; Kitano, N.; Morimoto, Y. Molecular Dynamics Simulations on O₂ Permeation through Nafion Ionomer on Platinum Surface. *Electrochim. Acta* **2016**, 188 (2016), 767–776.
- (82) Gunasekara, I.; Lee, M.; Abbott, D.; Mukerjee, S. Mass Transport and Oxygen Reduction Kinetics at an Anion Exchange Membrane Interface: Microelectrode Studies on Effect of Carbonate Exchange. *ECS Electrochem. Lett.* **2012**, 1 (2), F16–F19.
- (83) Giacinti Baschetti, M.; Minelli, M.; Catalano, J.; Sarti, G. C. Gas Permeation in Perfluorosulfonated Membranes: Influence of Temperature and Relative Humidity. *Int. J.*

Hydrogen Energy **2013**, 38 (27), 11973–11982.

- (84) Wood, D. L.; Chlistunoff, J.; Majewski, J.; Borup, R. L. Nafion Structural Phenomena at Platinum and Carbon Interfaces. *J. Am. Chem. Soc.* **2009**, 131 (50), 18096–18104.
- (85) Ono, Y.; Mashio, T.; Takaichi, S.; Ohma, A. The Analysis of Performance Loss with Low Platinum Loaded Cathode Catalyst Layers. *ECS ...* **2010**, 28 (27), 69–78.
- (86) Isegawa, K.; Nagami, T.; Jomori, S.; Yoshida, M.; Kondoh, H. In Situ S-K XANES Study of Polymer Electrolyte Fuel Cells: Changes in the Chemical States of Sulfonic Groups Depending on Humidity. *Phys. Chem. Chem. Phys.* **2016**, 18 (36), 25183–25190.
- (87) Liu, H.; Epting, W. K.; Litster, S. Gas Transport Resistance in Polymer Electrolyte Thin Films on Oxygen Reduction Reaction Catalysts. *Langmuir* **2015**, 31 (36), 9853–9858.
- (88) Masuda, T.; Sonsudin, F.; Singh, P. R.; Naohara, H.; Uosaki, K. Potential-Dependent Adsorption and Desorption of Perfluorosulfonated Ionomer on a Platinum Electrode Surface Probed by Electrochemical Quartz Crystal Microbalance and Atomic Force Microscopy. *J. Phys. Chem. C* **2013**, 117 (30), 15704–15709.
- (89) Ticianelli, E. A. Methods to Advance Technology of Proton Exchange Membrane Fuel Cells. *J. Electrochem. Soc.* **1988**, 135 (9), 2209.
- (90) Lee, S.; Mukerjee, S.; McBreen, J.; Rho, Y.; Kho, Y. T.; Lee, T. H. Effects of Nafion Impregnation on Performances of PEMFC Electrodes. *Electrochim. Acta* **1998**, 43 (24), 3693–3701.
- (91) Daly, K. B.; Benziger, J. B.; Panagiotopoulos, A. Z.; Debenedetti, P. G. Molecular Dynamics Simulations of Water Permeation across Nafion Membrane Interfaces. *J. Phys. Chem. B* **2014**, 118 (29), 8798–8807.
- (92) Bass, M.; Berman, A.; Singh, A.; Konovalov, O.; Freger, V. Surface-Induced Micelle Orientation in Nafion Films. *Macromolecules* **2011**, 44 (8), 2893–2899.
- (93) Kusoglu, A.; Kushner, D.; Paul, D. K.; Karan, K.; Hickner, M. a.; Weber, A. Z. Impact of Substrate and Processing on Confinement of Nafion Thin Films. *Adv. Funct. Mater.* **2014**, 24 (30), 4763–4774.
- (94) Kusoglu, A.; Modestino, M. a.; Hexemer, A.; Segalman, R. a.; Weber, A. Z. Subsecond Morphological Changes in Nafion during Water Uptake Detected by Small-Angle X-Ray Scattering. *ACS Macro Lett.* **2012**, 1 (1), 33–36.
- (95) Kusoglu, A.; Savagatrup, S.; Clark, K. T.; Weber, A. Z. Role of Mechanical Factors in Controlling the Structure–Function Relationship of PFSA Ionomers. *Macromolecules* **2012**, 45 (18), 7467–7476.
- (96) Tang, J.; Yuan, W.; Zhang, J.; Li, H.; Zhang, Y. Evidence for a Crystallite-Rich Skin on

Perfluorosulfonate Ionomer Membranes. *RSC Adv.* **2013**, 3 (23), 8947.

- (97) Alberti, G.; Narducci, R.; Sganappa, M. Effects of Hydrothermal/thermal Treatments on the Water-Uptake of Nafion Membranes and Relations with Changes of Conformation, Counter-Elastic Force and Tensile Modulus of the Matrix. *J. Power Sources* **2008**, 178 (2), 575–583.
- (98) Gebel, G.; Lyonard, S.; Mendil-Jakani, H.; Morin, A. The Kinetics of Water Sorption in Nafion Membranes: A Small-Angle Neutron Scattering Study. *J. Phys. Condens. Matter* **2011**, 23 (23), 234107.
- (99) Fumagalli, M.; Lyonard, S.; Prajapati, G.; Berrod, Q.; Porcar, L.; Guillermo, A.; Gebel, G. Fast Water Diffusion and Long-Term Polymer Reorganization during Nafion Membrane Hydration Evidenced by Time-Resolved Small-Angle Neutron Scattering. *J. Phys. Chem. B* **2015**, 119 (23), 7068–7076.
- (100) Patankar, K. A.; Dillard, D. A.; Case, S. W.; Ellis, M. W.; Lai, Y.-H.; Budinski, M. K.; Gittleman, C. S. Hygrothermal Characterization of the Viscoelastic Properties of Gore-Select® 57 Proton Exchange Membrane. *Mech. Time-Dependent Mater.* **2008**, 12 (3), 221–236.
- (101) Kusoglu, A.; Weber, A. Z. New Insights into Perfluorinated Sulfonic-Acid Ionomers. *Chem. Rev.* **2017**, 117 (3), 987–1104.
- (102) Zoski, C. G. *Handbook of Electrochemistry*; Elsevier, 2007.
- (103) Subramanian, N. P.; Greszler, T. a.; Zhang, J.; Gu, W.; Makharia, R. Pt-Oxide Coverage-Dependent Oxygen Reduction Reaction (ORR) Kinetics. *J. Electrochem. Soc.* **2012**, 159 (5), B531.
- (104) Trasatti, S.; Petrii, O. A. Real Surface Area Measurements in Electrochemistry. *Journal of Electroanalytical Chemistry*. 1992, pp 353–376.
- (105) Cottrell, F. G. Der Reststrom Bei Galvanischer Polarisierung, Betrachtet Als Ein Diffusionsproblem. *Z. Phys. Chem.* **1902**, 42, 385–431.
- (106) Saito, Y. No Title. *Rev. Polarogr. Jpn.* **1968**, 15, 177.
- (107) Winlove, C. P.; Parker, K. H.; Oxenham, R. K. C. The Measurement of Oxygen Diffusivity and Concentration by Chronoamperometry Using Microelectrodes. *J. Electroanal. Chem. Interfacial Electrochem.* **1984**, 170 (1–2), 293–304.
- (108) Giner, J. A Practical Reference Electrode. *J. Electrochem. Soc.* **1964**, 111 (3), 376.
- (109) Cherevko, S.; Topalov, A. a.; Zeradjanin, A. R.; Keeley, G. P.; Mayrhofer, K. J. J. Temperature-Dependent Dissolution of Polycrystalline Platinum in Sulfuric Acid Electrolyte. *Electrocatalysis* **2014**, 5 (3), 235–240.

- (110) Jiang, J.; Kucernak, A. Investigations of Fuel Cell Reactions at the Composite Microelectrode|solid Polymer Electrolyte Interface. I. Hydrogen Oxidation at the Nanostructured Pt|Nafion® Membrane Interface. *J. Electroanal. Chem.* **2004**, 567 (1), 123–137.
- (111) Hiesgen, R.; Helmly, S.; Galm, I.; Morawietz, T.; Handl, M.; Friedrich, K. A. Microscopic Analysis of Current and Mechanical Properties of Nafion® Studied by Atomic Force Microscopy. *Membranes (Basel)*. **2012**, 2 (4), 783–803.
- (112) James, P. J.; Elliott, J. A.; McMaster, T. J.; Newton, J. M.; Elliott, A. M. S.; Hanna, S.; Miles, M. J. Hydration of Nafion® Studied by AFM and X-Ray Scattering. *J. Mater. Sci.* **2000**, 35 (20), 5111–5119.
- (113) Van Nguyen, T.; Nguyen, M. V.; Lin, G.; Rao, N.; Xie, X.; Zhu, D.-M. Characterization of Surface Ionic Activity of Proton Conductive Membranes by Conductive Atomic Force Microscopy. *Electrochem. Solid-State Lett.* **2006**, 9 (2), A88–A91.
- (114) Hiesgen, R.; Helmly, S.; Morawietz, T.; Yuan, X.-Z.; Wang, H.; Friedrich, K. A. Atomic Force Microscopy Studies of Conductive Nanostructures in Solid Polymer Electrolytes. *Electrochim. Acta* **2013**, 110, 292–305.
- (115) Hiesgen, R.; Morawietz, T.; Handl, M.; Corasaniti, M.; Friedrich, K. A. Insight into the Structure and Nanoscale Conductivity of Fluorinated Ionomer Membranes. *J. Electrochem. Soc.* **2014**, 161 (12), F1214–F1223.
- (116) Economou, N. J.; Barnes, A. M.; Wheat, A. J.; Schaberg, M. S.; Hamrock, S. J.; Buratto, S. K. Investigation of Humidity Dependent Surface Morphology and Proton Conduction in Multi-Acid Side Chain Membranes by Conductive Probe Atomic Force Microscopy. *J. Phys. Chem. B* **2015**, 119 (44), 14280–14287.
- (117) Aleksandrova, E.; Hiesgen, R.; Eberhard, D.; Friedrich, K. A.; Kaz, T.; Roduner, E. Proton Conductivity Study of a Fuel Cell Membrane with Nanoscale Resolution. *ChemPhysChem* **2007**, 8 (4), 519–522.
- (118) He, Q.; Kusoglu, A.; Lucas, I. T.; Clark, K.; Weber, A. Z.; Kostecki, R. Correlating Humidity-Dependent Ionically Conductive Surface Area with Transport Phenomena in Proton-Exchange Membranes. *J. Phys. Chem. B* **2011**, 115 (40), 11650–11657.
- (119) Economou, N. J.; O'Dea, J. R.; McConaughy, T. B.; Buratto, S. K. Morphological Differences in Short Side Chain and Long Side Chain Perfluorosulfonic Acid Proton Exchange Membranes at Low and High Water Contents. *RSC Adv.* **2013**, 3 (42), 19525.
- (120) Kreuer, K.-D. The Role of Internal Pressure for the Hydration and Transport Properties of Ionomers and Polyelectrolytes. *Solid State Ionics* **2013**, 252, 93–101.
- (121) He, Q.; Kusoglu, A.; Lucas, I. T.; Clark, K.; Weber, A. Z.; Kostecki, R. Correlating Humidity-Dependent Ionically Conductive Surface Area with Transport Phenomena in Proton-Exchange Membranes. *J. Phys. Chem. B* **2011**, 115 (40), 11650–11657.

- (122) Chlistunoff, J. Oxygen Permeability of Cast Ionomer Films from Chronoamperometry on Microelectrodes. *J. Power Sources* **2014**, *245*, 203–207.
- (123) Wang, J. X.; Zhang, J.; Adzic, R. R. Double-Trap Kinetic Equation for the Oxygen Reduction Reaction on Pt(111) in Acidic Media. *J. Phys. Chem. A* **2007**, *111* (49), 12702–12710.
- (124) Chlistunoff, J.; Uribe, F.; Pivovar, B. Oxygen Reduction at the Pt/Recast-Nafion Film Interface. Effect of the Polymer Equivalent Weight. In *ECS Transactions*; ECS, 2007; Vol. 2, pp 37–46.
- (125) Gileadi, E. *Physical Electrochemistry: Fundamentals, Techniques and Applications*; Wiley-VCH, 2011.
- (126) Shoup, D.; Szabo, A. Chronoamperometric Current at Finite Disk Electrodes. *J. Electroanal. Chem. Interfacial Electrochem.* **1982**, *140* (2), 237–245.
- (127) Xiong, L.; Aldous, L.; Henstridge, M. C.; Compton, R. G. Investigation of the Optimal Transient Times for Chronoamperometric Analysis of Diffusion Coefficients and Concentrations in Non-Aqueous Solvents and Ionic Liquids. *Anal. Methods* **2012**, *4* (2), 371–376.
- (128) Basha, C. A.; Rajendran, L. Theories of Ultramicrodisc Electrodes: Review Article. *Int. J. Electrochem. Sci.* **2006**, *1* (6), 268–282.
- (129) Mahon, P. J.; Oldham, K. B. The Transient Current at the Disk Electrode under Diffusion Control: A New Determination by the Cope-Tallman Method. *Electrochim. Acta* **2004**, *49*, 5041–5048.
- (130) Mahon, P. J.; Oldham, K. B. Diffusion-Controlled Chronoamperometry at a Disk Electrode. *Anal. Chem.* **2005**, *77* (18), 6100–6101.
- (131) Gode, P.; Lindbergh, G.; Sundholm, G. In-Situ Measurements of Gas Permeability in Fuel Cell Membranes Using a Cylindrical Microelectrode. *J. Electroanal. Chem.* **2002**, *518* (2), 115–122.
- (132) Kodama, K.; Jinnouchi, R.; Suzuki, T.; Murata, H.; Hatanaka, T.; Morimoto, Y. Increase in Adsorptivity of Sulfonate Anions on Pt (111) Surface with Drying of Ionomer. *Electrochem. commun.* **2013**, *36*, 26–28.
- (133) Lindström, R. W.; Kortsdottir, K.; Wesselmark, M.; Oyarce, A.; Lagergren, C.; Lindbergh, G. Active Area Determination of Porous Pt Electrodes Used in Polymer Electrolyte Fuel Cells: Temperature and Humidity Effects. *J. Electrochem. Soc.* **2010**, *157* (12), B1795.
- (134) Iden, H.; Ohma, A. An in Situ Technique for Analyzing Ionomer Coverage in Catalyst Layers. *J. Electroanal. Chem.* **2013**, *693*, 34–41.
- (135) Sleightholme, A. E. S.; Kucernak, A. An Anomalous Peak Observed in the Electrochemistry of the Platinum/perfluorosulfonic Acid Membrane Interface. *Electrochim. Acta* **2011**, *56* (11), 4396–4402.

- (136) Catalano, J.; Myezwa, T.; De Angelis, M. G.; Baschetti, M. G.; Sarti, G. C. The Effect of Relative Humidity on the Gas Permeability and Swelling in PFSI Membranes. *Int. J. Hydrogen Energy* **2012**, 37 (7), 6308–6316.
- (137) Iden, H.; Ohma, A.; Shinohara, K. Analysis of Proton Transport in Pseudo Catalyst Layers. *Journal of The Electrochemical Society*. 2009, p B1078.
- (138) Antolini, E.; Gonzalez, E. R. Alkaline Direct Alcohol Fuel Cells. *J. Power Sources* **2010**, 195 (11), 3431–3450.
- (139) Markovic, N.; Gasteiger, H.; Ross, P. N.; Berkeley, L.; Division, M. S. Kinetics of Oxygen Reduction on Pt (Hkl) Electrodes: Implications for the Crystallite Size Effect with Supported Pt Electrocatalysts. *J. Electrochem. Soc* **1997**, 144 (5), 1591–1597.
- (140) Henkensmeier, D.; Kim, H.-J.; Lee, H.-J.; Lee, D. H.; Oh, I.-H.; Hong, S.-A.; Nam, S.-W.; Lim, T.-H. Polybenzimidazolium-Based Solid Electrolytes. *Macromol. Mater. Eng.* **2011**, 296 (10), 899–908.
- (141) Thomas, O. D.; Soo, K. J. W. Y.; Peckham, T. J.; Kulkarni, M. P.; Holdcroft, S. Anion Conducting Poly(dialkyl Benzimidazolium) Salts. *Polym. Chem.* **2011**, 2 (8), 1641.
- (142) Wright, A. G.; Fan, J.; Britton, B.; Weissbach, T.; Lee, H.-F.; Kitching, E. A.; Peckham, T. J.; Holdcroft, S. Hexamethyl-P-Terphenyl Poly(benzimidazolium): A Universal Hydroxide-Conducting Polymer for Energy Conversion Devices. *Energy Environ. Sci.* **2016**, 9 (6), 2130–2142.
- (143) Wright, A. G.; Weissbach, T.; Holdcroft, S. Poly(phenylene) and M-Terphenyl as Powerful Protecting Groups for the Preparation of Stable Organic Hydroxides. *Angew. Chemie - Int. Ed.* **2016**, 55 (15), 4818–4821.
- (144) Khadke, P. S.; Krewer, U. Mass-Transport Characteristics of Oxygen at Pt/Anion Exchange Ionomer Interface. *J. Phys. Chem. C* **2014**, 118 (21), 11215–11223.
- (145) Chlistunoff, J.; Uribe, F.; Pivovar, B. Oxygen Reduction at the Pt/Recast-Nafion Film Interface at Different Temperatures and Relative Humidities. In *ECS Transactions*; ECS, 2006; Vol. 1, pp 137–146.
- (146) Carmo, M.; Doubek, G.; Sekol, R. C.; Linardi, M.; Taylor, A. D. Development and Electrochemical Studies of Membrane Electrode Assemblies for Polymer Electrolyte Alkaline Fuel Cells Using FAA Membrane and Ionomer. *J. Power Sources* **2013**, 230, 169–175.
- (147) Britton, B.; Holdcroft, S. The Control and Effect of Pore Size Distribution in AEMFC Catalyst Layers. *J. Electrochem. Soc.* **2016**, 163 (5), F353–F358.
- (148) Adams, L. A.; Poynton, S. D.; Tamain, C.; Slade, R. C. T.; Varcoe, J. R. A Carbon Dioxide Tolerant Aqueous-Electrolyte-Free Anion-Exchange Membrane Alkaline Fuel Cell. *ChemSusChem* **2008**, 1 (1–2), 79–81.

- (149) Ahuja, A. K.; Behrend, M. R.; Whalen, J. J.; Humayun, M. S.; Weiland, J. D. The Dependence of Spectral Impedance on Disc Microelectrode Radius. *IEEE Trans. Biomed. Eng.* **2008**, 55 (4), 1457–1460.
- (150) Chen, D.; Tao, Q.; Liao, L. W.; Liu, S. X.; Chen, Y. X.; Ye, S. Determining the Active Surface Area for Various Platinum Electrodes. *Electrocatalysis* **2011**, 2 (3), 207–219.
- (151) Weidner, J. W. Effect of Ohmic, Mass-Transfer, and Kinetic Resistances on Linear-Sweep Voltammetry in a Cylindrical-Pore Electrode. *J. Electrochem. Soc.* **1991**, 138 (9), 2514.
- (152) Aoki, K.; Osteryoung, J. Diffusion-Controlled Current at the Stationary Finite Disk Electrode. *J. Electroanal. Chem. Interfacial Electrochem.* **1981**, 122, 19–35.
- (153) Lee, K.; Ishihara, A.; Mitsushima, S.; Kamiya, N.; Ota, K. Effect of Recast Temperature on Diffusion and Dissolution of Oxygen and Morphological Properties in Recast Nafion. *J. Electrochem. Soc.* **2004**, 151 (4), A639.
- (154) Secanell, M.; Putz, A.; Wardlaw, P.; Zingan, V.; Bhaiya, M.; Moore, M.; Zhou, J.; Balen, C.; Domican, K. OpenFCST: An Open-Source Mathematical Modelling Software for Polymer Electrolyte Fuel Cells. *ECS Trans.* **2014**, 64 (3), 655–680.
- (155) Sliusarenko, O.; Oleinick, A.; Svir, I.; Amatore, C. Development and Validation of an Analytical Model for Predicting Chronoamperometric Responses of Random Arrays of Micro- and Nanodisk Electrodes. *ChemElectroChem* **2015**, 2 (9), 1279–1291.
- (156) Ionomer Having High Oxygen Permeability. CA2949641 A1, 2015.
- (157) Orfanidi, A.; Madkikar, P.; El-Sayed, H. A.; Harzer, G. S.; Kratky, T.; Gasteiger, H. A. The Key to High Performance Low Pt Loaded Electrodes. *J. Electrochem. Soc.* **2017**, 164 (4), 418–426.
- (158) Myland, J. C.; Oldham, K. B. Uncompensated Resistance. 1. The Effect of Cell Geometry. *Anal Chem* **2000**, 72 (17), 3972–3980.
- (159) Kosakian, A.; Secanell, M.; Novitski, D.; Holdcroft, S. Numerical Estimation of Oxygen Transport Properties in Thin Polymer Membranes. *Proc. Can. Soc. Mech. Eng. Int. Congr.* **2016**, 3–7.
- (160) Suzuki, T.; Kudo, K.; Morimoto, Y. Model for Investigation of Oxygen Transport Limitation in a Polymer Electrolyte Fuel Cell. *J. Power Sources* **2013**, 222 (2013), 379–389.
- (161) Farag, I.; Havasi, G.; Zlatev, Z. Efficient Implementation of Stable Richardson Extrapolation Algorithms. *Comput. Math. with Appl.* **2010**, 60 (8), 2309–2325.

Appendix A.

Determination of charging constant

An approximation for cell resistance valid for microelectrodes is given by

$$RI_{steady\ state} = \frac{nFDc_b}{\kappa}$$

and is independent of the working electrode dimensions provided that the counter electrode is much larger.¹⁵⁸ From this, the resistance using permeabilities (Dc_b) can be approximated for hydrogen from Gode et al. under similar conditions (60°C rather than 70°C).¹³¹ Proton conductivities for Nafion 211 are taken from Peron et al., and are used as specific conductance (κ).²⁵ The steady state current was 0.1 nA from the electrode setup, and n is 1. The resulting approximated resistances are shown in Figure A1, and show an increase (generally) in resistance as relative humidity is decreased. Although the uncompensated resistance is on the order of hundreds of k Ω , what matters most for these current transient measurements is the charging time constant given by:

$$\tau = C_{dl}R_u$$

Where 5τ is generally considered sufficient time before contributions from non-Faradaic charging can be neglected and the current response can be considered Faradaic.² The double layer capacitance is taken from the double layer charging region from the cyclic voltammograms given in the text as Figure 3.4, and is on the order of nF . As can be seen from Figure A1, a wait time of about 2 milliseconds is required before measurements can be considered reasonably devoid of the effects of resistance and capacitance, that the working electrode surface potential has changed and the Faradaic reaction (ORR) occurs. Although it appears that there is substantial contribution from resistance (or more so, capacitive charging) from the presented CVs, the use of microelectrodes help to reduce the impact of resistive media. Similarly, the iR drop can be calculated from the resistance and currents of measurements (order of nA), and therefore the uncertainty is on the order of single millivolts, which is practically negligible.

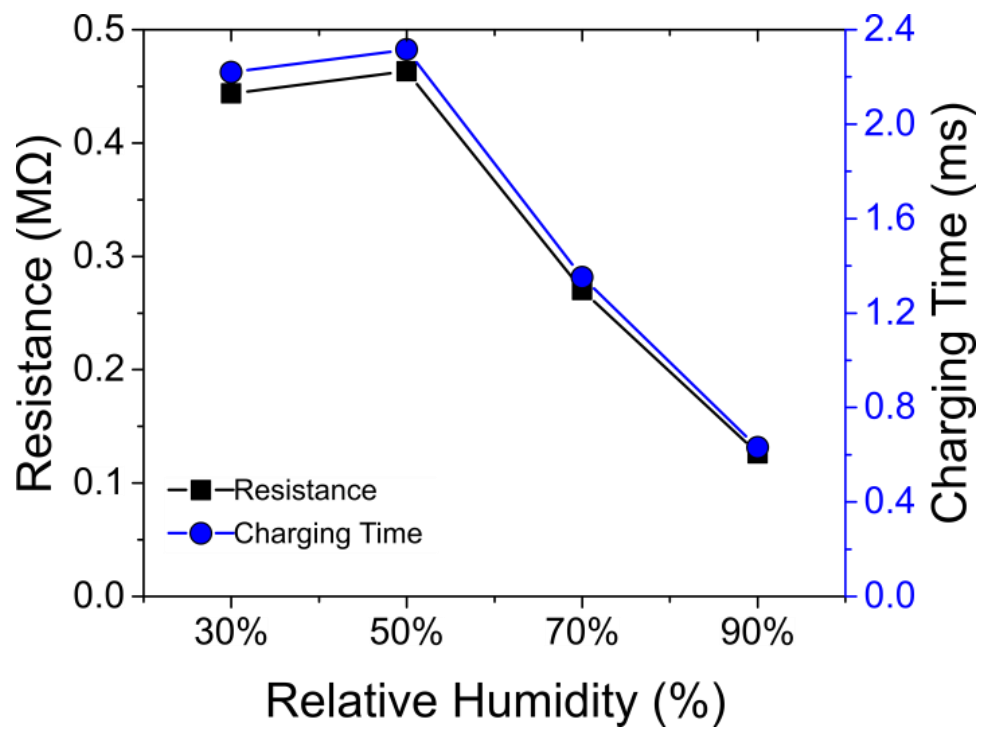


Figure A1. Calculated Ohmic resistance and charging time (given by 5τ).

Appendix B.

Numerical model¹

Due to axial symmetry of the microdisk electrode-ionomer film interface, a two-dimensional model in cylindrical coordinates was considered. The mathematical model is given by the following relations:

$$\partial_t c - \nabla \cdot (D_{bO_2} \nabla c) = 0, \quad x \in \Omega \subset \mathbb{R}^2, \quad t > 0, \quad (1)$$

$$c = 0, \quad x \in \Gamma_1 \subset \mathbb{R}^1, \quad t > 0, \quad (2)$$

$$-(D_{bO_2} \nabla c) \cdot \mathbf{n} = 0, \quad x \in \Gamma_2 \subset \mathbb{R}^1, \quad t > 0, \quad (3)$$

$$c = c_{bO_2}, \quad x \in \Gamma_3 \subset \mathbb{R}^1, \quad t > 0, \quad (4)$$

$$c = c_{bO_2}, \quad x \in \Omega \subset \mathbb{R}^2, \quad t = 0, \quad (5)$$



Figure B2. Computational domain and boundary conditions. The ionomer-electrode interface (Γ_1) is represented by the green line, ionomer-gas interface (Γ_3) is shown in blue, and the rest is the ionomer part of the domain.¹⁵⁹

where Ω is the two-dimensional computational domain with one-dimensional boundaries $\Gamma_i, i = \overline{1,3}$, shown in Figure B2, where a typical coarse mesh is presented with boundary lines thickened for illustration purposes.

Eqn. 1, with boundary and initial conditions represented by (2)-(5), was brought to a dimensionless form by introduction of three scaling factors: ionomer thickness, L , total time of simulation, T , and bulk oxygen concentration, c_{bO_2} . For the thicknesses (L) of the ionomer samples

¹ Numerical modeling was performed by Mr. Aslan Kosakian, with contributions from Dr. Marc Secanell (both from University of Alberta)

tested, the rate of oxygen dissolution is fast, and thus equilibrium at the ionomer-gas interface was assumed and represented by the boundary condition (4).^{87,160} Oxygen diffusion into the domain (gas-ionomer-electrode) was only allowed through the top interface (number 3 in Figure B2), as the bottom surface of the ionomer was in contact with the glass support of the electrode. Four different meshes were generated for the selected experimental cases to account for changing values of the effective electrode radius. Analytically fitted diffusivity values were used to estimate the expected diffusion length in each case and to choose an optimal size of the radial cut of the domain and its thickness. If the estimated diffusion length was close to or larger than the thickness of the ionomer, a rectangular domain was considered with thickness of 53 μm (the average thickness of all samples), and 2.5 times larger length.

Space discretization was performed with the finite element method using second order Lagrange shape functions. For time discretization, a Crank-Nicolson scheme was used. Detailed numerical procedure, including the fitting algorithm and description of the adaptive mesh refinement and adaptive time stepping methods used in the code can be found in a previous report by Kosakian et al., along with the validation of the numerical model, and will also be discussed in forthcoming publications.¹⁵⁹ In this work, an improved version of the code is used with automatic error estimation and optimal time step computation as described in the work by Farag^{*2} et al.¹⁶¹

The total current produced at the ionomer-electrode interface was computed based on the total flux of oxygen through the corresponding boundary Γ_1 :

$$I = -nF \int_{\Gamma_1} -D_{bo_2} \nabla c \cdot \mathbf{n} d\Gamma \quad (6)$$

Table B2 contains parameters used in the simulation for each of the mentioned cases. A value of 10^{-8} was used as tolerance for absolute solution error while 10^{-5} was the tolerance for relative solution error for the adaptive time stepping algorithm. In all simulations, relative error criterion was dominating in step size change. The number of performed adaptive refinements at each tenth time layer is reported in the n_{ref} column. The optimal value of n_{ref} in each case was found through running simulations for different test cases and comparing simulated current between refinement levels. At the

* In equation (9) of that paper, the ratio under the root should be inverted. It makes sense to decrease the time step when the solution error is larger than the tolerance and not otherwise.

first time step, and every tenth time step, a local grid refinement was performed using the Kelly error estimator. The 10% of cells with the largest error were refined and 1% of cells with the smallest error were coarsened. Two-dimensional distributions of oxygen concentration versus RH at $t \approx 5$ s are shown in Figure B3.

Parameter estimation

In order to estimate solubility and diffusivity, numerical current was fit to the experimental data. Similarly to the Shoup-Szabo fitting algorithm described in the main text, NRMSD was used as a numerical fit error and experimental data points containing non-Faradaic effects were removed by the introduction of time truncation and shifting with search bounds of 0.1 s and 0.25 s. Each range of solubility and diffusivity values consisted of 20 points in each direction, totalling 400 simulations for each RH. Simulated results were then interpolated onto a 77·77 point mesh and the point with the smallest NRMSD was found (Figure 4.17 in the main text). Numerically obtained oxygen transport properties, as well as truncation and shifting time values, are shown in Table 4.2 in the main text.

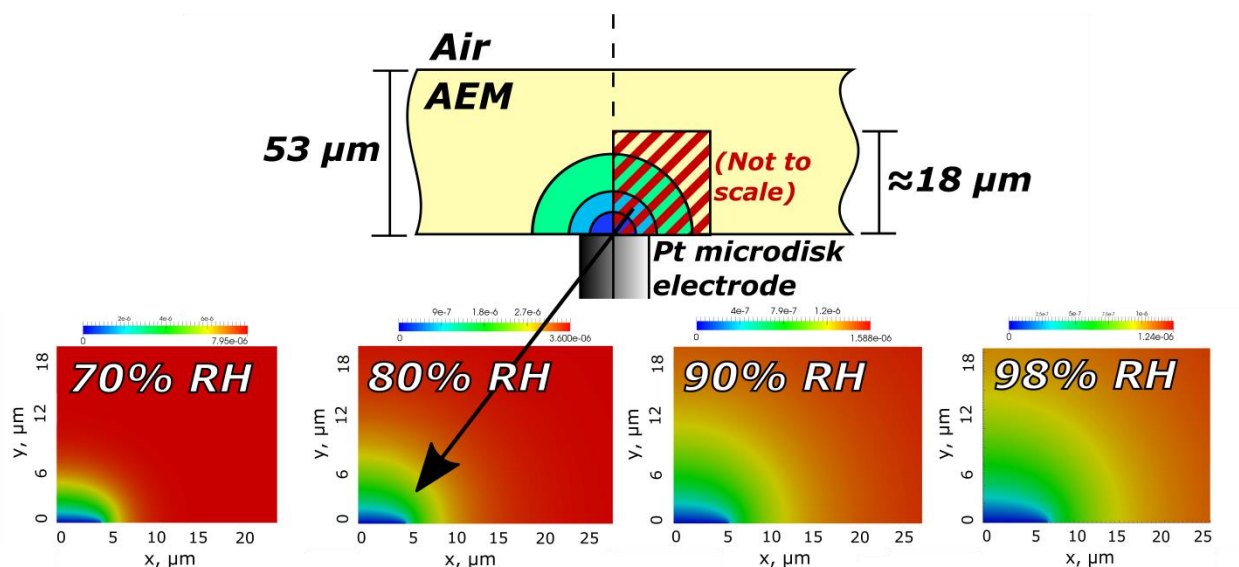


Figure B3. Top, diagram showing axis symmetrical quadrant in experimental setup being solved in numerical model (below). 2D distributions at $t \approx 5$ s of oxygen concentration (in mol/cm³) around the electrode from 70%, 90%, and 98% RH for 2.1 meq/g IEC HMT-PMBI-OH- at 60°C.

Table B.1 Estimated diffusion lengths for 2.1 meq/g IEC HMT-PMBI-OH at 60 °C at various relative humidities

| RH (%) | $D_{bO_2}^{an} \text{ (cm}^2\text{/s)} \cdot 10^7$ | $L_D \text{ (}\mu\text{m)}$ |
|--------|--|-----------------------------|
| 70 | 0.158 | 5.6 |
| 80 | 1.20 | 15.5 |
| 90 | 11.0 | 47.0 |
| 98 | 26.8 | 73.0 |

Table B.2 Parameters of simulations for 2.1 meq/g IEC HMT-PMBI-OH at 60 °C at various relative humidities

| RH, % | $r_{eff}, \mu\text{m}$ | Domain size, $\mu\text{m} \cdot \mu\text{m}$ | DoFs (coarse) | n_{ref} | $\alpha, \%$ | $c_{bO_2} \cdot D_{bO_2},$ $10^{-7} \text{ mol/cm}^3 \cdot$ $10^{-8} \text{ cm}^2/\text{s}$ |
|-------|------------------------|---|------------------|-----------|--------------|---|
| 70 | 4.68771 | $4r_0 \cdot 5r_0$ | 779 | 1 | 4.94 | [30.00,134.50] · [0.10,4.85] |
| 80 | 4.76616 | $53.0 \cdot 132.5$ | 1407 | 0 | 2.61 | [10.00,60.00] · [4.00,20.00] |
| 90 | 5.61470 | $53.0 \cdot 132.5$ | 1235 | 0 | 2.76 | [10.00,26.00] · [10.00,143.00] |
| 98 | 6.95156 | $53.0 \cdot 132.5$ | 1159 | 0 | 2.84 | [4.00,19.96] · [40.00,401.00] |